THERMAL PROPERTIES AND CHARACTERIZATION OF METHANE HYDRATES

by

Eilis Jill Rosenbaum

BS, BSE, Geneva College, 2001

Submitted to the Graduate Faculty of

School of Engineering in partial fulfillment

of the requirements for the degree of

Master of Science

University of Pittsburgh

2004

UNIVERSITY OF PITTSBURGH

SCHOOL OF ENGINEERING

This thesis was presented

by

Eilis Jill Rosenbaum

It was defended on

June 27, 2003

and approved by

Dr. Irving Wender, Research Professor, Chemical and Petroleum Engineering Department

Dr. Robert Enick, Professor and Macleod Faculty Fellow, Chemical and Petroleum Engineering Department

Dr. David Shaw, Geneva College, Associate Professor, Mechanical Engineering

Robert Warzinski, US Department of Energy NETL, Research Chemist

Thesis Advisor: Dr. Gerald Holder, US Steel Dean of Engineering Professor, Chemical and Petroleum Engineering

THERMAL PROPERTIES AND CHARACTERIZATION OF METHANE HYDRATES

Eilis Jill Rosenbaum, MS

University of Pittsburgh, 2004

Renewed interest in methane hydrates as a potential, unconventional energy source has prompted investigation into their thermal properties, which are necessary to determine heat flow through the hydrate for resource production.

In this investigation thermal property measurements have been made on unconsolidated pure methane hydrate samples formed in a high-pressure variable-volume viewcell (HVVC). Using a transient plane source (TPS) technique, a single measurement was used to simultaneously determine the thermal conductivity and thermal diffusivity of the methane hydrate inside the viewcell. A vessel was designed to contain the sample around the TPS for thermal property measurements while inside the HVVC. The vessel was successful in containing the sample during the hydrate formation experiments and its design made it possible to recover a methane hydrate sample, which was analyzed with Raman spectroscopy.

The striking quality of methane hydrate is that its thermal conductivity is much lower than ice, despite its structural similarities to ice. The thermal conductivity of pure methane hydrate for a temperature range of 264 K to 277 K and pressure range of 11.6 MPa to 13.0 MPa, respectively, can be described by $k = (-0.0034\ T + 1.2324)$ W/mK, where T is in Kelvin. The average of the thermal conductivity values within this range of temperatures and pressures is $k = 0.30 \pm 0.02$ W/mK. The sample was recovered and analyzed with Raman spectroscopy, confirming that the sample was pure hydrate.

The thermal diffusivity of methane hydrate has only been reported by one other investigator in preliminary experiments. The thermal diffusivity of methane hydrates determined in the work reported herein for a temperature range of 264 K to 277 K and pressure range of 11.6 MPa to 13.0 MPa, respectively, is $\alpha = (2.59 \pm 0.16) \times 10^{-7}$ m^2/s. The thermal diffusivity can also be described by $\alpha \times 10^7 = (0.0005\ T + 2.4424)$ m^2/s where T is in Kelvin.

TABLE OF CONTENTS

LIST OF TABLES

LIST OF FIGURES

ACKNOWLEDGEMENTS

The research reported here was supported by the University / NETL Student Partnership Program, Grant # DE-FC26-OINT41196.

Robert Warzinski of NETL supervised my work, teaching me how to do research and teaching me how to perform in a research environment. Bob was patient and supportive in letting me develop my work and was open to my ideas, allowing me to be independent in my research. I want to thank him for taking me as a student and supporting me in my learning.

Dr. Gerald Holder, Dean of Engineering at the University of Pittsburgh, was my research advisor and though his role was remote, his support, knowledge, and advice was integral to my work.

I would like to thank Ronald Lynn of NETL. Ron played an integral role in upgrading and automating our experimental setup. He wrote the data acquisition program, automating data collection. He supplied his vast knowledge of National Instrument's software and hardware and was a great resource for learning LabVIEW.

Dr. David Shaw of Geneva College developed most of the data analysis described here. He hired me as a research assistant while I was an undergraduate which led to an internship at NETL. As such, I was able to continue this work as a graduate student at Pitt. I thank him for his vast knowledge and work on the technique contained in this thesis and to also thank him for what he taught me as an undergraduate student, giving me a great foundation that supported the additional learning I accomplished as a graduate student. His continued support on this project is also much appreciated.

I thank my other committee members for their time and approval of my work: Dr. Robert Enick, University of Pittsburgh, and Dr. Irving Wender, University of Pittsburgh.

I would be remiss to not acknowledge the great support and encouragement of my parents, sisters, and wonderful friends all over the country and here in Pittsburgh.

1.0 INTRODUCTION

With recent estimates of *in situ* gas hydrates in the ocean and permafrost regions there is renewed interest in hydrates because of their potential as an unconventional energy source. Interest in and studies of natural gas hydrates as a potential energy source date back to the mid-1960's with the U.S.S.R.'s research of hydrate kinetics and thermodynamics [1]. Natural gas hydrates present an appealing resource of methane because energy obtained from the gas in the hydrate is fifteen times greater than the energy required to dissociate the hydrate for recovering the gas [1].

Gas production can be accomplished by creating a shift in the thermodynamic equilibrium of the hydrate [2]. Proposed gas recovery methods involve hydrate dissociation by three methods: thermal stimulation, depressurization, and inhibition [1, 2]. The rate of hydrate decomposition seems to be determined by the movement of a decomposition front which depends on the magnitude of heat flow through it [2]. If a temperature difference exists across the hydrate reserve, heat will flow from the hotter region to the cooler region via conduction. To model gas decomposition, knowledge of the heat flow through the sample must be determined which, therefore, requires knowing the thermal properties of the medium [2]. The thermal conductivity and thermal diffusivity are basic properties important in understanding the thermal behavior of the hydrate reservoir [3], however, the number of thermal property measurements reported is several orders of magnitude lower than that for phase equilibrium properties [1].

Further advances in hydrate research depends fundamentally on high-quality property data and laboratory exploration of the physics and chemistry that govern naturally occurring hydrates [4]. Measurements should also be made on samples inside the synthesis vessel. Because the thermal conductivity of an aggregate of sediment, water, and gas hydrate is a function of the individual phases, the concentration and distribution of those phases and, the nature of the interfaces between the phases, sample characterization is also essential.

In this work, a well developed and widely used method for thermal property measurements was employed. The transient plane source (TPS) technique, developed [5] and patented [6] by Gustafsson, allows the determination of both the thermal conductivity and thermal diffusivity from one measurement. This technique offers a non-invasive, quick, and reliable method of thermal property determination. Unlike past thermal property measurement methods, this technique can be used with small sample sizes and was adaptable, with minor modifications, to an existing experimental setup where methane hydrates have been successfully formed.

All components used in the setup of this system are commercially available. The experimental system has been updated using National Instruments components and a National Instruments programming system, LabVIEW, to automate thermal property measurements and data analysis for determining the thermal properties. Use of LabVIEW allows data acquisition and data analysis to be done coincidently during hydrate formation and dissociation experiments.

2.0 LITERATURE REVIEW

2.1 METHANE HYDRATE PROPERTIES

All natural gas hydrates form in one of three crystal structures (cubic structure I, cubic structure II, and hexagonal structure H) and, unlike ice which forms as a pure component, hydrates require guest molecules of the proper size to form. Methane hydrates form in cubic structure I which has large and small cavities. The large cage is a tetrakaidecahedron (14-sided) cavity, containing 12 pentagonal faces and 2 hexagonal faces ($5^{12}6^2$) (see Figure 2-1). The small cage is a pentagonal dodecahedron (12-sided) cavity which has twelve pentagonal faces (5^{12}) (see Figure 2-1). Hydrate crystal cell structure I is cubic with a body centered lattice. The small and large cages of Structure I are shown in Figure 2-2 where two complete $5^{12}6^2$ connect four 5^{12}. [1]

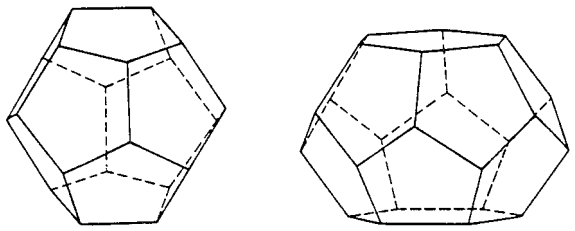

Figure 2-1: Cavities in Gas Clathrate Hydrates (a.) Pentagonal Dodecahedron (5^{12}). (b.) Tetrakaidecahedron ($5^{12}6^2$).

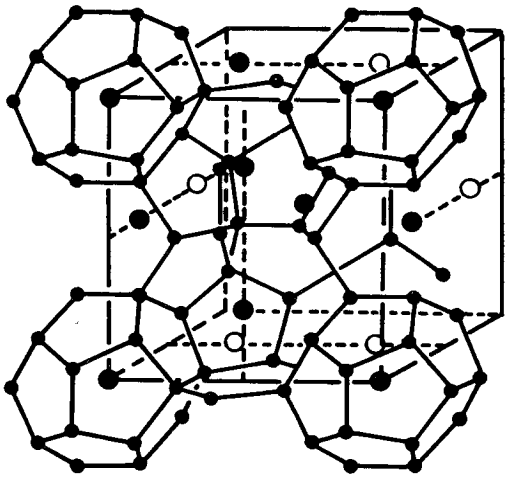

Figure 2-2: Hydrate Crystal Unit Structure I (McMullan and Jeffrey, 1965; taken from Sloan [1])

Hydrates consist of about 85% water on a molecular basis, so many of their mechanical properties resemble those of ice Ih, however, their thermal expansion and thermal conductivity are significantly different than that of ice [1]. The thermal conductivity of hydrates is markedly lower than ice and close to that of water. The low thermal conductivity of hydrates is due to their lattice structure, where the water molecules are restricted from translation or rotation. Because they vibrate anharmonically about a fixed position, a mechanism for scattering of phonons is provided, which causes the thermal conductivity to be lower. A weak coupling between the guest and host lattice does not noticeably affect most structural thermodynamic and mechanical properties but does hinder the transport of heat.

In solids, heat transport and dissipation is accomplished via acoustic lattice vibrations. The methane molecule inside the hydrate cage rotates freely as was determined by neutron scattering experiments [7]. Though the methane is free to rotate, its coupled motion with the lattice vibrations dissipates heat transport of the crystal-like structure. This dissipation of heat caused by the host molecule thus causes the thermal conductivity to be lower.

In a constant volume pressure vessel containing liquid water and methane gas at sufficient pressure, the pressure is seen to decrease as the temperature is decreased until hydrate nucleation begins [1]. As hydrates nucleate, a rapid reduction in pressure is observed (see Figure 2-3). The

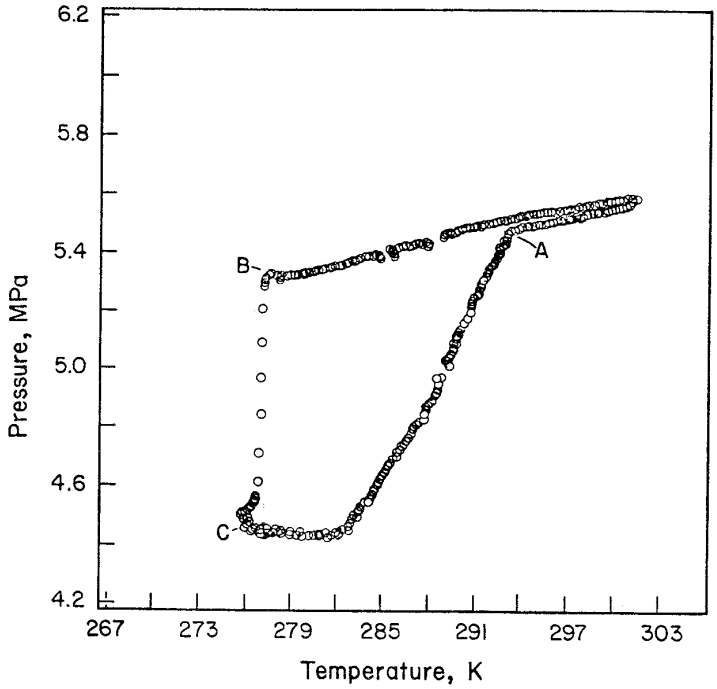

Figure 2-3: Temperature and pressure trace for formation of simple methane hydrates (from Sloan [1]).

pressure versus temperature of the dissociation line will retrace the pressure versus temperature of the formation line.

Hydrate from a two phase gas-water system has been hypothesized to occur in four stages [1]. The initial condition is where the pressure and temperature are favorable for hydrate formation but no gas molecules are yet dissolved in water. As gas dissolves, labile clusters form immediately. These labile clusters then agglomerate by sharing faces. When the size of the cluster agglomerates reaches a critical value, growth begins. When the critical cluster radius is reached, nucleation occurs. The induction time of methane hydrates is much longer than that of other gas hydrates, which has been measured to be longer than 24 hours. This sequence of steps continues to be a matter of some debate [8].

Hydrates form from gas and either water or ice at elevated pressures and low temperatures [1]. Nucleation from water is time-dependent with a high degree of metastability and a function of displacement from equilibrium, the state and history of the water, the composition of the gas, the degree of agitation or turbulence, and the geometry of the system and surface area. Nucleation from solid ice occurs easier when the temperature is increased above the melting

point. Melting ice provides a template for the formation of hydrates but once a protective film of hydrates forms at the surface, hydrate formation has been seen to diminish or cease.

Link et al [9] at the U.S. Department of Energy successfully formed methane hydrates from double-distilled water and methane in a high-pressure view cell with a high degree of vortex mixing. Hydrate was formed by pressurizing the cell with methane between 5.5 MPa and 13.8 MPa and dropping the temperature until hydrate formation was observed. In experiments to determine maximum methane uptake, methane was continually delivered to the cell to maintain a constant head pressure.

In experiments to study hydrate formation and dissociation, visual observation was made of hydrate crystals forming, agglomeration of the crystals, and the formation of a solid hydrate mass [9]. After formation of the solid hydrate mass, additional hydrate formation was observed with a decrease in the pressure with time as more free methane was incorporated into the crystal structure. Experiments were also performed using a surfactant. Additional hydrate could be formed because the formed hydrate was forced to the edges of the interfaces between water and gas, allowing the water-methane contact to be present longer, and the concentration of methane in the water to remain constant throughout formation. Using water containing 224 ppm of surfactant, the hydrate phase contained over 96% of the maximum theoretical amount of methane that would have been incorporated into hydrates if 100% of the water was converted to hydrate.

Waite et al from U.S. Geological Survey (USGS) [10] formed methane hydrate from granular ice in their thermal conductivity measurement device (thermal conductivity experiment described later). They started with granular ice (180 – 250 μm), or granular ice mixed with sediment in a methane pressurized vessel, and slowly heated the sample to form methane hydrates. They note that by creating hydrate from granular ice and sediment, a uniform mixture is obtained.

Once hydrate is formed and dissociated it has been seen that hydrates do not completely decompose but leave a partial structure which promotes hydrate formation more readily on subsequent cooling cycles. The residual structure of water is destroyed at temperatures greater than 28 ^{o}C [1]. In the work done by Link et al, this phenomenon was observed. With successive formations, the formation time decreased, which they attributed to possible microscopic hydrate crystals that were still present in the solution at 15 ^{o}C. If present, the crystals would act like seeds for future hydrate formation. [9]

2.2 THERMAL PROPERTY MEASUREMENTS OF METHANE HYDRATES

The number of thermal property measurements for natural gas hydrates are several orders of magnitude lower than those for phase equilibrium properties. A challenge in thermal property measurements lies in determination of the sample composition prior to measurement, which can be affected by hydrate decomposition when the apparatus is loaded with preformed hydrate [1]. Also a challenge is completely converting all of the water to hydrate and the ability to confirm this.

Sloan summarizes methods used thus far to determine thermal conductivity values of hydrates [1]. Stoll and Bryan [11] used a transient needle probe on propane hydrates, compacted after formation. A modified version of the needle probe was computerized, refined, and extended to short times and used by Asher [12] to measure the thermal conductivity of methane hydrates in sediments with an estimated accuracy of ± 8%. A steady-state method was used by Cook and Leaist [13] to measure the thermal conductivity of methane hydrates to within ± 12%. The thermal conductivity determined by Cook and Leaist was 0.45 W/mK at a temperature of 216.2 K. In this experiment, however, the sample was prepared and pressed externally and then introduced to the hot-plate cell of the apparatus. Sloan also notes that much remains to be explored in this area of hydrate research. Measurements reported by Sloan also indicate that neither the types of guest molecule nor the types of hydrate crystal significantly affect the thermal conductivity.

Ross and Anderson report thermal conductivity values for tetrahydrofuran using the transient hot-wire method [14]. Their results indicate that the thermal conductivity was proportional to temperature and not a function of pressure. In the range of temperatures from about 100 K to 250 K the thermal conductivity of tetrahydrofuran hydrate was about 0.47 W/mK to about 0.53 W/mK, respectively, showing a positive trend in the thermal conductivity with temperature, which they attribute to molecular disorder within the hydrate structure.

Cook and Leaist [13] measured the thermal conductivity of pressed samples of methane hydrate. To form the samples, powdered ice was loaded into a pressure vessel and ultrahigh

purity methane was condensed into the pressure vessel. Agitation of the sample was accomplished by rotating the vessel for several days, subjecting the sample to abrasion by rods contained within the vessel. The temperature was maintained at -13 ^{o}C to form the hydrate. The sample composition was $CH_4 \bullet (5.7 \pm 0.8)\ H_2O$. After hydrate formation, the sample was removed and pressed into a disc for thermal conductivity measurements using the guarded hot-plate cell method. During the sample preparation some atmospheric water condensed in their sample. During thermal property measurements, the hydrate decomposed considerably. At the completion of the measurement, the methane hydrate content, determined by weight loss, was found to be 57 ± 5%.

Asher [12] used a needle probe to measure the thermal conductivity of methane hydrates in sediments. The hydrate formation cell was packed with sediment, saturated with water, and the needle probe was inserted. The cell was pressurized with methane up to 11.7 MPa (1700 psia). The temperature was lowered to 1 ^{o}C to form hydrates. They assumed complete formation when the pressure change approached zero. In order to verify that the sample was in fact hydrate and sediment and not ice in sediment, they measured the thermal conductivity above and below the ice point and concluded that it should be the same if the sediment was saturated with hydrate only. Their experimental system was calibrated with water and glycerin. The value he reports for methane hydrate in Ottawa sand is $k = 2.75$ W/mK at $T = 275$ K. Other thermal conductivity values were displayed on a graph included in his thesis with no actual values reported. The graph compiled by Asher is in Figure 2-4 with other recent measurements included. The values reported by Asher show that hydrate in the sediments decrease the bulk thermal conductivity of the sample from that of water. The thermal conductivity of methane hydrates in sediment is about half of the thermal conductivity of ice in sediments.

Recent work done by Brian deMartin reports thermal conductivity values and thermal diffusivity values for methane hydrates and methane hydrates in Oklahoma 1 sand (~100%

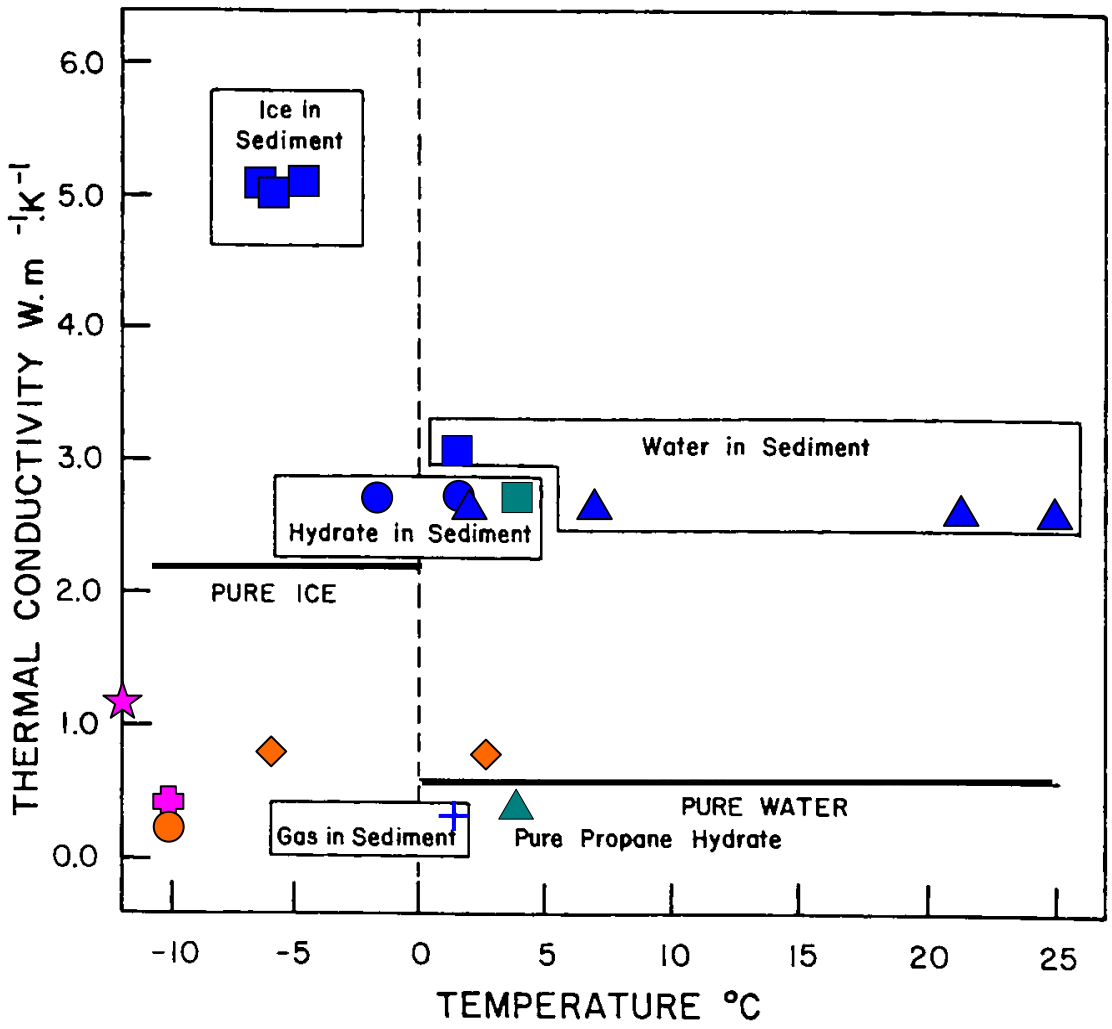

Stoll and Bryan (1979)
- 20-30 Mesh Ottawa Sand and Propane Hydrate
- Pure Propane Hydrate

deMartin (2001)
- Oklahoma Sand with Methane Hydrate
- Pure Methane Hydrate

Asher (1987), 20-30 Mesh Ottawa Sand
1. 80% Water Saturation
2. 80% Water Saturation
3. 0% Water Saturation
4. 100% Water Saturation

(Numbers indicate sample fabrication order)

USGS (2002)
- 68 vol.% Quartz Sand, 38 vol.% Methane Hydrate
- Pure Methane Hydrate

Figure 2-4: Thermal conductivity history compiled by Asher [12] with recent measurements added.

quartz sand, density = 2,650 kg/m^3, and grain size = 100 ± 50 μm) [15]. The thermal conductivity measurements were performed in the apparatus used for hydrate synthesis via the needle probe thermal conductivity method. Granular, sieved (180- to 250 μm) H_2O ice seed grains placed in a high pressure cylinder were pressurized with cooled methane to a pressure of 22 MPa. The sample was then heated to near the melting point of ice (271.5 K) to form methane hydrate. This method of hydrate formation is supposed to produce samples closest in properties to natural gas hydrates, even close in terms of stoichiometry. deMartin reports the thermal conductivity of a porous Structure I methane hydrate sample at 263 K and a confining pressure of about 28 MPa to be 0.32 ± 0.005 W/mK. The pure methane hydrate samples measured by deMartin were estimated to have a porosity of 28% to 33%, determined by knowing the hydrate volume and the volume of the sample vessel.

deMartin concludes from preliminary experiments that in sand, gas decreases the bulk thermal conductivity and hydrates act to increase the thermal conductivity from about 0.25 W/mK for a sand and gas mixture to about 0.82 W/mK for unconsolidated methane hydrate and sand mixtures [15]. He also found that the thermal conductivity of hydrate / sediment mixtures increased with the presence of methane hydrate. His explanation of this phenomenon is that the hydrate enhances grain to grain contact, thereby increasing heat flow through the sample.

The only other known measurements of thermal diffusivity were reported by deMartin using the modified Angstrom method [15]. The samples used to measure the thermal diffusivity were formed and compacted at USGS-Menlo Park, wrapped in aluminum foil, stored in liquid nitrogen and transported to Lawrence Livermore National Labs (LLNL) for the thermal diffusivity measurements. To make the measurements, the samples were drilled with two holes for inserting thermocouples. A wire at the center was used to apply a sinusoidal voltage to the samples and the temperature wave was monitored during the heating to determine the thermal diffusion of the sample. The thermal diffusivity was determined by knowing the phase difference between the two thermocouples, the period of the sinusoidal heat wave, and the radial distance between the two thermocouples.

The results reported by deMartin show that the thermal diffusivity rises with increasing pressure and falls with increasing temperature [15]. He also found that the presence of water ice affects the thermal diffusivity of the hydrate, and that the thermal diffusivity increases with increasing confining pressure. The character of the pressure dependence varied from sample to

sample. Because of problems in the experiment, thermal diffusivity values at a constant confining pressure of about 10 – 16 MPa, could only be made at temperatures between 148 K and 170 K. He reported thermal diffusivity values for temperatures of 150 K and 270 K at confining pressures of 0.1 MPa to 15 MPa as $\alpha = 4.5 \times 10^{-7}$ m^2/s and $\alpha = 4.2 \times 10^{-7}$ m^2/s, respectively. In his work the thermal diffusivity decreased with increasing temperature.

The most recently recorded methane hydrate thermal conductivity measurements were done by Waite et al at USGS [10]. They used a needle probe method as well, where the sample was formed and compacted around the needle probe in the thermal conductivity measurement chamber. They report values for ice Ih ($k = 2.12 \pm 0.015$ W/mK at $T = -10$ ^{o}C), pure methane hydrate ($k = 0.460 \pm 0.003$ W/mK at $T = -10$ ^{o}C and $k = 0.454 \pm 8.14 \times 10^{-4}$ T for a temperature range of -30 ^{o}C to -5 ^{o}C), and a uniform mixture of 32 vol. % methane hydrate with 68 vol. % quartz sand ($k = 1.15 \pm 0.015$ W/mK at -15 ^{o}C). Before taking thermal conductivity measurements, the sample was compacted to reduce porosity in the sample until the thermal conductivity values ceased to change with increasing pressure. The hydrate samples were checked to ensure that all water in the sample was converted to hydrate by lowering the temperature to -10 ^{o}C and checking for ice formation from any un-reacted water.

As evidenced above few thermal property measurements have been made on methane hydrates and the most recently reported thermal property values are in the developmental stages with little to no sample characterization reported. The values reported by Cook and Leaist were of samples made external to the actual thermal conductivity measuring device. Asher does not report values of pure methane hydrate and the samples he used are not well characterized in his thesis. deMartin has made significant progress with thermal property measurements and reports the only other known values of the thermal diffusivity of methane hydrates. USGS comes closest to reporting well characterized samples as well as measurements of consolidated methane hydrate samples. Much remains to be explored in the determination of the thermal properties of methane hydrates. Inherent is the challenge of sample characterization to ensure that the measurement can be correlated to the physical properties and composition of the sample.

2.3 TRANSIENT PLANE SOURCE (TPS) TECHNIQUE

A technique has been developed and patented [6] by S. E. Gustafsson to determine the thermal diffusivity and thermal conductivity of a material by simultaneously heating the material with and recording the voltage change over a transient plane source (TPS) element [5]. The transient plane source (TPS) technique, transformed from the transient hot strip method, has been used for determining the thermal conductivity of a variety of materials in the range from 0.02 W/mK to 200 W/mK [16].

The TPS technique, unlike its predecessor, can be used for small sample sizes because its conducting pattern arrangement allows the total electric resistance of the TPS to be much higher than the hot strip [17]. Because the total time of the transient recording is based on the size of the TPS, the measurement time is also reduced.

The TPS element used and described by Gustafsson consisted of a pattern of a thin, electrically conducting material in a symmetric shape [5]. The conducting material is usually one with a well known or easily determined temperature coefficient of resistivity (TCR) that is relatively constant over a wide range of temperatures. The TCR of the conducting material is used to determine the temperature rise in the conducting material due to the electrical current pulse applied to the TPS during the transient heating.

Starting with Carslaw and Jaeger's [18] point source solution to the thermal conductivity equation a solution can be found to describe the temperature increase in the sample. The temperature increase in an infinite solid due to a quantity of heat, $Q\rho c$, instantaneously liberated at time, t' and at a point (x', y', z'), for an anisotropic material with principal thermal conductivities, k_1, k_2, k_3, along the directions of the x-, y-, z-axis, is given by:

$$\Delta T(x,y,z,t) = \frac{Q(\rho C_p)^{3/2}}{8\left(\pi^3 k_1 k_2 k_3\right)^{1/2}(t-t')^{3/2}} \exp\left\{-\frac{\rho C_p}{4(t-t')}\left[\frac{(x-x')^2}{k_1}+\frac{(y-y')^2}{k_2}+\frac{(z-z')^2}{k_3}\right]\right\}, \quad \textbf{(2-1)}$$

where ρC_p is the specific heat capacity per unit volume. Accounting for the above assumptions, equation (2-1) satisfies the differential equation of conduction of heat.

Assuming that the conducting pattern is located in the *yz* plane of a coordinate system and inside an infinite solid, the temperature increase, at point *y*, *z* and time, *t*, due to an output power, *Q*, per unit area is [5 citing 18]:

$$\Delta T(y,z,t)=\frac{1}{8\pi^{3/2}\rho C_p}\int_0^t\frac{1}{[\alpha(t-t')]^{3/2}}dt'\int_A Q(y',z',t')\exp\left\{\frac{-\left[(y-y')^2+(z-z')^2\right]}{4\alpha(t-t')}\right\}dy'\,dz', \quad \textbf{(2-2)}$$

where α is the thermal diffusivity defined by:

$$\alpha=\frac{k}{\rho C_p}, \quad \textbf{(2-3)}$$

and *A* is the total area of the conducting pattern.

To simplify the equation and for further convenience, the equation for the temperature increase is expressed as a function of τ, defined as [5]:

$$\tau=\left[\frac{t}{\theta}\right]^{\frac{1}{2}}, \qquad \theta=\frac{a^2}{\alpha}. \quad \textbf{(2-4)}$$

2*a* is the width of the conducting pattern. θ is the characteristic time of the measurement. $\Delta T(y,z,\tau)$ in terms of τ, which results from a change of variable in equation (2-2), is:

$$\Delta T(y,z,\tau)=\frac{1}{4\pi^{3/2}ak}\int_0^\tau\frac{1}{\sigma^2}d\sigma\int_A Q\left(y',z',t-\frac{\sigma^2a^2}{\alpha}\right)\exp\left\{\frac{-(y-y')^2+(z-z')^2}{4\sigma^2a^2}\right\}dy'\,dz'. \quad \textbf{(2-5)}$$

To get the temperature rise in terms of τ, $\alpha(t - t')$ was replaced by σ^2a^2 to perform the integration [19].

The pattern of the TPS can be considered a series of "individual" strips. Defining the strip width as, $2D_p$, where p represents a point on curve P, made up of points located at equal distances from the edges of the individual strips, the resistance increase due to a short element of an individual strip can be given as [5]:

$$dR = \rho_0 \left(1 + (TCR)\overline{\Delta T_p(\tau)}\right)\frac{1}{2D_p\, 2\nu}\, dr\,, \qquad \textbf{(2-6)}$$

where dr is defined as the displacement in the direction of the tangent to curve P, ρ_0 is the resistivity of the pattern material, and 2ν is the constant thickness of the conducting pattern. The average temperature rise at each point, p, can then be expressed as [5]:

$$\overline{\Delta T_p(\tau)} = \frac{1}{2D_p}\int_{-D_p}^{+D_p} \Delta T(y,z,\tau)\, dn\,, \qquad \textbf{(2-7)}$$

Integration is performed for each point, p, in a direction dn perpendicular to the tangent of the curve P along the entire strip. $\Delta T(y,z,\tau)$ is given by equation (2-5).

The average temperature is related to the resistance through the following equation [5]:

$$R(t) = R_0\left[1 + (TCR)\overline{\Delta T(\tau)}\right], \qquad \textbf{(2-8)}$$

where R_0 is the initial resistance of the TPS before the power is supplied. The resistance across the TPS throughout the transient heating, $R(t)$, is calculated from voltage data collected during the transient heating. The temperature coefficient of resistivity (TCR) is known for the material of the conducting pattern, which allows the temperature rise to be calculated. The TCR is calculated by [20]:

$$TCR = \frac{1}{R(T)}\frac{\partial R(T)}{\partial T}\,. \qquad \textbf{(2-9)}$$

The conducting pattern can be in any shape but generally in basic shapes for the ease of deriving equations to describe its temperature rise. Gustafsson presents equations for a "hot disk" configuration and a "hot square" configuration [5]. The conducting pattern can be produced by vapor deposition [5] and for the hot disk and hot square it is deposited in a "bifilar spiral" pattern resembling a disk or a serpentine pattern in the shape of a square, respectively.

Starting from equation (2-7) the average temperature increase can be given for the hot square pattern. Assuming that neither the square source nor the leads carrying the current would influence the temperature increase either as heat sources or heat sinks, and as a result, the output of power per unit area, Q [W/m^2], is considered constant after time, t_0, the temperature increase in any point (y, z) in the plane $x = 0$ can be given as [5]:

$$\overline{\Delta T(\tau)} = \frac{P_0}{4\pi^{1/2} ak} H(\tau), \qquad \textbf{(2-10)}$$

$$H(\tau) = \int_0^{\tau} \left\{ erf \frac{1}{\upsilon} - \frac{\upsilon}{\pi^{1/2}} \left[1 - \exp\left(\frac{-1}{\upsilon^2} \right) \right] \right\}^2 d\upsilon, \qquad \textbf{(2-11)}$$

$$erfx = \frac{2}{\pi^{1/2}} \int_0^x \exp(-\upsilon^2) d\upsilon. \qquad \textbf{(2-12)}$$

P_0 is the constant output of power in the TPS element and assumed to be transferred to and consumed for heating the sample. The function $H(\tau)$ gives the temperature increase as a function of time [21] and can be approximated analytically or evaluated numerically. For τ values of about less than 0.3, equation (2-11) can be solved analytically [5].

Most commercially available TPS elements have thin insulating layers surrounding the conducting pattern for a sturdy sensing element that also allows measurements on electrically conducting materials. The equations given above for the temperature increase do not take into account these thin insulating layers above and below the conducting pattern and between the "strips" of the pattern. To include the effects of these layers, a good approximation can be established. By employing a numerical solution, integrals describing the theoretical expression can be solved [5].

Assuming that the strips are equally spaced and of equal width, the following can be defined: $2n$ = number of strips, $2d$ = width of each strip, $2a$ = length of each strip, and 2δ = the distance between two strips. So that [5]:

$$a = 2n(d+\delta) - \delta \tag{2-13}$$

In the same manner as before, an expression for the temperature increase at point (y, z) in the plane $x = 0$ at time t due to one single strip, with number i, is:

$$\Delta T_i(y,z,t) = \frac{Q}{8\pi^{3/2}\rho C_p}\int_0^t \frac{dt'}{[\alpha(t-t')]^{3/2}}\int_{(2i-1)(d+\delta)-d}^{(2i-1)(d+\delta)+d}\exp\left(\frac{-(y-y')^2}{4\alpha(t-t')}\right)dy' \times \int_{-a}^{a}\exp\left(\frac{-(z-z')^2}{4\alpha(t-t')}\right)dz' \tag{2-14}$$

For the temperature increase, caused by all 2n strips at the same point (y, z) the expression is given as [5]:

$$\Delta T_{2n}(y,z,t) = \sum_{1-n}^{n}\Delta T_i(y,z,t), \tag{2-15}$$

where $\Delta T_i(y, z, t)$ is given above.

The average temperature of one whole strip (with number i) is given as [5]:

$$\overline{\Delta T_i(t)} = \frac{1}{4ad}\int_{(2i-1)(d+\delta)-d}^{(2i-1)(d+\delta)+d} dy \int_{-a}^{a}\Delta T_{2n}(y,z,t)dz\,. \tag{2-16}$$

The average temperature, in terms of τ, taken over all the strips, becomes [5]:

$$\overline{\Delta T(\tau)} = \frac{1}{2n}\sum_{1-n}^{n}\overline{\Delta T_i(\tau)}, \qquad \textbf{(2-17)}$$

which can be rewritten in a useful form as [5]:

$$\overline{\Delta T(\tau)} = \frac{P_0}{4\pi^{1/2}ak} H_s(\tau). \qquad \textbf{(2-18)}$$

$H_s(\tau)$ is a function of time only, but incorporates parameters of the source size and shape (n, d, and δ). After numerically evaluating the above equations, $H_s(\tau)$ can be determined for different values of τ.

In the same manner, equations can be derived to describe the temperature rise in the hot disk. Although an exact solution is possible, Gustafsson gives two approximate solutions that he used in his work [5]. By assuming that the disk is made up of m number of concentric ring sources, the average temperature rise can be found from Carslaw and Jaeger's ring source solution [18]. The average temperature rise can be approximated as:

$$\overline{\Delta T(\tau)} = \frac{P_0 D_s(\tau)}{\pi^{3/2}ak}, \qquad \textbf{(2-19)}$$

where

$$D_s(\tau) = \frac{1}{[m(m+1)]^2}\int_0^{\tau}\frac{1}{\sigma^2}\left[\sum_{l=1}^{m} l\sum_{i=1}^{m} i\exp\left(\frac{-(l^2+i^2)}{4m^2\sigma^2}\right) I_0\left(\frac{li}{2m^2\sigma^2}\right)\right] d\sigma\,. \qquad \textbf{(2-20)}$$

P_0 is the total output of power, a is the radius of the disk, and I_0 is the modified Bessel function.

The second approximation assumes that the space between the concentric rings is infinitely small. The average temperature rise in this approximation is given as:

$$\overline{\Delta T(\tau)} = \frac{P_0 D(\tau)}{\pi^{3/2}ak}, \qquad \textbf{(2-21)}$$

where

$$D(\tau)=\int_0^{\tau}\frac{1}{\sigma^2}d\sigma\int_0^1\upsilon\int_0^1 u\exp\left(\frac{-\left(u^2+\upsilon^2\right)}{4\sigma^2}\right)I_0\left(\frac{u\upsilon}{2\sigma^2}\right)dud\upsilon. \qquad \textbf{(2-22)}$$

Through a detailed study, Gustafsson determined that the agreement between the two approximations was nearly perfect when a time correction was applied for τ values larger than 0.1 and for more than 10 concentric rings (*m* greater than 10) [5]. A correlation between the approximations and the ideal solution can also be made using a time correction. This close correlation between the approximate solutions and exact solution exists because the disturbances due to the space between the strips or rings in the conducting pattern are relaxing and disappearing very quickly at the beginning of the transient event. With a time correction, either of the approximations can be used to evaluate the thermal properties and the results will be close to those found using an exact solution [5].

As with the solution for the disk source, equation (2-11) can be used in conjunction with a time correction instead of solving for $H_s(\tau)$. While equation (2-11) is for an infinite number of strips, it gives a good approximation to the actual solution for the square source.

For TPS elements covered with insulating layers, the thermal contact between the heating material and the sample is reduced. The result is seen at the beginning of the transient recording where the power $Q(t)$ delivered to the sample is not constant. When a constant current is passed through the TPS element, the voltage drop across a Wheatstone bridge can be measured to determine the resistance variation across the element and therefore the temperature rise of the TPS element. The exact point where the power passing through the insulating layers is constant and is emitted to the sample is unknown and determination of which is influenced by a few factors. Non-ideal electrical components in the circuit will influence the start of the transient heating. The thermal resistance between the TPS element and the sample cause time delays between the power release in the element and delivery of the power to the sample. [22]

Gustafsson et al derives a model to determine the actual start of the transient event and finds a time correction, t_c. In his work he used a strip rather than a square or disk shaped source, but assumes that the strip is ideal with a variable output of power, all of which is delivered to the sample [22]. This means that any temperature difference between the two surfaces of the

insulating layer has become constant, though the mean temperature of the insulating layer itself will continue to increase throughout the transient heating. The thickness of the insulating layer should be much less than the width of the strip. Any disturbances at the beginning are assumed to dissipate quickly so that the power will become a constant value, P_0, after some time, t_0, after which the heat capacity of the insulating layer can be neglected. The time correction, t_c, and time zero, t_0, should be much less than the characteristic time, θ, so that enough data exists for evaluation. Gustafsson et al uses a second order polynomial in $(t - t_c)^{1/2}$ to which the data is fit. In an iterative procedure, t_c is determined by changing its value to maximize the fit of the data to the following polynomial [22]:

$$R = R_0 + A(t - t_c)^{1/2} + B(t - t_c). \quad \textbf{(2-23)}$$

A and B are empirical constants, particular to and determined for each thermal property measurement. In Gustafsson's work, t_0, was estimated as larger than $2t_c$.

All of the equations above assume that the material of interest surrounding the source is infinite. To make this assumption, it is sufficient if the material appears infinite to the source, so that the sample boundaries do not influence the thermal behavior of the sample. The probing depth, Δ_p, is the region of the sample heated during the transient recording. The distance from the source to any point on the outer surface of the sample must be greater than [5, 17, 22]:

$$\Delta_p = \beta(\alpha t_{\max})^{1/2}, \quad \textbf{(2-24)}$$

$t_{\max}$ is the total time of the transient recording and must be at least 1.5 θ, β is a constant of the order of unity, which is chosen for the desired experimental accuracy [5]. Gustafsson defines this value as $\beta = 1.42$ [23]. For very precise work, β can be chosen greater [17].

3.0 EXPERIMENTAL

3.1 THERMAL PROPERTY MEASUREMENTS WITH THE TPS TECHNIQUE

National Instrument's hardware and LabVIEW software are used to control the thermal property measurements (see Appendix for component diagrams). An electromechanical relay switch (SCXI 1161) is used to apply the voltage from a dummy load to the Wheatstone bridge containing the TPS sensor (shown in Figure 3-1). A SCXI 1320 temperature sensor terminal block connects the signals from the bridge circuit to a SCXI 1120 isolation amplifier. LabVIEW virtual instruments (VI's) acquire the data. The voltage difference across the bridge is measured with time using LabVIEW to collect the data. The voltage difference across the bridge will increase as the sensor is being heated. A plot of the voltage difference, ΔV, versus time will show either an initial steep rise or fall, depending on the conditions of the bridge prior to measurement.

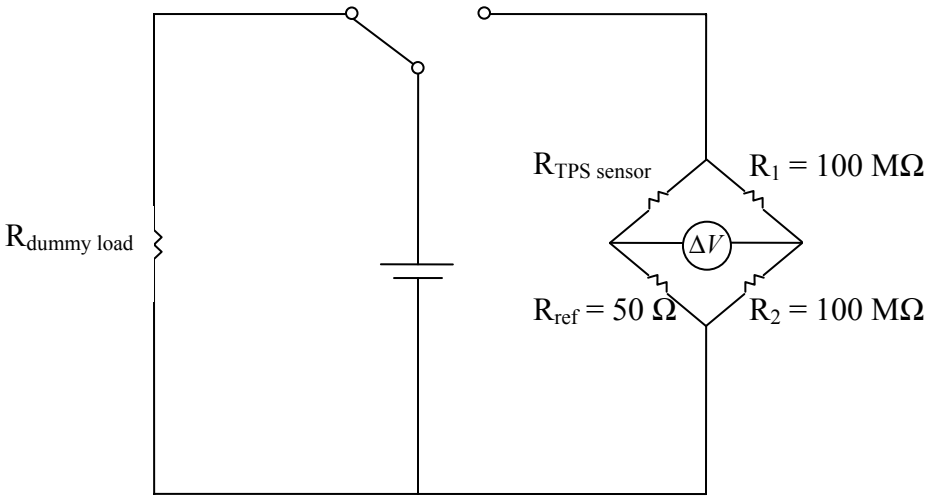

Figure 3-1: Wheatstone bridge circuit, containing the TPS sensor.

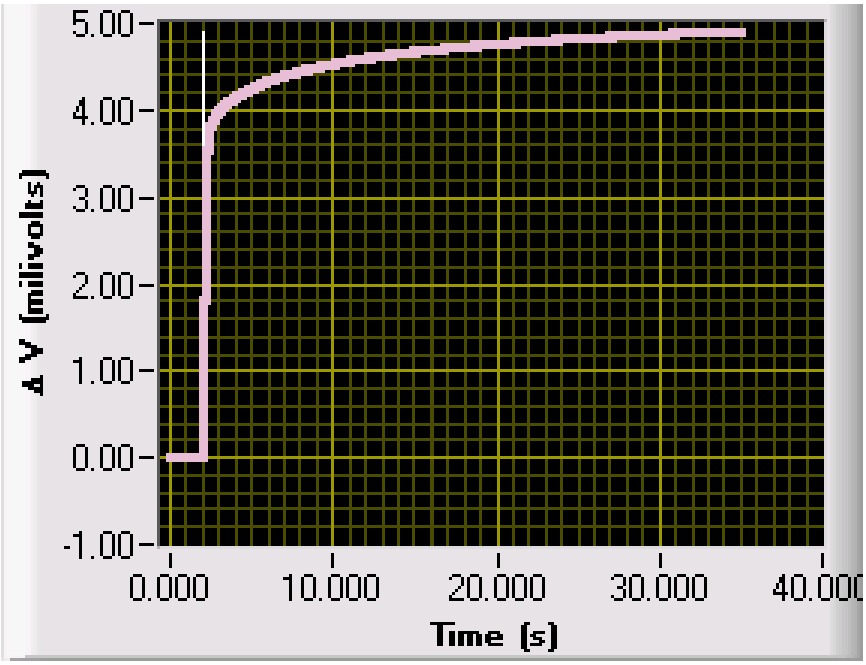

Figure 3-2: Raw data collected and plotted using LabVIEW.

The actual bridge is located in the laboratory while the sensor is generally at a different initial temperature inside the environmental chamber; this initial temperature difference affects the initial state of the bridge. When the temperature of the TPS is lower than the rest of the bridge, a plot of ΔV versus time will show an initial drop, followed by a rise in ΔV as the sensor is being heated. Data points at the beginning, representative of systematic delays, are not used in the analysis. Figure 3-1 shows a typical data set where the voltage difference rises first, indicating that the sensor was initially at the same or greater temperature than the rest of the bridge. The shape of the curve gives useful information about the thermal nature of the sample and only this portion of the data is actually used in the analysis.

The voltage data, ΔV versus time, is used to calculate the resistance of the sensor during the transient heating through the following equation (derivation in appendix B.1):

$$R_{sen} = R_{ref}\left[\frac{1}{\frac{1}{2} - \frac{\Delta V}{V_{tot}}} - 1\right]. \qquad \textbf{(3-1)}$$

R_{ref} is a constant at 50 Ω. ΔV is the voltage difference across the bridge measured with time, and V_{tot} is the total voltage applied to the bridge from a power supply, which is also recorded during the measurement.

The power output to the sensor is calculated using the following equation:

$$P = \frac{V_{tot}^{\ 2} R_{sen}}{\left[R_{sen} + R_{ref}\right]^2}. \qquad \textbf{(3-2)}$$

When voltage is applied to the TPS element, the first points seen in the voltage rise are representative of the heat flow through the insulating layers of the TPS element. The exact time of when the heat flow actually penetrates to the test sample is unknown. Due to the time it takes for the heat flow to penetrate thermal barriers between the heated portion of the TPS element and the test sample, a time correction, t_c, is applied to account for this delay [20].

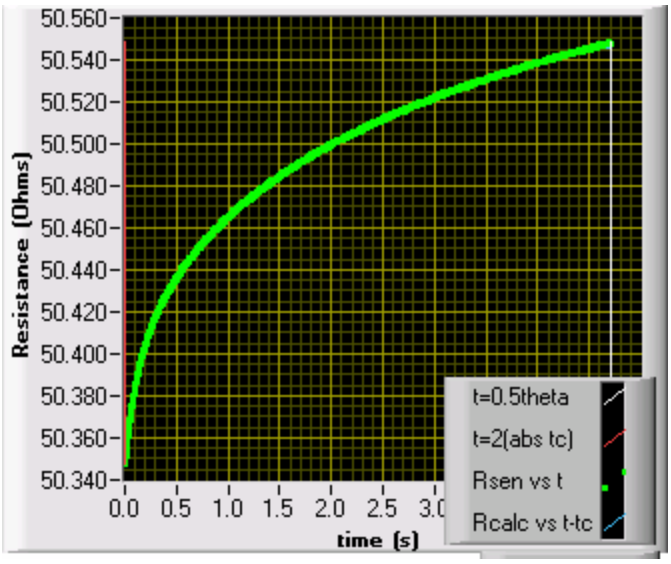

Figure 3-3: Resistance versus time data fit to a second order polynomial in the range of data t = 2 t_c to ½ θ.

The data used to find the time correction, t_c, is defined by the range of 2 t_c to ½ θ. θ is a function of the thermal diffusivity, α (equation (2-4)). Since α is also a property to be determined, an initial guess of α must be made in order to determine t_c. t_c is changed to fit the resistance data (R_{sen}) versus time to a second order polynomial in $(t - t_c)^{1/2}$ given by equation (2-23) in the range of data mentioned above (see Figure 3-3).

The time correction, t_c, is used to adjust the time data. The intercept, R_0, obtained from fitting the data to equation (2-23) is used to calculate the temperature rise of the TPS during the transient heating using equation (2-8).

The manufacturer of the TPS, Vishay Micro-Measurements, supplies equations to describe the behavior of the sensor and are given by following polynomial equations:

$$T(R_{sen}) = A' + B' R_{sen} + C' R_{sen}^{\,2} + D' R_{sen}^{\,3} + E' R_{sen}^{\,4} + F' R_{sen}^{\,5} + G' R_{sen}^{\,6}, \qquad \textbf{(3-3)}$$

$$R(T) = A + BT + CT^2 + DT^3 + ET^4 + FT^5 + GT^6, \qquad \textbf{(3-4)}$$

where the constants were determined for a temperature range of -195 ^{o}C to +260 ^{o}C.

The temperature coefficient of resistivity (TCR) is determined from equation (2-9), using the empirical equations above and used as:

$$TCR = \frac{B + 2CT + 3DT^2 + 4ET^3 + 5FT^4 + 6GT^5}{A + BT + CT^2 + DT^3 + ET^4 + FT^5 + GT}. \qquad \textbf{(3-5)}$$

The temperature rise in the TPS can then be calculated by rearranging equation (2-8) as:

$$\Delta T(\tau) = \frac{R_{sen} - R_0}{(TCR)R_0}, \qquad \textbf{(3-6)}$$

using the *TCR* calculated with equation (3-5) and the R_0 value obtained during the determination of t_c.

As mentioned in section 2.3, an approximation of the function $H_s(\tau)$ can be made using a time correction and the function $H(\tau)$ as was done in analyses utilizing the hot disk configuration

of the TPS. An attempt was made at solving the equations needed to determine $H_s(\tau)$ but, even with the use of software designed to do numerical integration, the solution was difficult to determine. Because an approximate solution with a correction was seen to give good results [5], this was used in determining the thermal properties reported herein. In later work, if determined necessary, the "more" exact solution may be used. $H_s(\tau)$ takes into account the insulating created by the Kapton between the strips while $H(\tau)$ assumes that the conducting pattern is a solid square of nickel. Even $H_s(\tau)$ is partly an approximation (albeit a better one) since it treats the conducting pattern as strips.

An empirical formula was determined for values of τ ranging from 0 to 5. Equation (2-11) was solved numerically using Mathematica® (see appendix B.1.2 for the values) for the aforementioned values of τ and the constants of the polynomial were determined using Microsoft Excel. $H(\tau)$ values are calculated for the analysis with the following equation using τ values calculated with the corrected time:

$$H(\tau) = C_1 + C_2\tau^{1/2} + C_3\tau + C_4\tau^{3/2} + C_5\tau^2 + C_6\tau^3 \quad . \qquad \textbf{(3-7)}$$

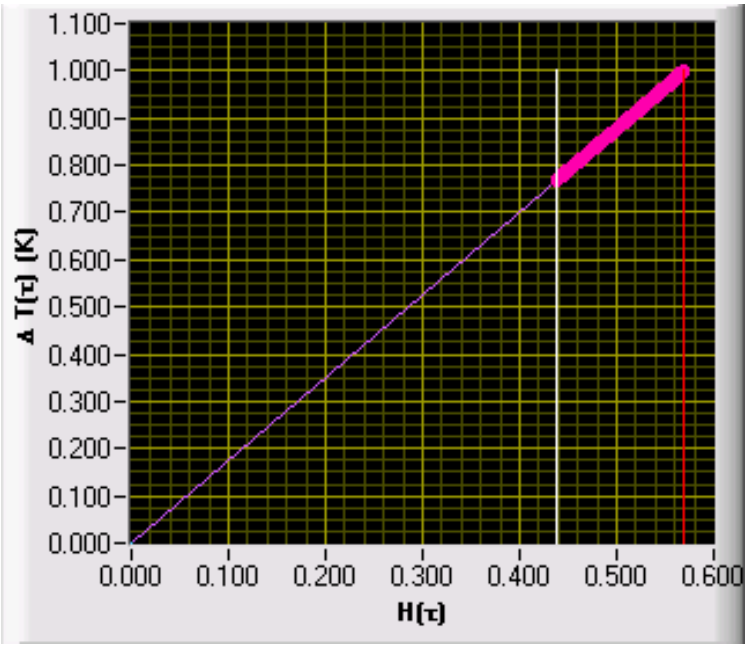

Figure 3-4: ΔT versus H(τ) data fit to a straight line through the origin.

Through equation (2-18), a linear relationship exists between $H(\tau)$ and ΔT. In an iterative process, the thermal diffusivity, α, is changed to optimize the fit of ΔT versus $H(\tau)$ to a straight line through the origin using the numerical Golden Section method. α is chosen based on the value giving the lowest mean squared error (mse) of the data fit to the line. Figure 3-4 shows the best fit of the ΔT versus $H(\tau)$ data through the straight line. The slope of this line is used to calculate the thermal conductivity by rearranging equation (2-18) as:

$$k = \frac{P_{ave} s}{4\pi^{1/2} a_{1/2} (slope)}. \qquad \textbf{(3-8)}$$

P_{ave} is the average of the power calculated with equation (3-2). The half width of the sensor, a, is adjusted by a correction factor to account for the assumptions made in deriving the model used for analysis. The correction is applied as follows:

$$a_{1/2} = \frac{a}{\sqrt{c.f.}}. \qquad \textbf{(3-9)}$$

$2a$ is the nominal size of the conducting pattern of the TPS. A correction factor (*c.f.*) of 0.75 was used in the analysis, giving values for glycerol, water, and ice closest to literature values. The value represented by s takes into account the fact that the TPS is not attached to a perfect insulator. Realistically, some of the power supplied to the TPS dissipates into the PVC backing. s is between 1 and 2 depending on whether the TPS is surrounded on both sides by the sample of interest or if the sample contacts only one side of the TPS with a perfect insulator on the other, respectively. The s-value is determined by the following equation:

$$s = \frac{2 * k}{(k + k_{PVC})}. \qquad \textbf{(3-10)}$$

Since the thermal conductivity of the sample is used to determine s, a new value of thermal conductivity is calculated using the s-value, which is repeated until the old and new value of k agree to within 0.000001 W/mK.

The information rich region of the data is used to determine the thermal diffusivity and here defined by where t = ½ θ to 1½ θ. Beginning data is eliminated because the temperature drop across the insulating layer is not yet constant, which is an assumption of the analysis developed above. After a certain time, the temperature increase of the TPS becomes nearly constant and no longer provides insight into the thermal behavior of the sample material and therefore data after 1½ θ is not used in the analysis.

Because the α-value used to determine t_c was initially an approximation, the newly determined α-value is used to determine t_c again as well as another α - value. This process is repeated until the old and new values of α agree to within 1×10^{-10} m^2/s.

3.2 EXPERIMENTAL IMPROVEMENTS

Past measurement and data collection utilized a Keithley 2000 multimeter, a GPIB board to couple the Keithley to a laboratory computer, and LabVIEW for data acquisition, signal conditioning and file conversion. The TPS was part of the same Wheatstone bridge shown above but was connected to a manual switch. To take thermal property measurements during hydrate formation and dissociation, the experiments needed to be strategically planned so that someone was available to take the measurements during pertinent times of the experiment, which can span a week or more. This process was not only inconvenient but it limited the information that was attainable from the experiments to times when someone was available. Data collection was also limited to about 100 samples per second with the Keithley multimeter. To determine the thermal properties from the data collected, Microsoft Excel spreadsheets were used to process the data. Some portions of the data processing were automated with macros and Visual Basic but a majority of the data handling required user interaction. This was tedious and required a lot of time to obtain results. The Excel files, containing the relevant experimental data and calculated thermal properties were large and required a lot of storage space. While using Excel for data processing was somewhat sufficient for the size of the data files collected using the Keithley and GPIB board, the new capability to obtain 1000 samples or more per second using National Instruments components, made the files too large for Excel to handle. Recognizing these

inadequacies, the system was redesigned and the data analysis program was rewritten in LabVIEW.

components. The data acquisition and data analysis described above are both accomplished using National Instrument's software, LabVIEW. The modifications and improvements to the system have allowed measurement initiation and data collection to be automated. The number of measurements desired and the time between the measurements can be specified.

Only after the thermal properties are known, can changes and adjustments be made to the measurement such as increasing or decreasing the voltage supplied to the TPS, the frequency of the measurements, or the maximum required transient heating time. A program to process data immediately was, therefore, pertinent to efficient experimenting. The capabilities of LabVIEW will allow results from the measurements to be obtained right away and be used to adjust parameters to improve the next measurement.

3.3 EXPERIMENTAL SETUP

3.3.1 High-Pressure Variable-Volume Viewcell (HVVC)

The HVVC, used for hydrate formation, has been described elsewhere [24] and used to form methane hydrates for thermal property measurements [25]. The HVVC is rated at 69 MPa (10,000 psig) at 25.0 ^{o}C, and has a working volume of 7 cm^3 to 38 cm^3. The internal piston can be used to change the pressure or volume inside the HVVC. The stainless-steel bottom, used in the thermal property measurement experiments, can be replaced with a glass or sapphire bottom to allow visual observation of the cell contents during an experiment. In this case, however, thermal property measurements cannot be made.

When performing thermal conductivity measurements in the HVVC, a small holding container with a transient plane source (TPS) element at the bottom is used to retain the sample around the TPS. Figure 3-5 shows the HVVC with the holding container. The previous setup utilizing a smaller container is also shown. Some problems in the previous design included loss

of sample, it was not detachable from the HVVC stainless steel base, and sample recovery was not possible.

During experiments, the pressure and temperature of the gas phase in the HVVC are monitored with a digital Heise gauge and platinum RTD probe, respectively.

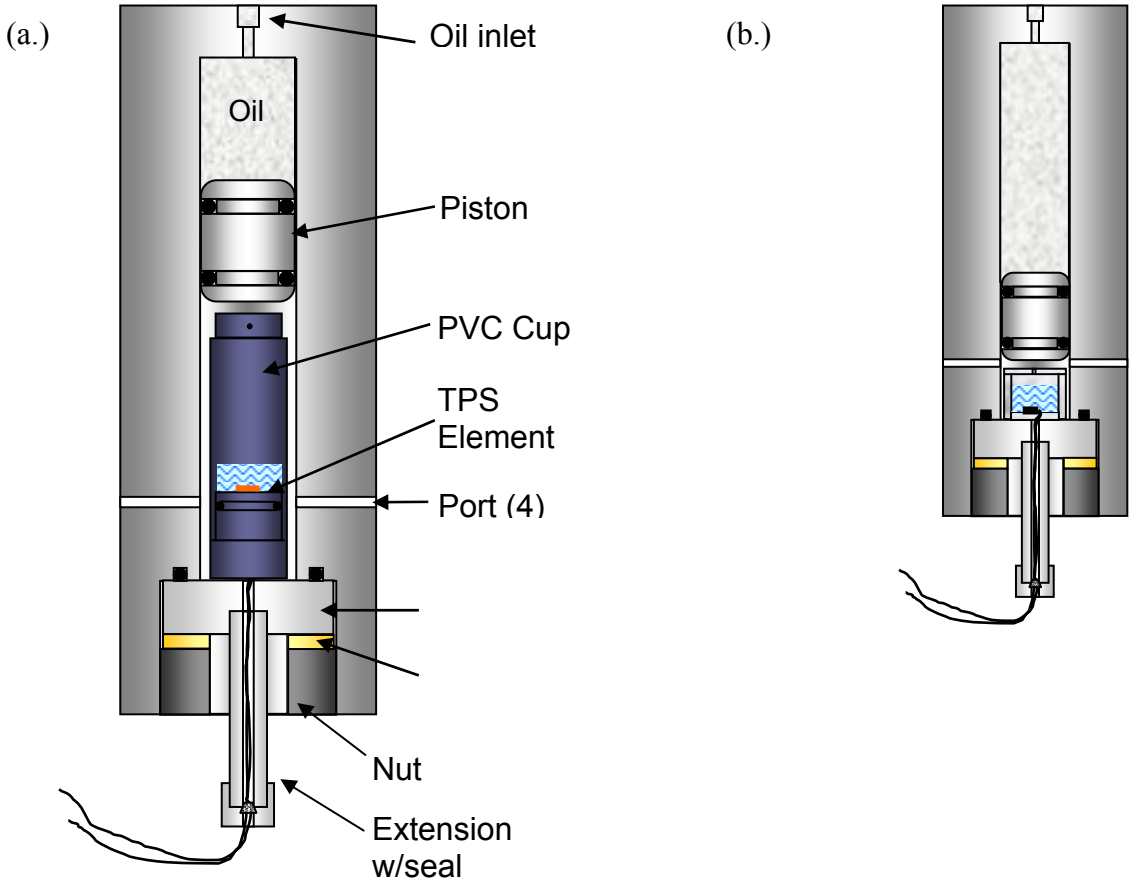

Figure 3-5: (a.) Newly designed experimental system, (b.) System containing old cup.

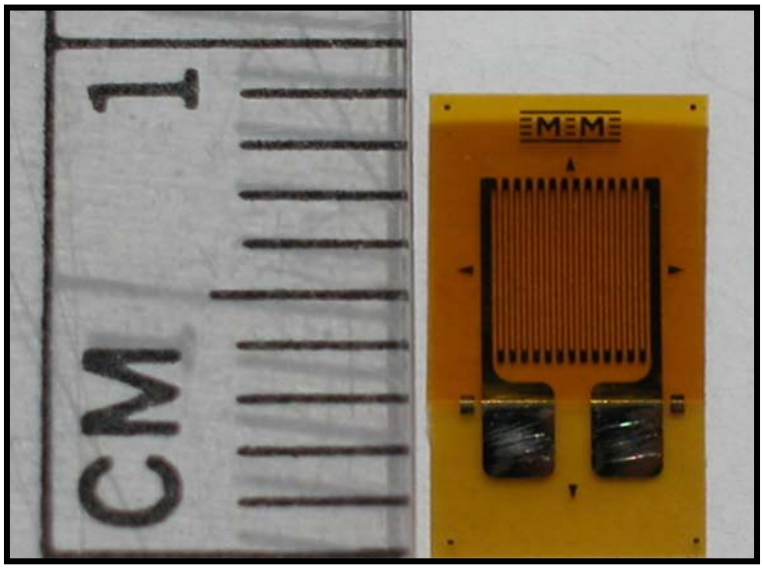

Figure 3-6: Vishay Micro-Measurements precision strain gauge used for thermal property measurements.

3.3.2 Transient Plane Source (TPS) Cup Assembly

Thermal property measurements are made possible with a transient plane source (TPS) element attached to polyvinyl chloride (PVC) for support. The TPS element used in the experiments described is a commercially available precision strain gauge from Vishay Micro-Measurements Group, Inc. The TPS element is located at the bottom of a cup-like container (hereby referred to as "cup") so that the sample to be measured is in good contact with the TPS element.

The TPS (Figure 3-6), approximately 3 mm^2, consists of a thin foil heater, made by depositing a narrow strip of high-purity nickel in a serpentine square pattern on a Kapton (polyimide) substrate. The exposed heater surface is coated with a thin film (0.03 mm) of Kapton, resulting in a robust, flexible heating element, which can be used on electrically conducting samples. The overall thickness of the gauge is less than 50 μm, with a working temperature range of about 78 K to 505 K. The TPS is part of a Wheatstone bridge whereby measuring the voltage difference across the bridge during a transient heating allows the temperature rise in the heating element to be calculated. The temperature rise history of the TPS,

along with the temperature coefficient of resistivty (TCR) of the nickel, allows determination of the thermal properties of the sample in contact with the TPS.

In some preliminary experiments problems in the experimental setup were addressed with the redesigned cup assembly. During methane hydrate formation and dissociation experiments where thermal property measurements were taken, the old cup that was used did not contain the water when hydrates decomposed. After subsequent formation and dissociation cycles, the thermal conductivity values became lower and lower as sample was lost from the cup. Upon disassembly, it was seen that all of the sample was outside the cup. The lid was not secure enough to contain the sample. Power was supplied to the TPS via wires that ran through fittings and the viewcell bottom. Though the current experimental setup utilizes this same method of wiring, the old cup was directly connected to the wires. The cup was therefore attached to the viewcell bottom via the wires but was not secured to the viewcell bottom otherwise. Not only did this require cutting wires and soldering to replace the cup but the cup could easily tip while inserting and removing it from the viewcell. Accuracy was limited in weighing the sample because the viewcell bottom, fittings, and cup were all one entity. The sample could not be removed easily from the cup, especially without disturbing the sample and verification of the

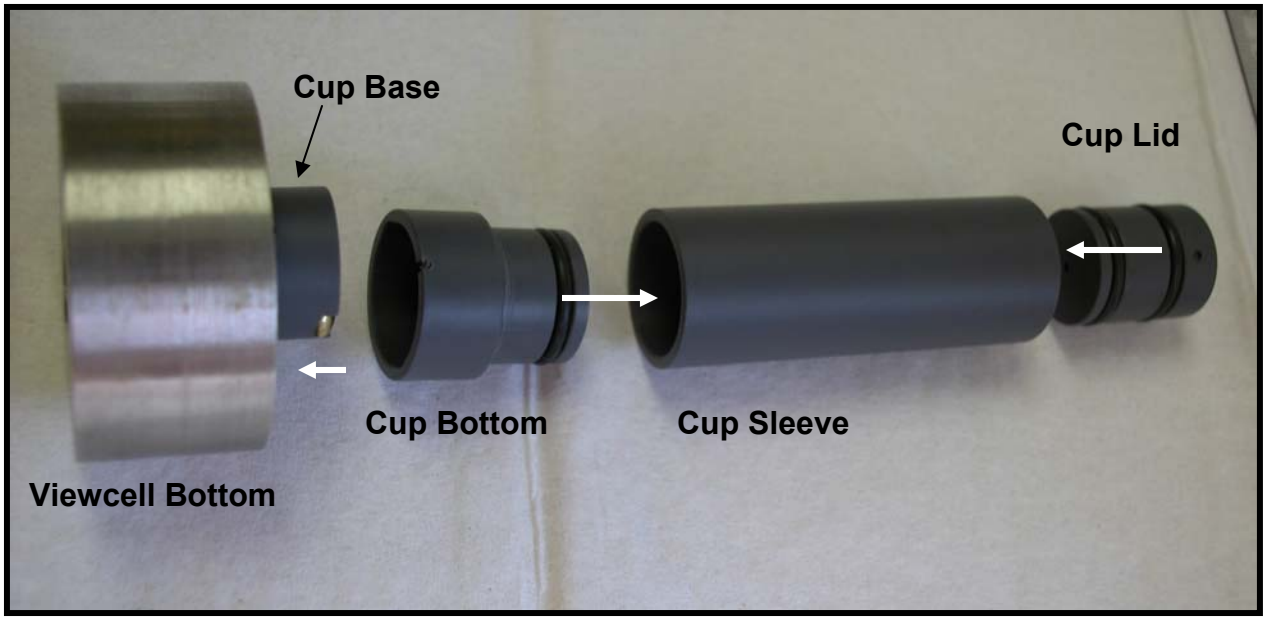

Figure 3-7: Disassembled Cup.

sample / TPS element contact was impossible. With these problems and inadequacies, the TPS / cup assembly was redesigned.

The redesigned cup, machined from PVC, allows for sample recovery when additional analysis is required or desired on the sample. It successfully contains the sample as well, which was one objective in its redesign. The disassembled cup is shown in Figure 3-7. The cup bottom contains the TPS element and is removable from the cup sleeve for easy sample recovery and verification of the TPS contact with the sample. The cup sleeve can be easily machined and its height reduced or increased to change the capacity of the cup. The lid contains a vent, angled at 90 degrees, to allow methane into the cup for hydrate formation but seals with o-rings to contain the sample, even during hydrate dissociation. The cup lid can be pushed with the piston inside the HVVC to compact the hydrate sample, however this was not done in the work reported here.

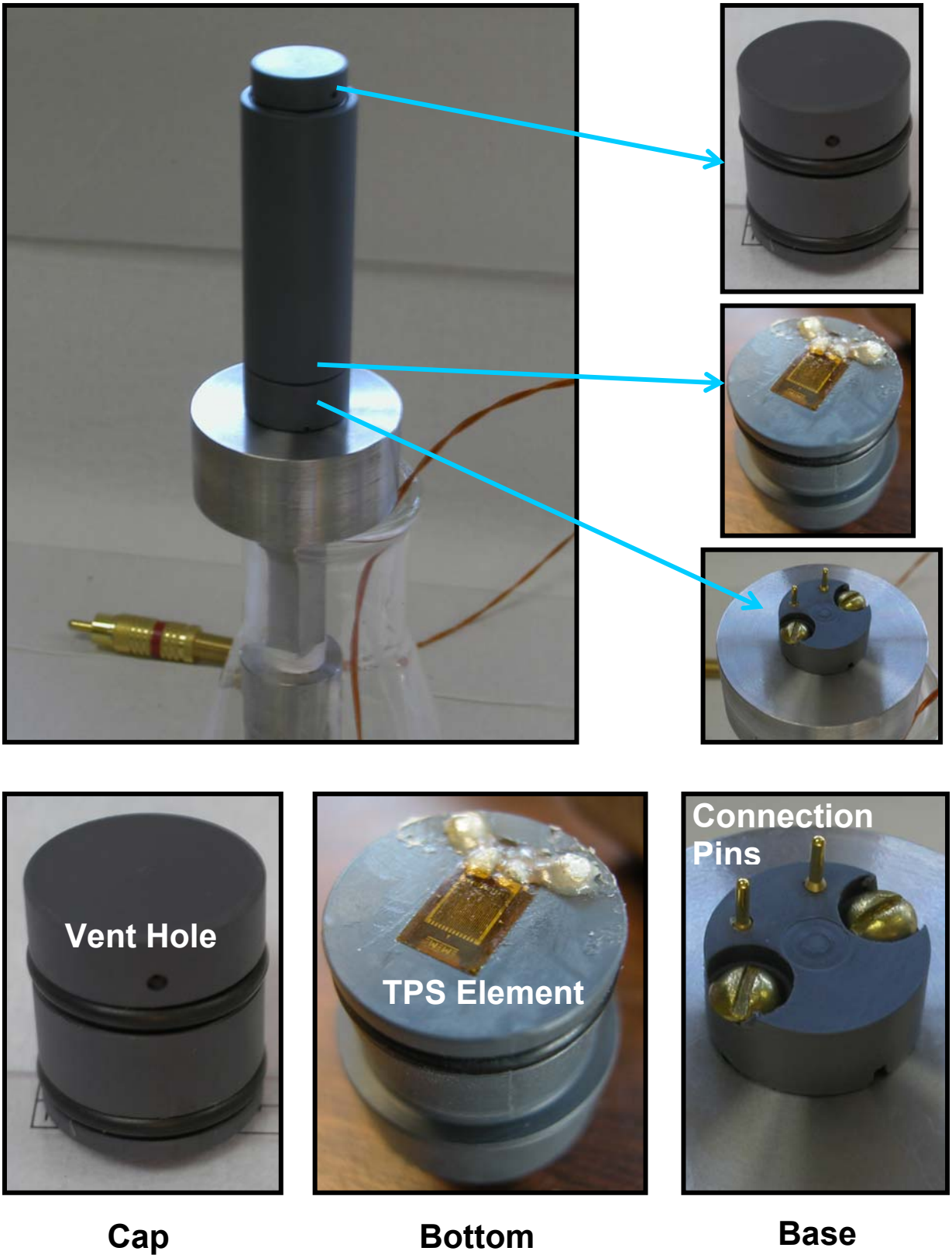

Figure 3-8: Details of the TPS Cup Assembly.

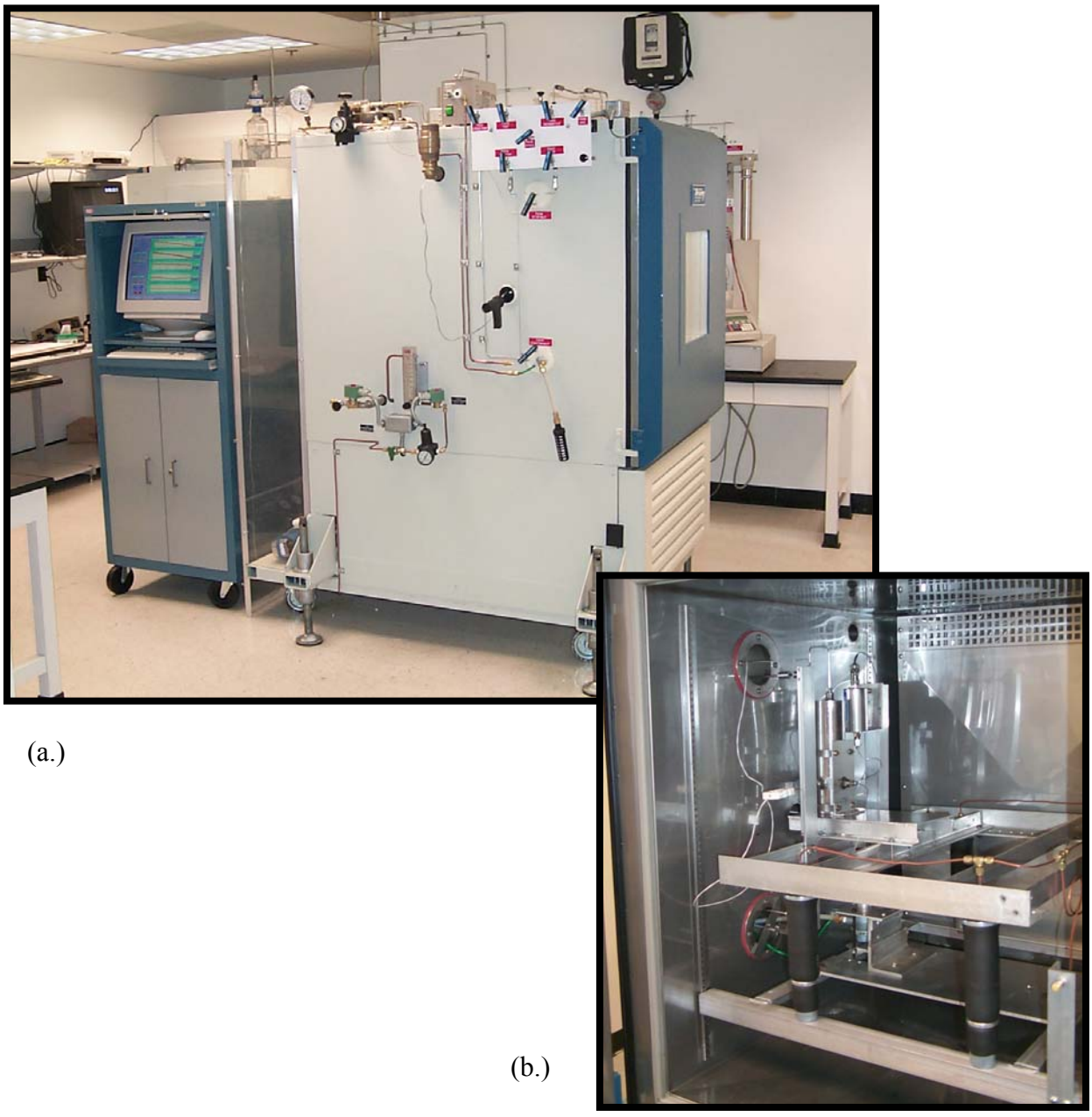

(a.)

(b.)

Figure 3-9: (a.) Environmental chamber and computer system, (b.) HVVC mounted inside chamber.

The entire cup assembly is secured to the HVVC bottom via a base which is screwed into the HVVC bottom. By slipping the cup over the base, not only is the cup secured but it allows connection to the power supply through connectors located on the cup bottom and cup base. The cup is slipped inside the HVVC for experiments to allow thermal property measurements during hydrate formation and dissociation cycles.

3.3.3 Environmental Chamber

A Tenney Environmental T20S chamber houses the HVVC during experiments (Figure 3-9). With a 20 ft^3, explosion-resistant interior, methane hydrate formation experiments can be carried out. The environmental chamber provides temperature control to within 0.1 K and can be programmed for temperature ramp cycles and soak intervals. ISCO syringe pumps are used to control the piston in the HVVC used for pressurizing the viewcell by adding or removing oil from behind the piston.

3.4 EXPERIMENTS

For the experiments described below, water, purified by reverse osmosis and ion exchange to 18 MΩ-cm and methane, Matheson research grade (99.999%), were used to form methane hydrate unless otherwise noted.

In experiments involving thermal property measurements, the cup assembly with the TPS element was filled with water and placed inside the HVVC. The HVVC was pressurized using methane and, in some experiments, the piston. The temperature was cycled down and up at a rate of 1 K per hour to form and dissociate hydrates. During the temperature ramps, thermal property measurements were taken.

To obtain thermal property data, a small voltage (~ 1 V) was applied to the TPS element to raise the temperature of the sample about but not more than 1 K so that the sample was unaffected. During the transient heating, the voltage difference across the Wheatstone bridge was recorded at a rate of 1000 samples per second.

The pressure and temperature were recorded at a rate of 1 sample per minute. A plot of the pressure versus the temperature shows hydrate formation with a drop in the pressure and hydrate dissociation indicated by a sudden increase in the pressure. In all hydrate formation experiments, the hydrate dissociation correlated well with dissociation equilibrium data [1].

Initial experiments were done to make visual observations of the hydrate formation and dissociation since this is impossible when taking thermal property measurements. By better understanding the physical phenomenon that was occurring inside the HVVC and cup, experimental improvements could be made. In the first experiment described pure methane hydrates were formed and dissociated. A significant finding from this experiment was that the cup needed to be redesigned since most of the sample was lost during the experiment. In the next experiment, methane hydrates were formed from a sand and water mixture. This was insightful to see how hydrate formed and dissociated in the pores created by the sand. The sample was not well contained in this experiment either and, with the observations made, the new cup was designed so that thermal property measurements could be made on hydrate and sediment samples as well.

After redesign and automation of the experimental setup and redesign of the cup, measurements were made on water, ice, and glycerol which all have well known thermal properties. Water and ice are also present during the formation and dissociation of methane hydrate so it was important to know these values so that when hydrate formed it could be distinguished. Glycerol is a good standard because is does not convect at room temperature and even at elevated temperatures. The problem encountered with glycerol, however, is that it hydrates quickly, giving falsely high thermal conductivity values for glycerol. Precautions were taken to ensure that the measurements of glycerol were taken on anhydrous and pure glycerol samples.

Two successive experiments were done to take thermal property measurements of methane hydrate using the new TPS cup assembly. In the first experiment methane hydrate was formed from water and methane, frost was used instead of water in the second experiment. In both experiments, the methane uptake was small as indicated by almost no change in pressure. Throughout both experiments the thermal conductivity values were either that of water or ice. The experiment starting first with a porous mixture of frost was done to reduce suspected

limitations due to diffusion. In this experiment it is possible, however, that most of the frost sample melted even before pressurization with methane, thereby not enhancing diffusion.

The thermal property values are most influenced by the material closest to the TPS element and the thermal conductivity values obtained are indicative that hydrate did not form far enough down in the sample to influence the thermal conductivity. Since the new TPS cup assembly was successful in containing the sample, the surface area of exposed water or ice that could react with the methane was reduced and the depth of the sample was also greater.

It was suspected that hydrate was forming in the vent hole of the cup and preventing or reducing methane exposure to the water inside the cup. To rule out any limitations caused by the cup lid, it was left off during one experiment. It was only after successive cycles without dissociating the hydrate, that significant hydrate formation was observed. The hydrate was not dissociated until the last cycle upon which some of the sample was lost from the cup since it had no lid. In this experiment the thermal properties of methane hydrates were successfully measured.

The final experiment described below was successful in converting all of the water to hydrate and thermal property measurements were taken of this pure methane hydrate sample. The sample was recovered and Raman spectroscopy was performed on the sample to determine the composition of the portion of the sample in contact with the TPS element.

3.4.1 Experiment T20-006: Methane Hydrate Formation from Water and Methane With Visual Observation of Hydrate Formation and Dissociation

Because experiments involving thermal property measurements need to use the stainless steel bottom of the HVVC instead of the glass bottom, the intent of this experiment was to make visual observations of hydrate formation from methane and water and dissociation of the methane hydrate.

Starting with 0.2546 g of water, placed in a cup made of CPVC tubing with a clear, plexiglass bottom and a PVC lid, hydrates were observed to form and dissociate both visually and from the pressure / temperature data. The cup rested on the glass bottom of the HVVC and activity inside the HVVC was monitored through the viewport by means of a remote video camera and borescope. The HVVC was pressurized with the piston and methane to about 13 MPa. Hydrate did not form in the cell until ice was observed visually, at a set point of 268 K (-

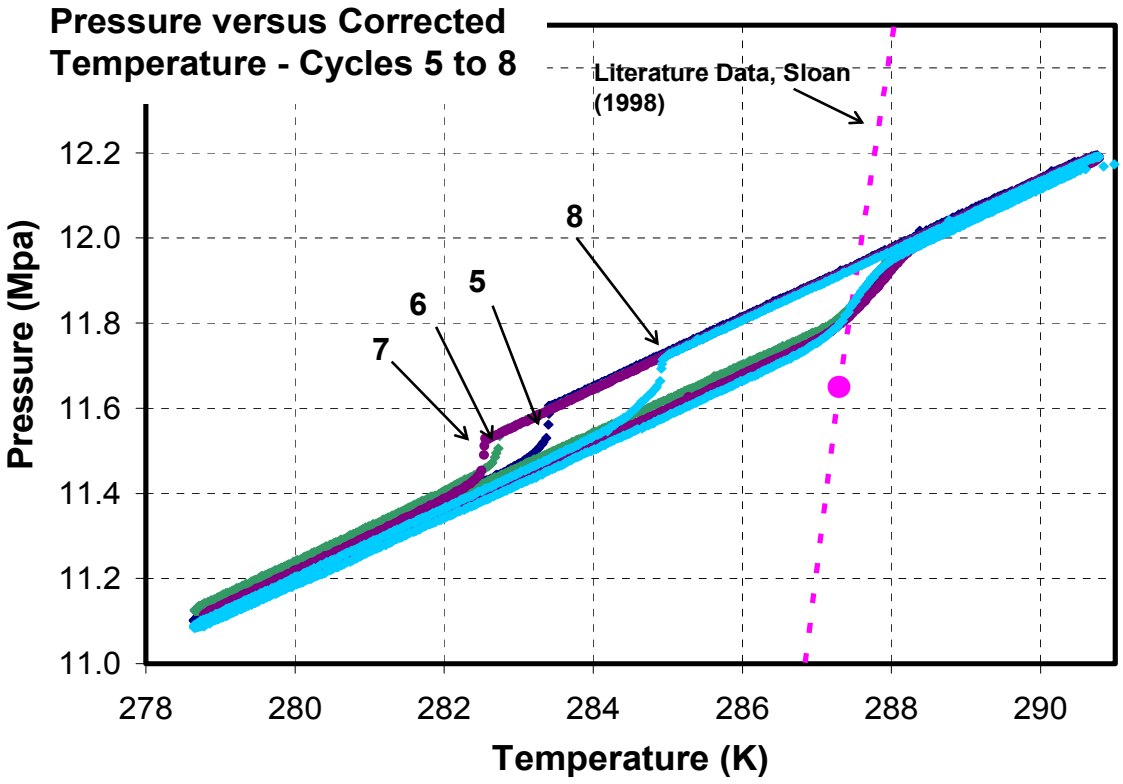

Figure 3-10: Experiment T20-006, A typical pressure versus temperature trace of hydrate formation and dissociation.

5.0 ^{o}C). With subsequent temperature ramps, hydrate formation and dissociation was observed from the pressure / temperature data and visually through the HVVC bottom. By cycling between 278 K (5 ^{o}C) and 291 K (18 ^{o}C), cycles 5 through 8 show a typical pressure versus temperature trace of hydrate formation and dissociation. The hydrate dissociation equilibrium point of all four cycles corresponded well with literature data from Sloan [1]. Upon disassembly of the HVVC, no water could be seen in the cup, though water was on the viewcell bottom and the bottom o-ring. Water loss was attributed to degassing, hydrate dissociation, and a poorly secured lid. Lack of water containment from this experiment prompted the redesign of the cup.

In Figure 3-10, the numbers correspond to the cycle which is herein defined by lowering the temperature and raising the temperature with the intent to form and dissociate hydrate, respectively. The pressure versus temperature profile is typical for hydrate formation and dissociation [1]. The dissociation of methane hydrates will follow the same path with subsequent cycles but, as seen in this experiment, the formation equilibrium varies.

This experiment was significant in making improvements to the experimental system, especially the cup which contains the sample. Because activity inside the cup was monitored during the experiment, the cause of sample loss from the cup was determined. Some water was lost from the cup during evacuation of the HVVC to remove air before the methane was introduced. It was also observed that the release of methane during hydrate dissociation caused sample loss from the cup. The cup lid needed to be redesigned to contain the sample but at the same time allow methane to contact the water inside the cup.

3.4.2 Experiment T20-009: Methane Hydrate Formation from Water Saturated Sand and Methane

Since observations of the HVVC contents cannot be made during experiments involving thermal property measurements, this experiment was performed to observe the formation and dissociation of methane hydrates in sediments, the first experiment of this work involving hydrate formation in sediments.

Sand from Lawrence Livermore National Labs was used to make a sand and water mixture. The density of the sand (ρ_{sand}) was determined to be 2.86 ± 0.14 g/ml. The apparent density ($\rho_{app.}$) of the sand was determined to be 1.7137 g/ml. The void fraction (Σ) of the sand was calculated as 0.401 by rearranging the following equation:

$$\rho_{app} = \rho_{air}\Sigma + \rho_{sand}(1-\Sigma). \quad \textbf{(3-11)}$$

The mass of the water needed to completely saturate the sand was about 7 g. (6.9995 g. as calculated for 30.003 g. of sand). The saturation of the sand was calculated as 99.97 %, though water continued to evaporate from the mixture while it was outside the HVVC. Before placing the sample inside the HVVC, the mass of the mixture was 5.396 g.

A small piece of CPVC tubing was placed on the glass bottom of the HVVC with no bottom and no lid and filled with the mixture of sand and water as is seen in Figure 3-11. The activity inside the cell could then be observed through the viewport by means of a remote video camera and borescope. Some water migrated toward the bottom and seeped out onto the glass before inserting it into the viewcell.

The cell was pressurized with methane to about 7 MPa (1000 psig) then with the piston to 14.5 MPa (2087 psig).

During the first cycle problems occurred with a component of the National Instruments hardware. A replacement was obtained and used to record the pressure / temperature data. Hydrate dissociation was observed from the pressure versus temperature data.

The second cycle started at 293 K (20.2 ^{o}C). The temperature was lowered to a set point of 269 K (-4.0 ^{o}C) and soaked for an hour then ramped up to 293 K (20.0 ^{o}C). Hydrate formation was observed in the pressure / temperature data and visually through the viewport. The third and fourth cycles went from 293 K to 275 K (20.0 ^{o}C to 2 ^{o}C) then back to 293 K. A fifth cycle was done in the same temperature range to confirm the results of cycles 3 and 4.

Hydrate formation seemed to continue as the temperature was lowered. The presence of the sand seemed to alter consumption of gas by the water. Whereas the absence of sand produces an abrupt drop in pressure, the presence of sand showed a gradual uptake of the methane in most of the cycles (see Figure 3-12).

Figure 3-11: Experiment T20-009. Post experiment picture of the CPVC tubing on top of the HVVC glass bottom. The water in the sand has already evaporated.

Upon dissociation, the equilibrium dissociation point for all cycles matched well with literature values [1]. As the temperature was increased to near the dissociation, decreases in the pressure indicated additional hydrate formation.

After taking the sample out of the cell, the sand mixture was highly porous and had been pushed out from the bottom and top of the CPVC tubing. This phenomenon probably occurred during hydrate dissociation as the gas was being released from the methane hydrate (see Figure 3-13). The voids extended throughout the sample indicating that hydrate had formed even in the center of the sand sediment.

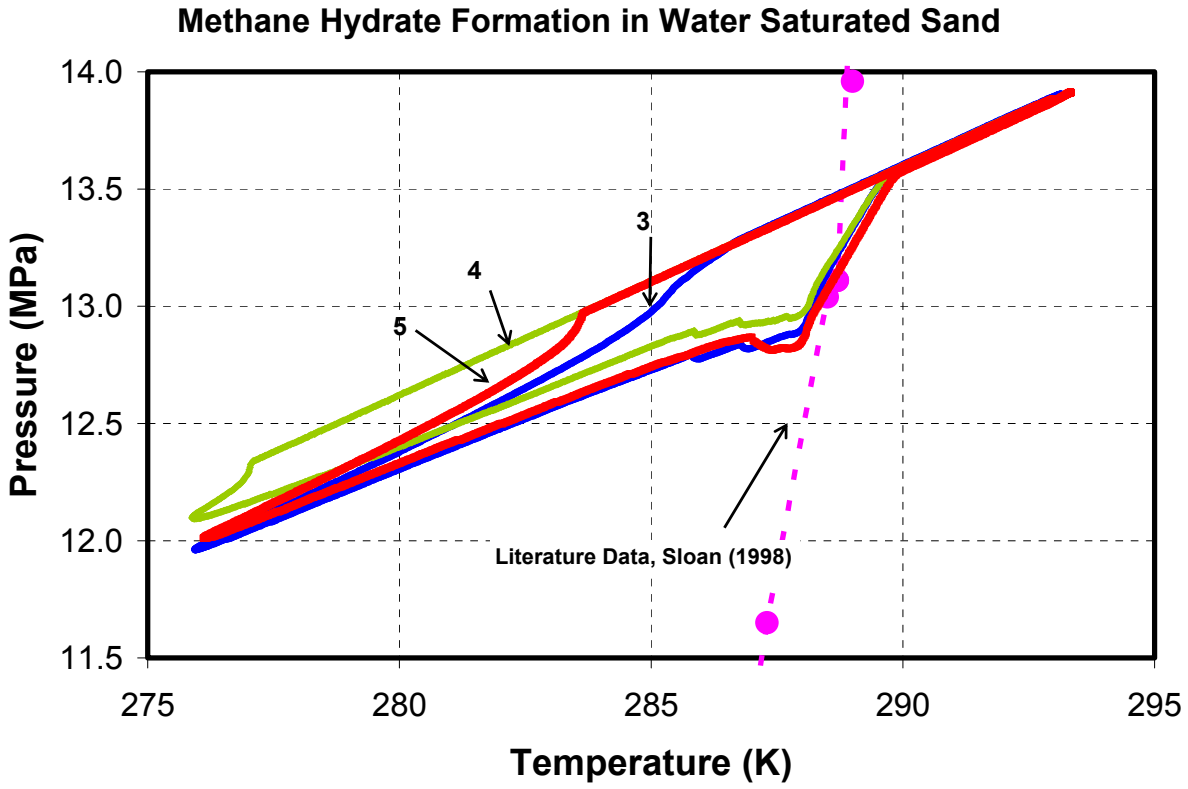

Figure 3-12: Experiment T20-009, Formation of methane hydrates in sediments.

Figure 3-13: Experiment T20-009, Post experiment picture showing the eruption of the sand mixture from the CPVC tubing.

3.4.3 Experiments T20-010 and T20-011: Thermal Property Measurements of Glycerol

After the last two experiments described, extensive changes were made to the experimental setup. The thermal property measurements were automated as described in section 3.2 and the TPS cup assembly was redesigned. To validate measurements with this new experimental setup, glycerol was used as a standard because of its high viscosity.

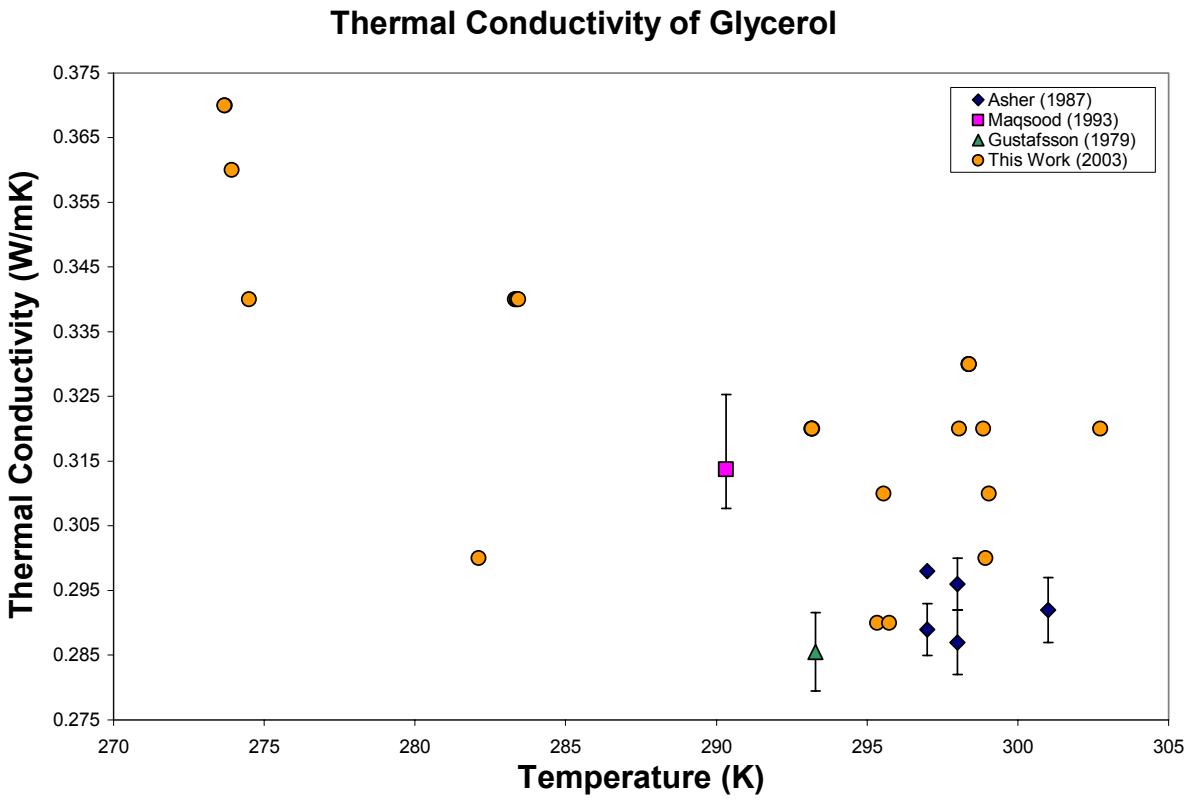

Figure 3-14: Experiments T20-010 and T20-011, thermal conductivity of glycerol with literature values.

Anhydrous, 99.5% GC grade, glycerol containing less than 0.1% water was used to calibrate the TPS element and experimental system. Glycerol was placed in the thermal conductivity measurement cup and inserted into the HVVC with a silica gel drying packet and placed in the environmental chamber so that thermal conductivity measurements could be made at various temperatures. The silica gel packet was used to reduce hydration of the glycerol sample.

The thermal conductivity values of the glycerol were higher than most of the other literature values obtained at room temperature. One difficulty in determining the thermal properties of the sample from the data is determining when the power supplied to the TPS has penetrated to the sample. The range of data used in determining the thermal properties, itself influences the thermal property values obtained. Due to the insulating layers of the TPS element and systematic errors, the transient behavior in the ΔV versus time data at the very beginning

will cause errors in the data analysis. Additionally, after a certain time the voltage difference across the bridge approaches a steady-state value and no longer gives useful information regarding the thermal properties of the sample (refer to section 3.1). This was one problem encountered when analyzing the data and may be the reason why the values vary so much and why the values are higher than expected.

It has not been determined whether the high thermal conductivity values are due to a numerical problem in the data analysis program or due to hydration of the glycerol sample, which would cause an increase in the thermal conductivity of the sample.

Figure 3-14 shows the thermal conductivity values obtained for glycerol from this work and literature values obtained by other investigators. Most of the thermal conductivity values obtained around room temperature are higher that the other reported literature values and in this work, the thermal conductivity was seen to increase with decreasing temperature. This trend with temperature has not been confirmed and could be due to a numerical problem in the data analysis.

3.4.4 Experiment T20-014: Thermal Property Measurements of Water at Various Temperatures

During the formation of methane hydrates, water and ice are also present at times. The thermal properties of liquid and solid water are also well known. This experiment was done to obtain thermal property values of water at various temperatures so that the presence of hydrate could be distinguished from that of the water and ice.

The water described above was boiled under vacuum at room temperature for about 10 minutes to remove most of the gas from the water. All subsequent experiments use this water as well. 7.65 mm (0.3012 inches, 1.563 g) of this water was placed in the cup and the cup was inserted into the HVVC. The HVVC was mounted in the environmental chamber so that thermal property measurements could be taken of the water at various temperatures. Thermal property measurements were taken at set points from 283 K down to 263 K (10 ^{o}C, 0 ^{o}C, -5 ^{o}C, -7 ^{o}C, and -10 ^{o}C) and given in Table 3-1.

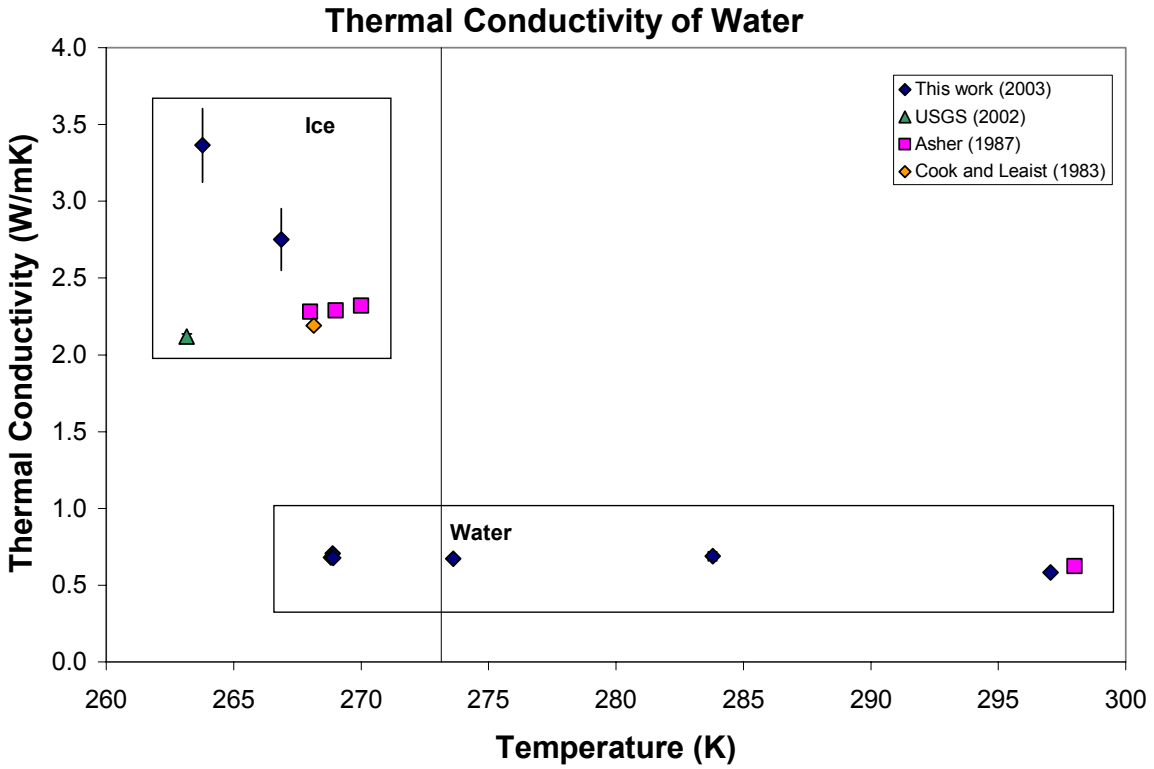

Figure 3-15: Thermal conductivity of water compared with literature values.

Table 3-1: Measured Thermal Property Data of Water (This Work).

Temperature (°C)	State	Thermal Conductivity *k* (W/mK)	Thermal Diffusivity α x 10^7 (m^2/s)
(297 K / 24 °C) 23.91 ± 0.07	Liquid	0.58 ± 0.01	1.98 ± 0.07
(283 K / 10 °C) 10.64 ± 0.17	Liquid	0.69 ± 0.01	1.74 ± 0.05
(273 K / 0 °C) 0.46 ± 0.01	Liquid	0.67 ± 0.02	1.5 ± 0.1
(268 K /-5 °C) -4.28 ± 0.04	Liquid / Solid	0.69 ± 0.02	1.54 ± 0.06
(266 K / -7 °C) -6.29 ± 0.01	Solid	2.75 ± 0.20	4.25 ± 0.85
(263 K / -10 °C) -9.36 ± 0.03	Solid	3.36 ± 0.24	4.0 ± 0.2

At room temperature (23.91 ± 0.07 ^{o}C) and atmospheric pressure the thermal conductivity, *k*, of water was determined to be 0.584 ± 0.006 W/mK. The thermal conductivity of water was nearly constant with temperature as shown in Figure 3-15. When ice formed in the cup, the thermal conductivity rose greatly. The thermal conductivity of ice was determined to be 2.75 ± 0.20 W/mK and 3.36 ± 0.24 W/mK at -7 ^{o}C and -10 ^{o}C, respectively. The thermal conductivity value of ice at -10 ^{o}C is over one and a half times higher than other reported values for ice. Because the portion of the sample in contact with the TPS could not be examined during the measurement, the exact reason for this high value cannot be conclusively determined. It has been observed, however, from this work that trapped gasses in the ice cause unusually low thermal conductivity values of ice. The thermal conductivity values indicated whether ice or water was present in the cup since visual confirmation could not be made.

3.4.5 Experiment T20-015: Thermal Property Measurements of Hydrates Formed from Water and Methane

With the validated experimental setup, this experiment was performed so that thermal property measurements could be taken on a pure methane hydrate sample using the new TPS cup assembly.

Starting with 1.413 g. (6.92 mm) of water (k = 0.63 W/mK), the cell was pressurized with methane to cylinder pressure and then with the piston to about 13 MPa. The temperature was lowered to about 261 K (-12 ^{o}C) and raised to about 293 K (20 ^{o}C). Hydrate may have formed during this first cycle at around 267 K (-6.2 ^{o}C), where a slight drop in pressure occurred (Figure 3-16). Upon heating the sample beyond the dissociation equilibrium point, again, a very slight change (rise) in pressure seemed to indicate hydrate dissociation but so slight that hydrate presence could not be confirmed with the thermal property measurements. The temperature was again lowered to 261 K (-12 ^{o}C) and an estimated 7 % of the water was converted to hydrate based on about a 0.23 MPa (23 psi) pressure drop. Upon heating, hydrate dissociation was observed in the pressure / temperature data with a small rise in pressure around 291 K (17.5 ^{o}C), corresponding to literature data [1].

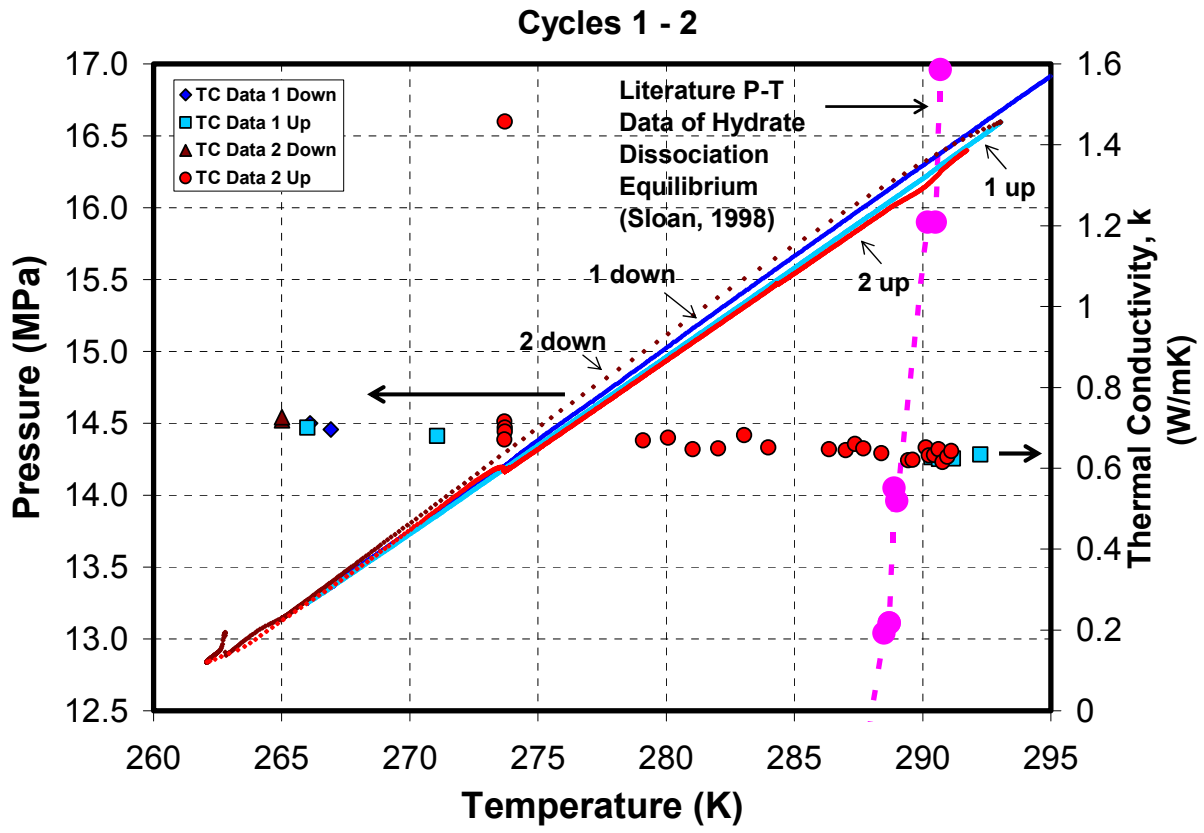

Figure 3-16: Experiment T20-015, Cycle 1 down and up, Cycle 2 down.

The thermal conductivity remained close to that of water (0.605 W/mK at 298 K, CRC Handbook) throughout the experiment, indicating that any hydrate formed in the cup was not near the TPS element. Because of the depth of the water in the cup, and the small surface area exposed to the methane, hydrate formation was limited by diffusion. The presence of some ice was indicated by a thermal conductivity of $k = 1.46$ W/mK at $T = 273.7$ K during the temperature increase of cycle 2. This value is low for ice but the measurement was taken above the freezing point. Liquid water may have been present near the TPS element. Thermal conductivity measurements were taken well below the freezing point of water but, as was seen in earlier experiments, it can be difficult to form ice from such pure water and at these temperatures. The thermal conductivity value obtained for ice was taken during the second cycle.

In Figure 3-16 the pressure versus temperature is shown along with the thermal conductivity values obtained during the experiment shown by the larger points as specified by

the legend. Though it is apparent that any hydrate present in the cup did not form near the sensor, the thermal conductivity values were indicative of the contents of the cell. Note the high thermal conductivity value during the heating of cycle 2, indicating the presence of some ice near the sensor.

3.4.6 Experiment T20-016: Thermal Property Measurements of Hydrates Formed from Frost and Methane

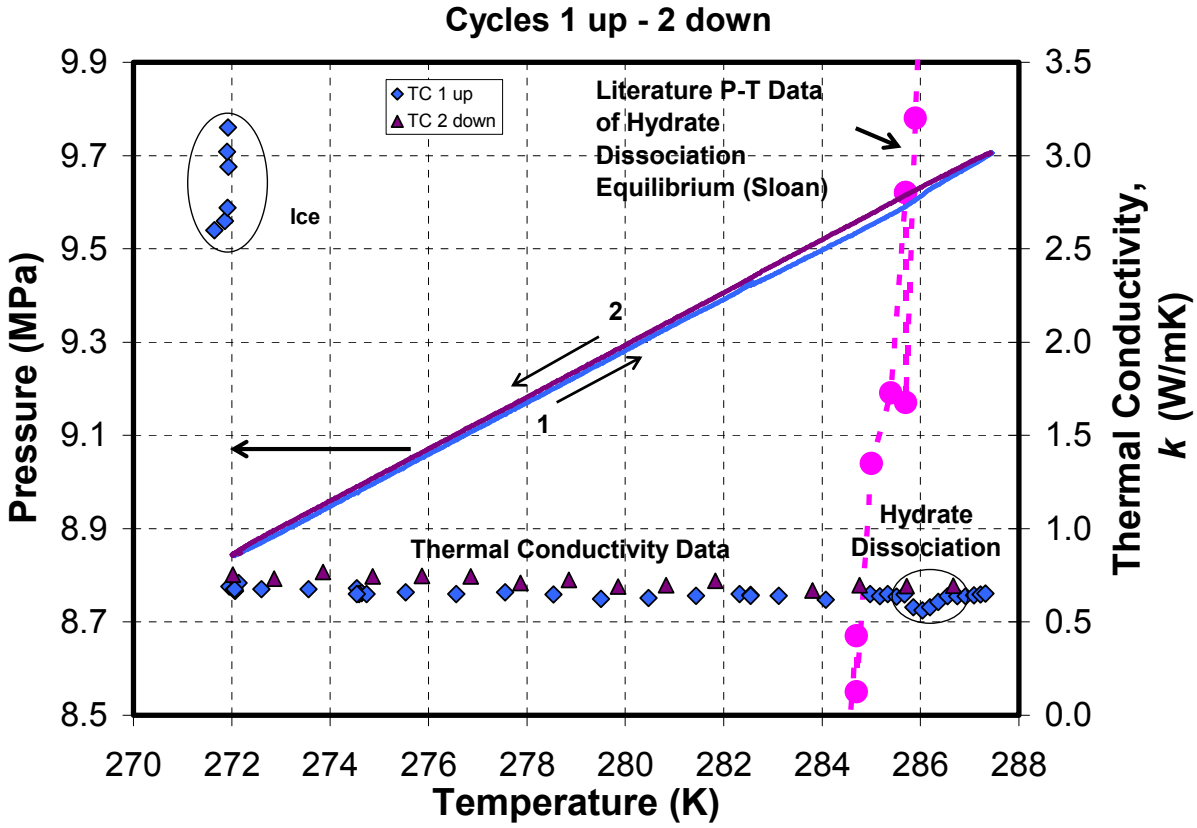

Figure 3-17: Experiment T20-016, Cycles 1 up to 2 down.

Since little hydrate formation was observed in experiment T20-015, this experiment was performed to enhance hydrate formation by starting with frost instead of water. In experiment T20-015, hydrate formation down to the TPS in the cup was thought to be limited by diffusion of the gas down to the water near the TPS. Hydrates have successfully been formed from granular ice and methane [10].

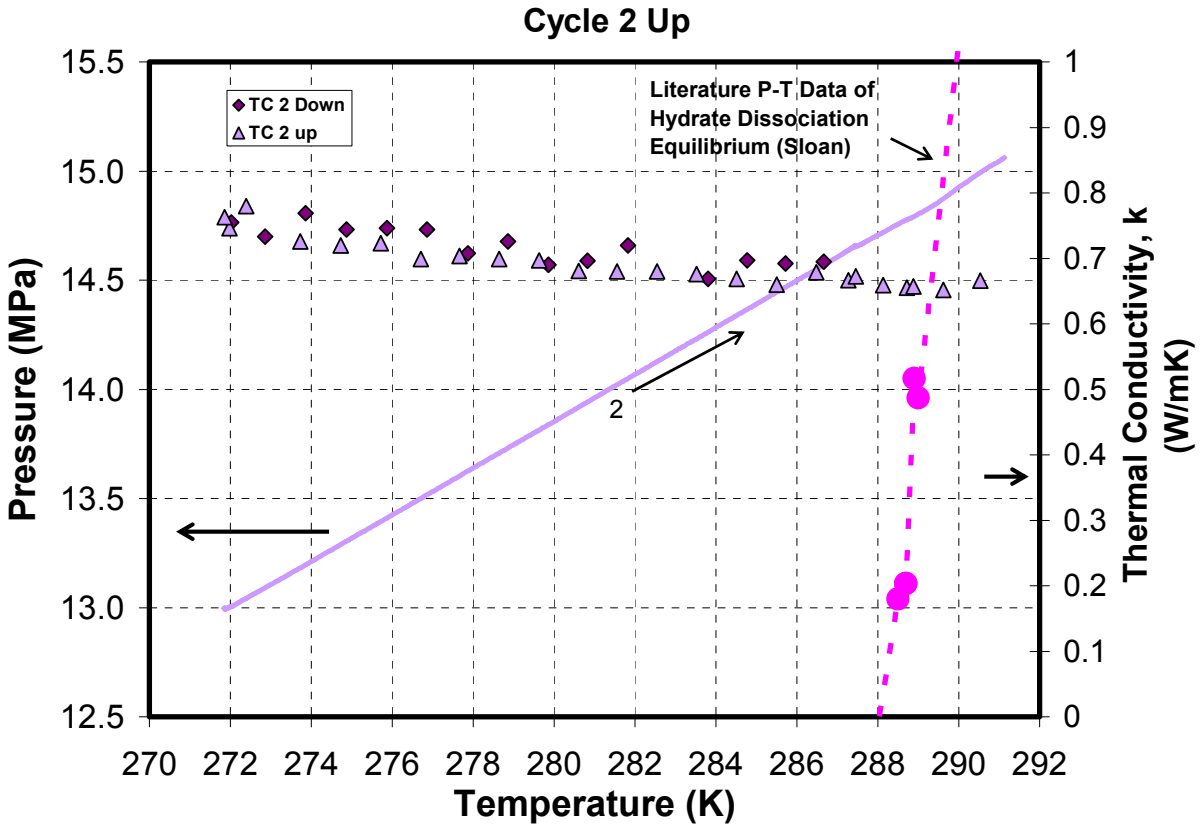

Figure 3-18: Experiment T20-016, Cycle 2 up.

In this experiment, about 1.09 g. of frost, obtained from a freezer at about 203 K (-70 ^{o}C), was used to form methane hydrate. The thermal conductivity of the ice at the start of this experiment was 2.2 W/mK. The cell was pressurized with methane to about 8.8 MPa. After a few temperature ramps between 274 K and 271 K (1.0 ^{o}C and -2.0 ^{o}C), with no change in the thermal conductivity, the temperature was increased from a set point of 271 K to 282 K (-2.0 ^{o}C to 9.0 ^{o}C) and held for about 9 hours during which, additional hydrates formed. The temperature was increased further to a set point of 287 K (14.0 ^{o}C) and hydrate dissociation was observed in the pressure / temperature data by a slight increase in the pressure, corresponding with literature data [1] of the dissociation equilibrium. The thermal conductivity data indicated hydrate dissociation by a decrease during the dissociation (Figure 3-17).

The thermal conductivity values throughout the experiment were close to water, indicating (again) that the water converted to hydrate was not near the TPS. The decrease in thermal

conductivity during hydrate dissociation was probably caused by the release of the gas (observed visually in experiments when the glass HVVC bottom was used) causing mixing in the sample, resulting in heat transport by convection. The gas released from hydrate dissociation may also have come close to the TPS, causing the decrease in the thermal conductivity. The temperature was decreased from a set point of 287 K to 271 K (14.0 ^{o}C to -2.0 ^{o}C) for cycle 2 down. Hydrate formation could not be detected from the pressure and temperature data and the thermal conductivity values were still near that of water.

The pressure of the system was increased with the piston to about 13.0 MPa from 8.8 MPa (Figure 3-18). The temperature was increased from a set point of 271 K to 287 K (-2.0 ^{o}C to 14.0 ^{o}C) at this elevated pressure, where it was held for 3 hours. The temperature was then increased to 291 K (18.0 ^{o}C). At both times in the experiment when the temperature was held for an extended period, a small amount of hydrate formed. During hydrate dissociation of cycle 2 the thermal conductivity decreased slightly, not nearly as much as the first cycle dissociation though.

Little hydrate formed according to the pressure and temperature data. Any hydrate that formed apparently was not close to the TPS according to the thermal property data, however, the thermal conductivity data did indicate the state of the sample and indicated hydrate dissociation.

3.4.7 Experiment T20-017: Thermal Property Measurements of Hydrates Formed from Water and Methane – The Cup Was Used Without the Cap

Because so little hydrate was observed to have formed in the preceding two experiments, the cap of the cup was left off in this experiment to determine if water was condensing in the vent hole of the cap and / or hydrates were forming in the hole, thus reducing or preventing the transfer of methane into the cup.

1.413 g. of water was used in the cup, corresponding to a depth of 6.86 mm (0.27 in.). The thermal conductivity of water at the start of the experiment was k = 0.62 ± 0.02 W/mK. The cell was purged with methane, pressurized to bottle pressure with methane, then pressurized with the piston to about 13 MPa. The temperature was then lowered to a set point of 261 K (-12 ^{o}C) to first form ice. Ice formation was indicated by a rise in pressure as it expanded into a solid. Thermal property measurements were not possible at this temperature, however, because of physical limits set on the bridge. Therefore, ice formation could not be confirmed by the thermal

property data. Additionally, no hydrate was evident from the pressure / temperature data or thermal property measurements. The temperature was increased to a set point of 287 K (14 ^{o}C), right before the dissociation equilibrium point. During this heating, a small amount of hydrate formed once the temperature was near the melting point of ice, indicated by a slight drop in pressure starting around 273 K (0 ^{o}C). All of the pressure data for all cycles is shown in Figure 3-19 along with the corresponding thermal conductivity values.

For cycle 2, as the temperature was decreased to about 274.5 K (1.4 ^{o}C) more hydrate formed. The temperature was then raised to about 287 K (14.0 ^{o}C) and, even more hydrate formed just before the dissociation point. The temperature was lowered to 276 K, then increased to dissociate the hydrate for the third and final cycle.

It was seen from this experiment, that by not dissociating the hydrate with each cycle, hydrate formation was promoted with subsequent cooling. As seen in prior experiments, not

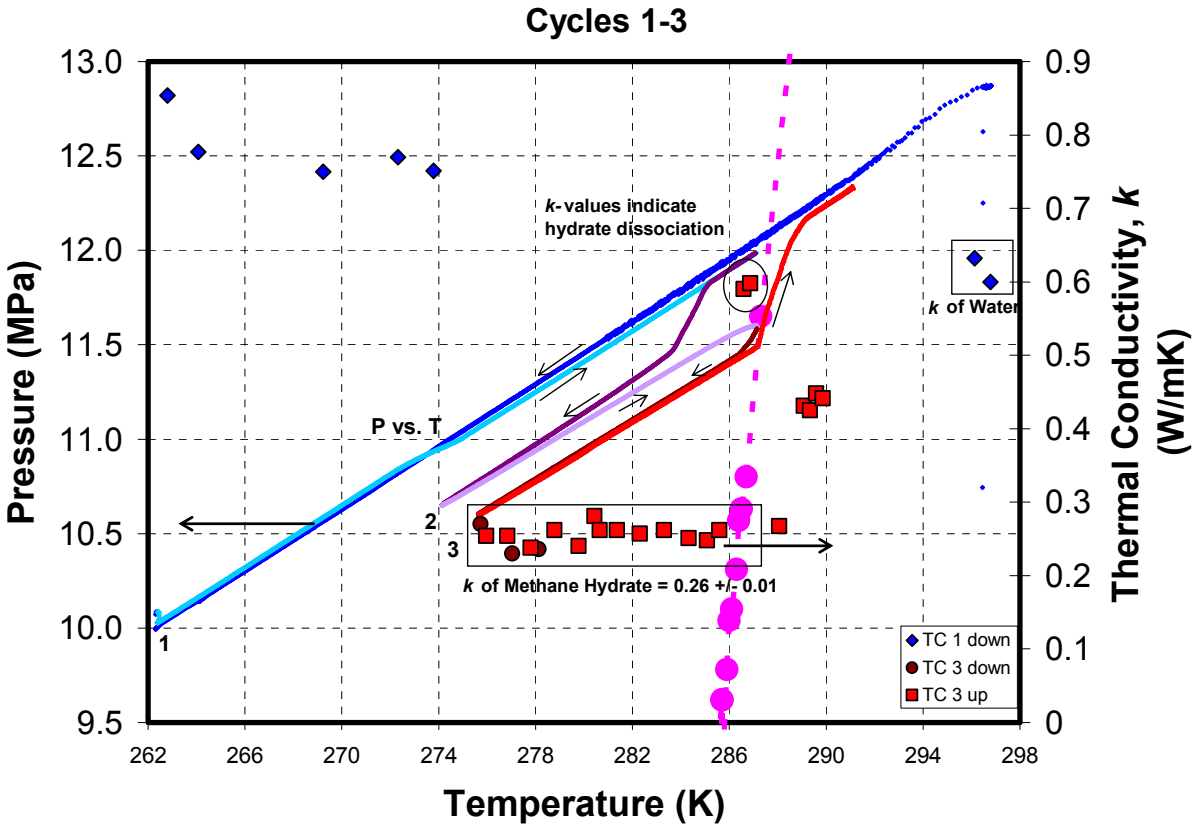

Figure 3-19: Experiment T20-017, Pressure and temperature data with corresponding thermal conductivity measurements.

much hydrate formed during the first cycle. Subsequent cycles, however, promoted more hydrate formation.

Thermal conductivity values were only taken during the first and third cycles. During the first cycle, hydrate formation was indicated by the pressure / temperature data. The thermal conductivity values obtained, however, were indicative of water and at lower temperatures a combination of water and ice. Hydrate formation would begin at the top of the water (or ice) and be limited by diffusion. It can be assumed from the high thermal conductivity values that the measurements taken during cycle 1 were of water (or ice and water) rather than hydrate.

Thermal property measurements were taken during cycle 3 down and up. The k values of cycle 3 down and up were almost the same. It appears from the pressure / temperature data and the nearly constant thermal conductivity values that all of the water was converted to hydrate. The thermal conductivity of cycle 3 up (before hydrate dissociation) in the temperature range of 276 K to 286 K was $k = 0.26 \pm 0.01$ W/mK. A straight line fit through the thermal conductivity values of cycle 3 up can be described by the following equation, where T is in Kelvin:

$$k = 0.0005T + 0.1058 \quad \textbf{(3-12)}$$

During cycle 3 up, the thermal conductivity corresponded with the pressure / temperature data. Before the pressure / temperature data indicated dissociation, the thermal conductivity rose suddenly. The thermal conductivity was 0.262 W/mK then suddenly rose to 0.59 W/mK right before the pressure rose, indicating the start of hydrate dissociation. The higher value of thermal conductivity seems indicative of water which has a higher thermal conductivity than hydrate. During dissociation the thermal conductivity was determined to be 0.267 W/mK and after complete dissociation the thermal conductivity was 0.44 W/mK.

The rise in the thermal conductivity, indicating the start of dissociation, could be from convection occurring due to the release of gas or from water present near the TPS. The thermal conductivity value during dissociation could be low for a number of reasons. During dissociation, methane is being released from the hydrate causing mixing. The thermal property measurements are of the sample surrounding the TPS. Gases near the TPS would cause the thermal conductivity to be low. After dissociation the thermal conductivity was lower than typical values of water.

After taking the cup out of the HVVC, much of the water was found outside the cup. The water most likely came out of the cup during dissociation, which has been observed in other experiments when the cup lid could not retain the sample. Approximately 0.4 g of water remained in the cup corresponding to a depth of about 2.03 mm (0.08 in.) which is about half of the probing depth. Because the water depth in the cup was lower than the probing depth, the thermal conductivity values were influenced by the gas above the sample. The low thermal conductivity values obtained for the water of post dissociation can be attributed to the low depth of the water as well as bubbles observed in the water on the TPS after the experiment.

3.4.8 Experiment T20-018: Thermal Property Measurements of Hydrates Formed from Water and Methane and Analysis with Raman

This experiment was done to verify the thermal property values obtained from the last experiment and also to attempt recovering the sample for further analysis.

0.895 g. of water, a depth of 4.369 mm (0.172 in.), was placed in the cup with the cup lid secured. At room temperature (299.09 K, 25.94 ^{o}C) the thermal conductivity of the water under air at atmospheric pressure was k = 0.53 W/mK. This thermal conductivity value is slightly lower than the literature values. Only one measurement of water at room temperature was taken in this experiment. Additionally, the depth of the water was close to the probing depth for a α-value of 3.32×10^{-7} m/s^2 determined at this temperature.

The temperature was lowered to 262.4 K (-10.8 ^{o}C, a set point of -12.0 ^{o}C) and held at this temperature for about 15 hours. The cell was pressurized with methane to bottle pressure then with the piston to about 12 MPa.

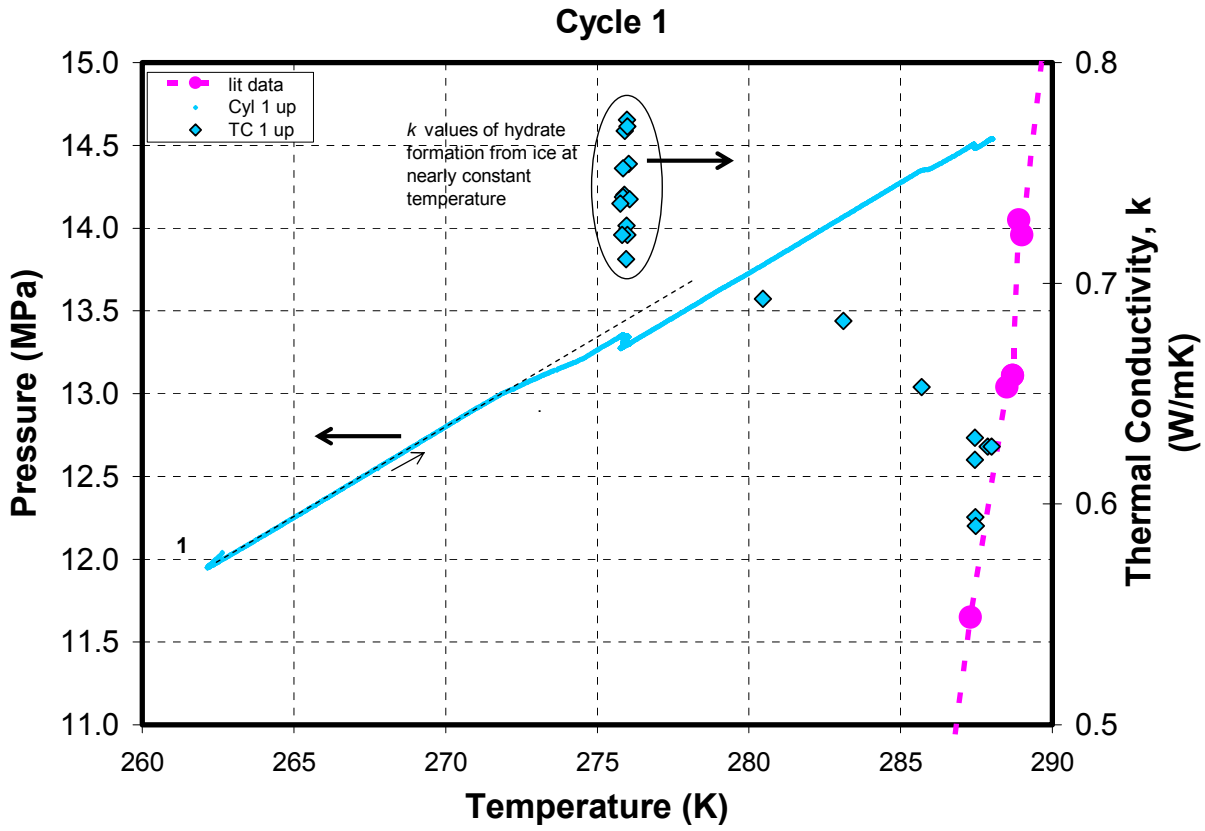

Figure 3-20: Experiment T20-018, Cycle 1 up.

The temperature was then increased at 1 K per hour to about 275.9 K (2.7 ^{o}C) and was held at this temperature for about 5 ½ days. At about 272 K (-1 ^{o}C), hydrate formation was observed in the pressure / temperature data. More hydrate formation was observed while the temperature was held at 275.9 K (2.7 ^{o}C). The thermal conductivity data corresponded with the trend in the pressure / temperature data. As the pressure continued to drop at almost constant temperature, indicating hydrate formation, the thermal conductivity became lower with time as well. When the pressure ceased to fall and the thermal conductivity values remained about constant, the temperature was raised to a set point of 287 K (14 ^{o}C), near but before the dissociation point. The hydrate was not dissociated but rather held at 287 K (14 ^{o}C) till the pressure remained constant. The temperature was increased by half a degree then another half a degree so that the pressure and temperature were very near the dissociation point. Figure 3-20 shows the pressure

and temperature data of the heating of cycle 1 and the corresponding thermal conductivity values versus temperature.

The temperature was lowered to 269.5 K (-3.7 ^{o}C) for cycle 2 then back to about 288 K (15 ^{o}C). No additional hydrate formation was observed in the pressure / temperature data, though the thermal conductivity was slightly lower than the first cycle thermal conductivity values (see Figure 3-21).

As the temperature was lowered to 262 K (-11 ^{o}C) in cycle 3, ice formation was observed in the pressure / temperature data with a rise in pressure as the water expanded into its solid state. The values of thermal conductivity, as taken during the cooling of cycle 3, were significant in two ways. The thermal conductivity indicated the formation of ice. The fact that the thermal conductivity value was close to ice indicates that water was near the sensor and not hydrate. The thermal conductivity right before ice formation was 0.708 W/mK and was 2.41 W/mK after ice formation was indicated in the pressure / temperature data.

The temperature was increased to a few degrees above the melting point of ice, 276 K, to

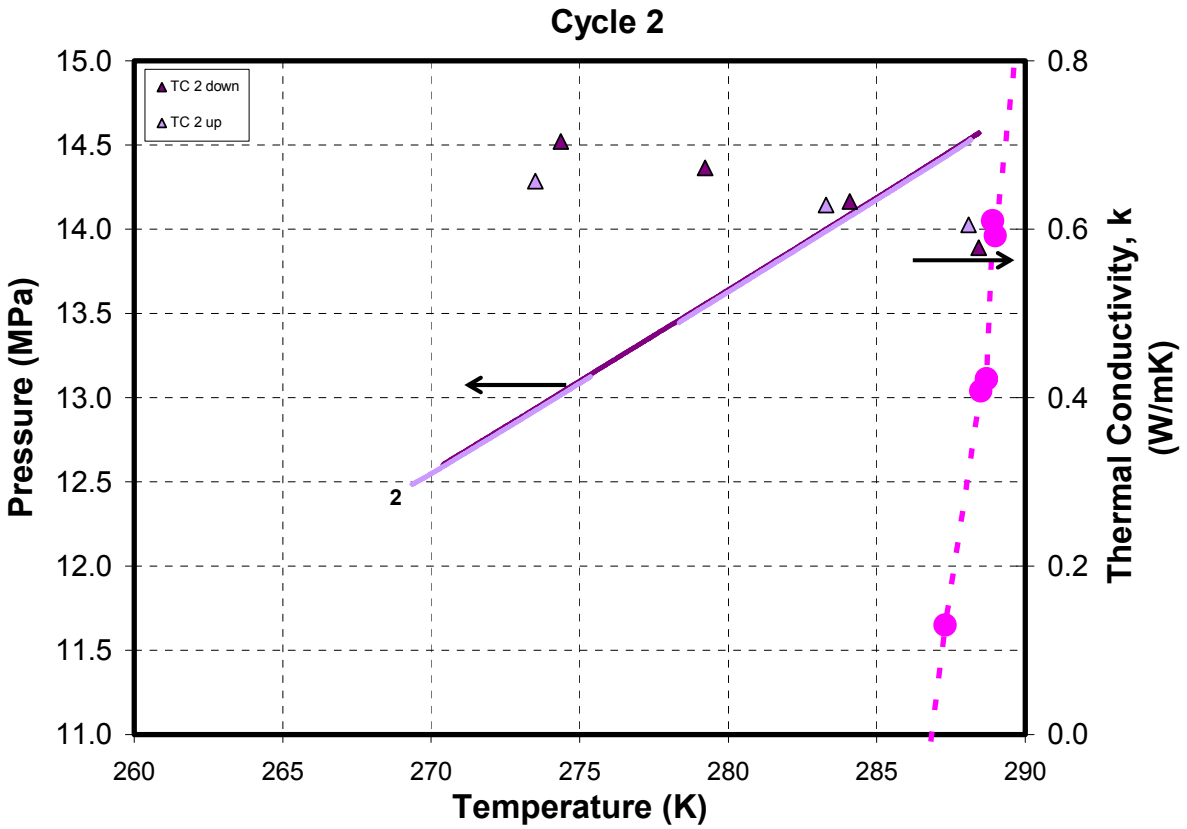

Figure 3-21: Experiment T20-018, Cycle 2.

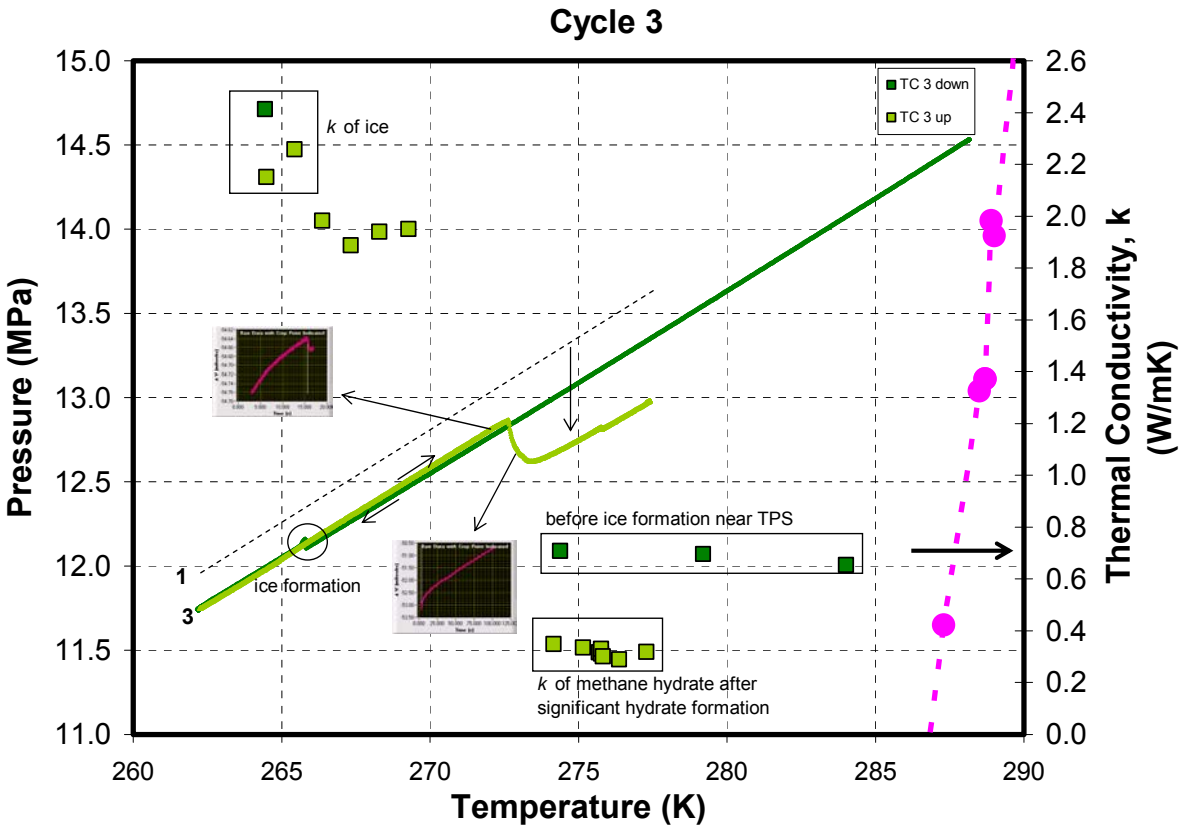

Figure 3-22: Experiment T20-018, Cycle 3.

form hydrate from the unconverted water. The temperature was then increased by 2 K. Around 272.7 K, more hydrate formed with an almost 0.2 MPa drop in pressure. Subsequent cooling, heating, and cooling (cycle 4 down, cycle 4 up, and cycle 5 down, respectively) with no apparent changes in pressure, indicated that all the water was converted to hydrate. The thermal conductivity corresponded with the indications of the pressure / temperature data. The thermal conductivity values, right before the drop in pressure of cycle 3 up, were between 1.87 and 1.98 W/mK. After hydrate formation was confirmed by the pressure / temperature data, the thermal conductivity dropped to 0.348 W/mK.

Thermal conductivity measurements taken right before and during hydrate formation were not possible to analyze. Right before the 0.2 MPa pressure drop, hydrate formation was indicated with the thermal conductivity data (voltage drop data). A slight drop in the pressure was indicated in the pressure / temperature trace about where hydrate formation occurred in cycle 2 up at about 272 K (-1 ^{o}C). The thermal conductivity data concurs in that the voltage drop

data collected across the Wheatstone bridge did not show a smooth rise in ΔV with time (see Figure 3-22) when hydrate formation was starting. During hydrate formation, the ΔV data, again, did not show a smooth rise with time. The voltage data indicated activity inside the sample cup. In a sample where heat transfer is accomplished by conduction alone and without convection occurring, the plot of ΔV versus time rises smoothly and will eventually become almost level as the temperature rise becomes steady (refer to Figure 3-2).

During cycles 4 and 5, the thermal conductivity remained almost constant (see Figure 3-23). The pressure / temperature data during these cycles did not indicate any additional hydrate formation. The thermal conductivity values all decreased with increasing temperature. The behavior of the data can be described by the following equation for the temperature range of 264 K to 277 K (T is in Kelvin):

$$k = -0.0034T + 1.2324 \qquad \textbf{(3-13)}$$

The pressure data for all of the cycles with the corresponding thermal conductivity values versus temperature are included in Figure 3-24. With subsequent cycles, additional hydrate formed, indicated by a pressure drop. The thermal conductivity determined for cycles 1, 2, and 3 are near that of water and can be seen to drop with subsequent cycles. It was not until the heating of cycle 3 that significant hydrate formation was observed. The thermal conductivity values correspond well with the pressure / temperature data.

The thermal diffusivity was determined simultaneously with the thermal conductivity. The thermal diffusivity of water at room temperature was determined to be $\alpha = 3.32 \times 10^{-7}$ m^2/s. The diffusivity values dropped as more and more hydrate formed in the cup with subsequent cycles. The thermal diffusivity of ice was near that of the values obtained for cycles 1 and 2, which was determined to be water. The thermal diffusivity of ice was determined to be $\alpha = 1.39 \times 10^{-7}$ m^2/s at 264.4 K. During cycle 3, when significant hydrate formation was observed from the pressure / temperature data, the thermal diffusivity right before formation was $\alpha = 0.51 \times 10^{-7}$ m^2/s and rose to 2.25×10^{-7} m^2/s after formation. The thermal diffusivity for cycles 4 down, 4 up, and 5 down was determined to be $\alpha = (2.59 \pm 0.16) \times 10^{-7}$ m^2/s.

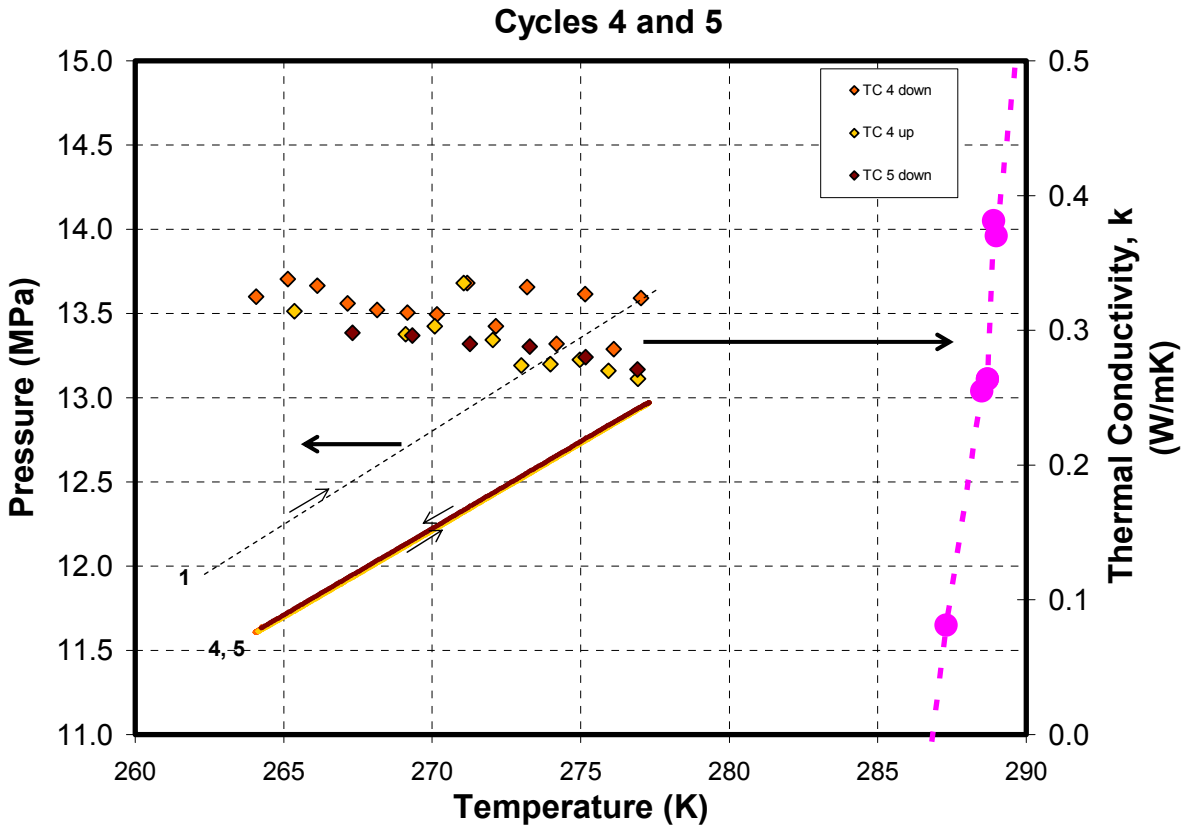

Figure 3-23: Experiment T20-018, Cycles 4 and 5.

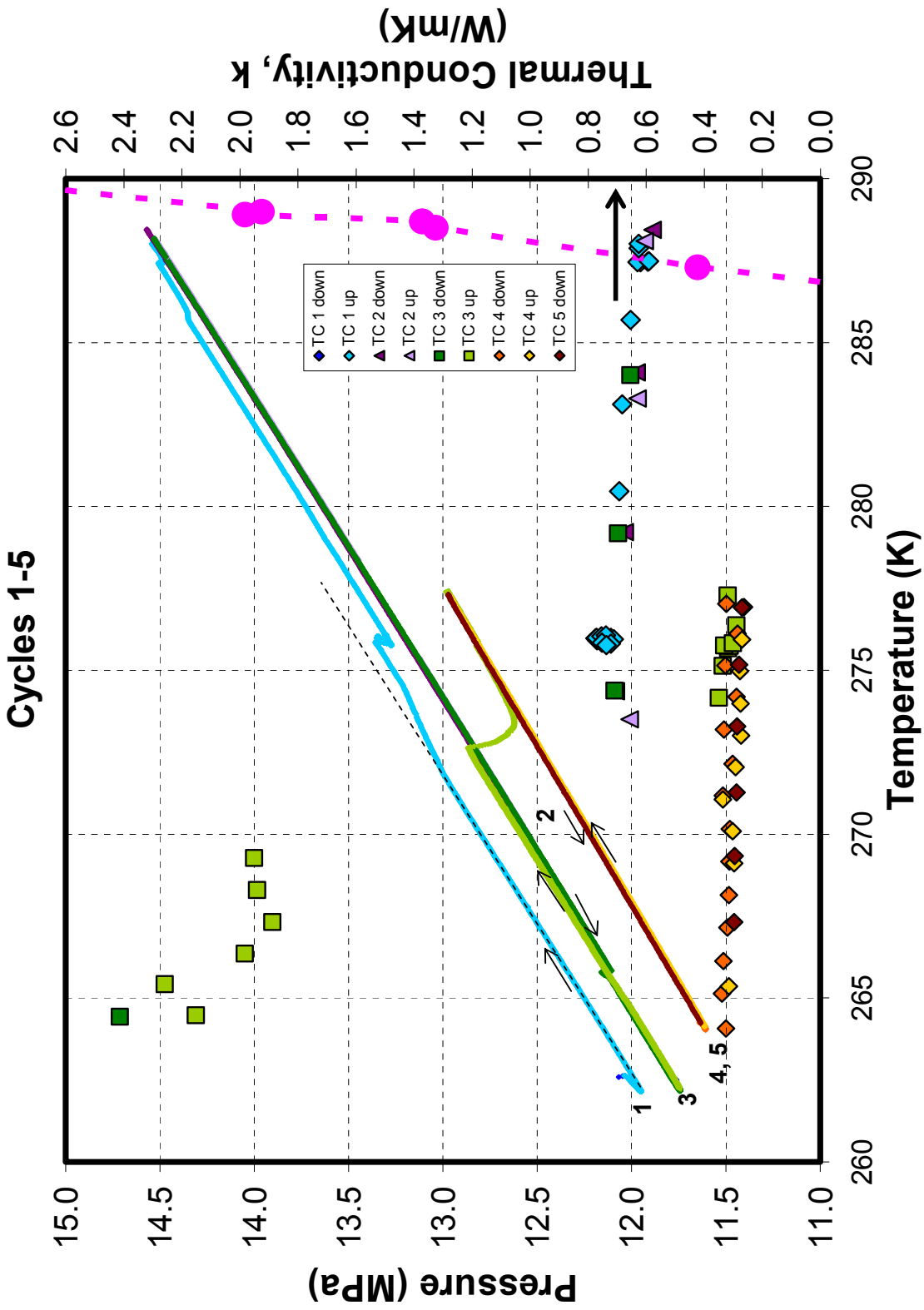

Figure 3-24: Experiment T20-018, cycles 1 up through 5 down with thermal conductivity values.

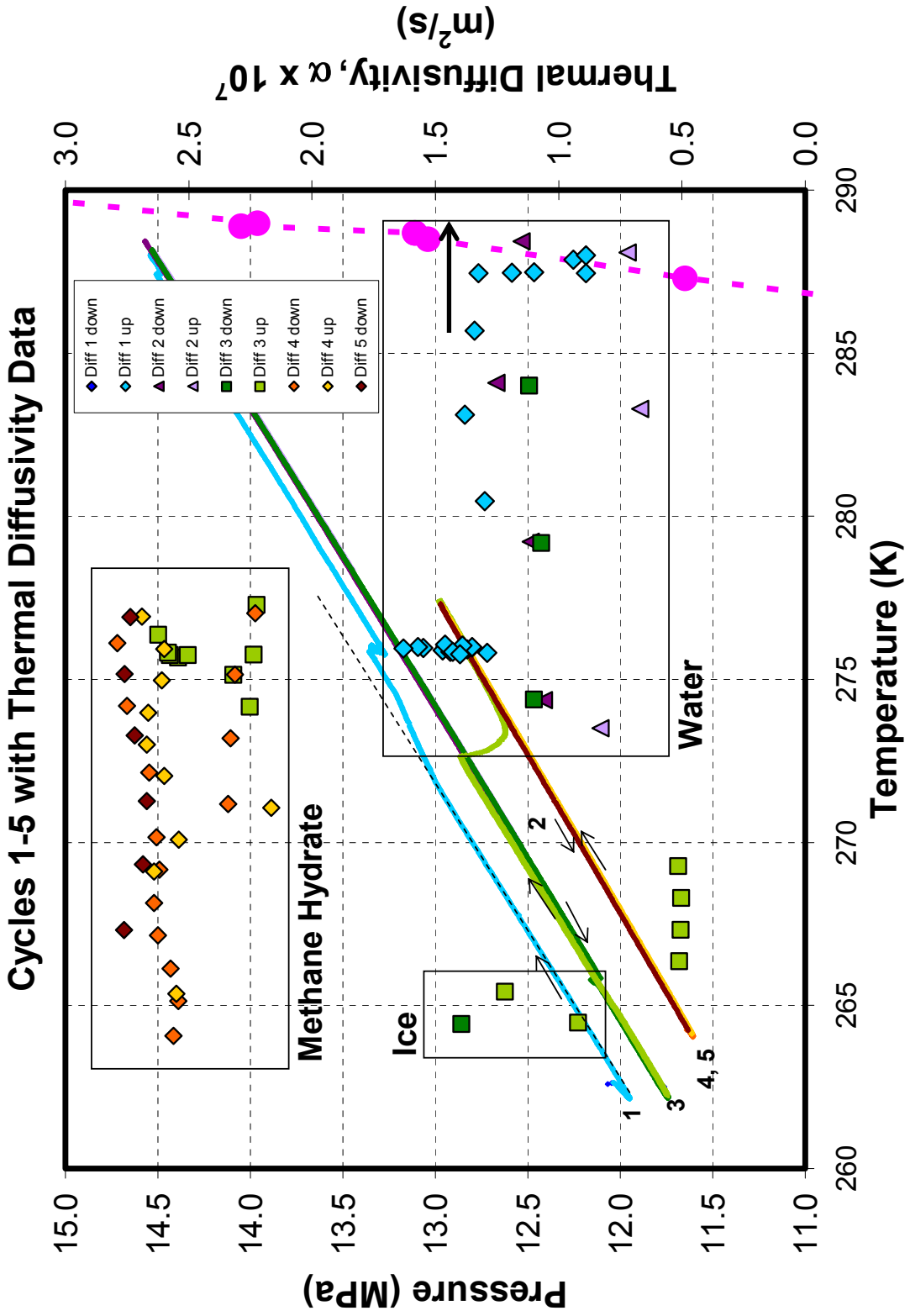

Figure 3-25: Experiment T20-018, Cycles 1 up through 5 down with thermal diffusivity values.

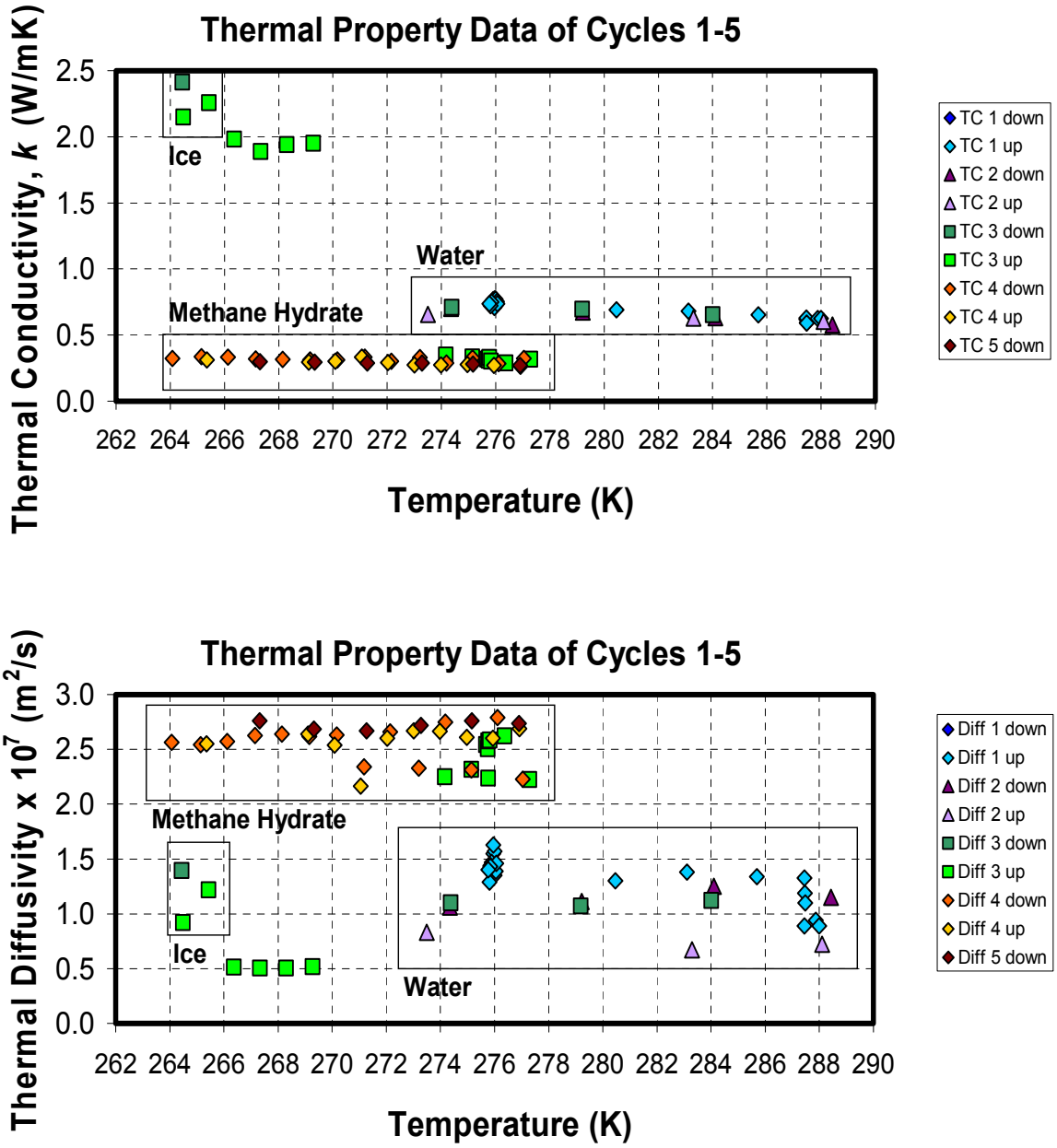

Figure 3-26: Experiment T20-018, Thermal Conductivity and Thermal Diffusivity Data.

The temperature was lowered to a set point of 261 K (-12 ^{o}C) so that the sample could be recovered. The cup bottom was removed to recover the sample. The cup sleeve, containing the sample, was placed in liquid nitrogen so that it could be inspected and further analyzed. After taking the sample out of the liquid nitrogen, it was difficult to obtain a clear picture of the hydrate sample because of the evaporating liquid nitrogen. The picture shown in Figure 3-27 is a view of the hydrate that was in contact with the TPS element. The cup bottom, containing the TPS element, was removed to view the portion of the sample in contact with the TPS. The picture shows pores in the unconsolidated hydrate sample, which appeared almost snow-like. Because the sample was unconsolidated, any voids present in the sample would affect the thermal conductivity measurements.

Figure 3-27: Hydrate in cup sleeve. The cup bottom was removed to view the hydrate sample and pictured above is the hydrate near the TPS.

Figure 3-28 is a picture of the cup bottom after being placed in liquid nitrogen and exposure to the atmosphere. The TPS is covered with a portion of the hydrate sample as well as some frost formed from condensing water. Despite the fact that the sample was out of the liquid nitrogen for considerable amounts of time and at atmospheric pressure, the entire sample remained amazingly intact, though some water condensed and froze on the sample while taking pictures. The frost that formed on the hydrate sample and cup bottom can be seen in Figure 3-28.

Raman spectroscopy was performed on the recovered sample in the sleeve (see Figure 3-27). The sample was contained in the sleeve of the cup during testing. The Raman spectrum indicated a relatively pure sample of hydrate [1]. The results can be seen in Figure 3-29.

Figure 3-28: Cup bottom shown with hydrate stuck on the TPS element.

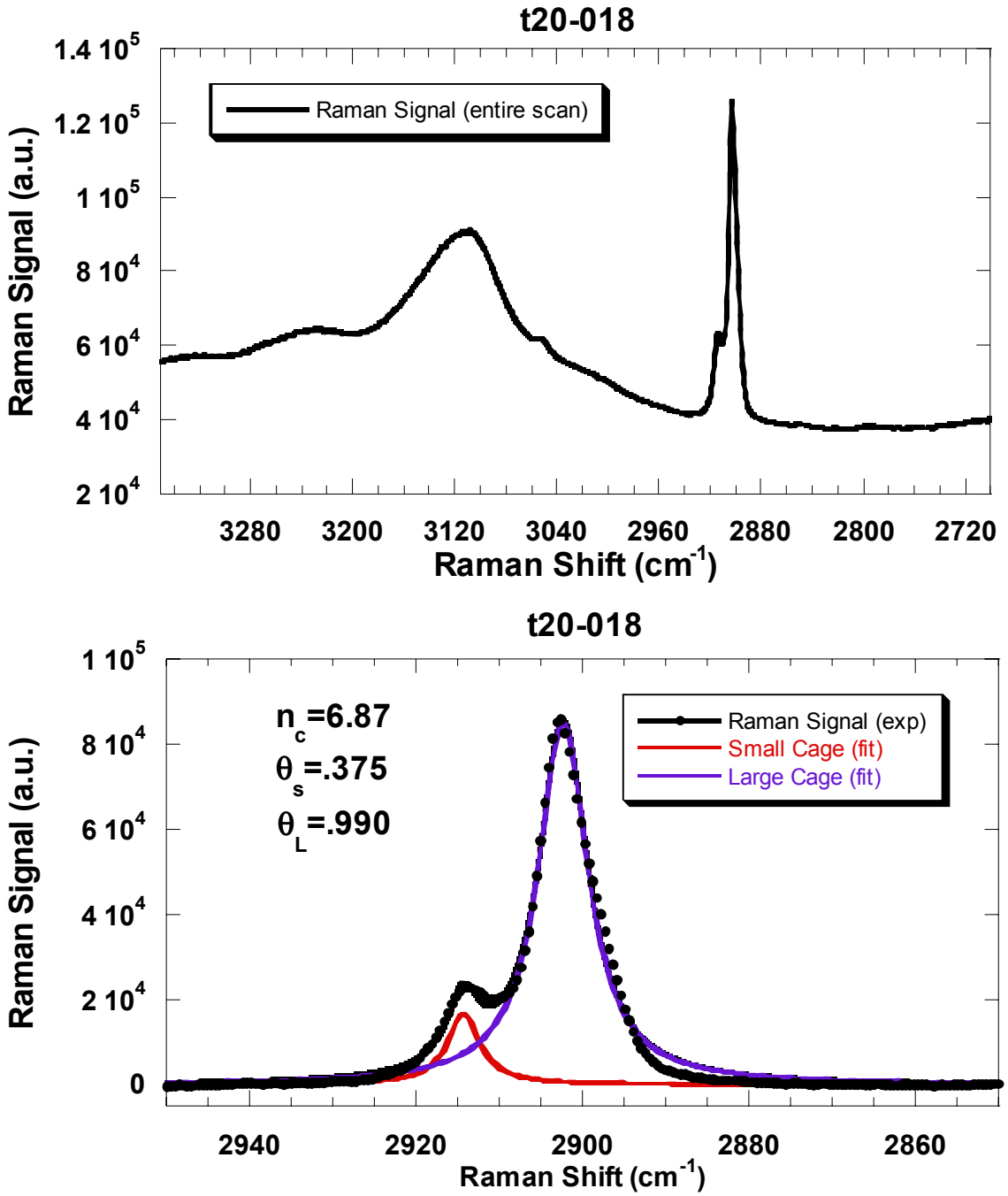

Large Cage:
Resonance Energy = 2902.4 cm^{-1}
FWHM = 7.28 cm^{-1}

Small Cage
Resonance Energy = 2914.2 cm^{-1}
FWHM = 4.68 cm^{-1}

Figure 3-29: Raman Spectroscopy Results.

After performing Raman spectroscopy on the sample, the sample was pushed out of the sleeve. The hydrate was dissociated at room temperature and atmospheric pressure. Figure 3-30 shows the water and gas of the dissociated hydrate that was stuck to the TPS element (see Figure 3-28). The bubbles usually found trapped in the water after dissociation are also seen in the picture.

Figure 3-30: The dissociated hydrate on the cup bottom.

4.0 DISCUSSION

The first few experiments performed enabled experimental improvements. The experiments where visual observations were made gave useful insight into redesigning the cup. After the cup was redesigned and the data collection and analysis was automated, a few more experiments prompted changes in the experimental procedure so that the final two experiments, T20-017 and T20-018 were successful in obtaining thermal property data of methane hydrates.

In experiment T20-017 the thermal conductivity and thermal diffusivity were determined for a methane hydrate sample formed in the new TPS cup. Verification of the sample

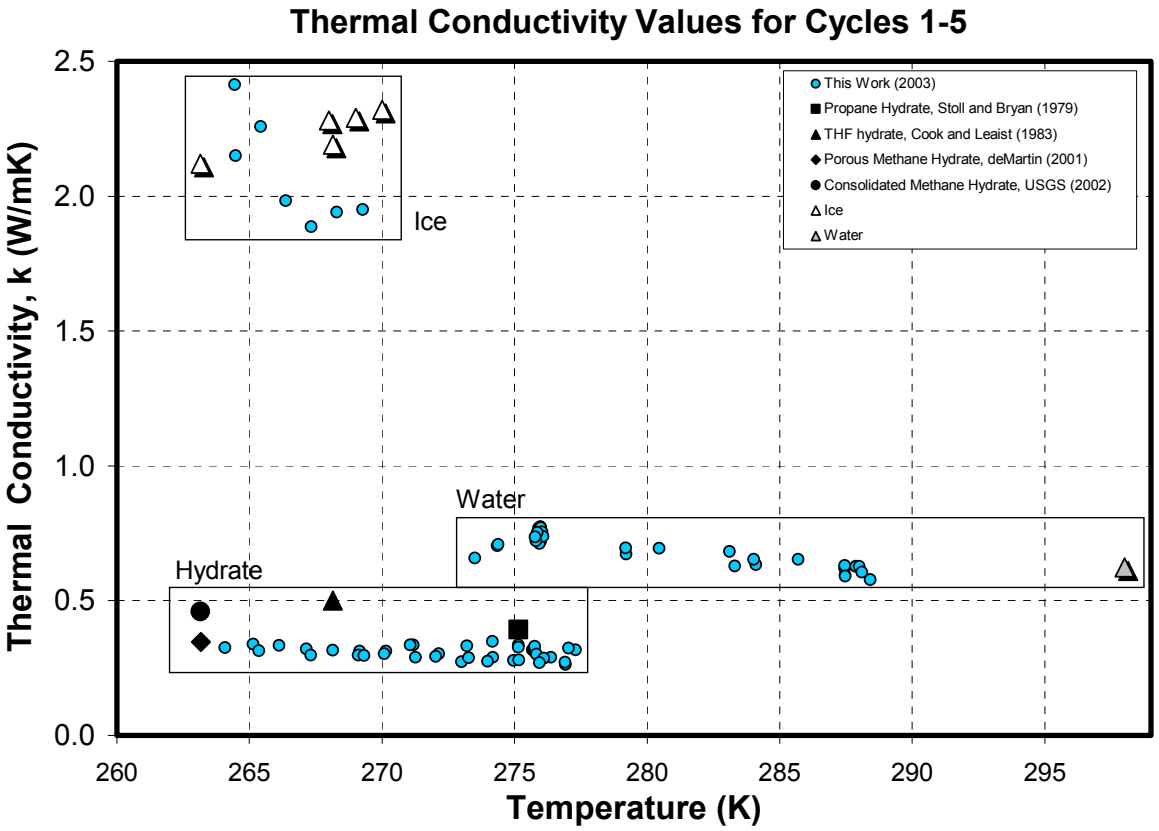

Figure 4-1: Experiment T20-018, Thermal conductivity values from this work with literature values.

composition was not done since the sample was dissociated and part of the water was lost during dissociation because of the absence of the cup lid during this experiment. The thermal property values were constant for the cooling and heating of the third (last) cycle, which seems to indicate that all of the water had converted to hydrate.

The thermal conductivity values obtained from experiment T20-018 during the fourth and fifth cycles, after complete conversion of the water to hydrate was confirmed, were low compared to other literature values. Most of the literature values shown in Figure 4-1 were of consolidated hydrate samples except for the values obtained by deMartin [15].

The thermal conductivity range obtained from experiment T20-018 of 0.264 W/mK to 0.338 W/mK corresponds to a void fraction of about 0.10 to about 0.25. Figure 4-2 shows the effective thermal conductivity of an unconsolidated methane hydrate sample [26]. Assuming a thermal conductivity value for a consolidated hydrate sample and the thermal conductivity of methane, the effective thermal conductivity at different void fractions is given by different models [27]. It seems reasonable that, after viewing the post-experiment pictures, the void

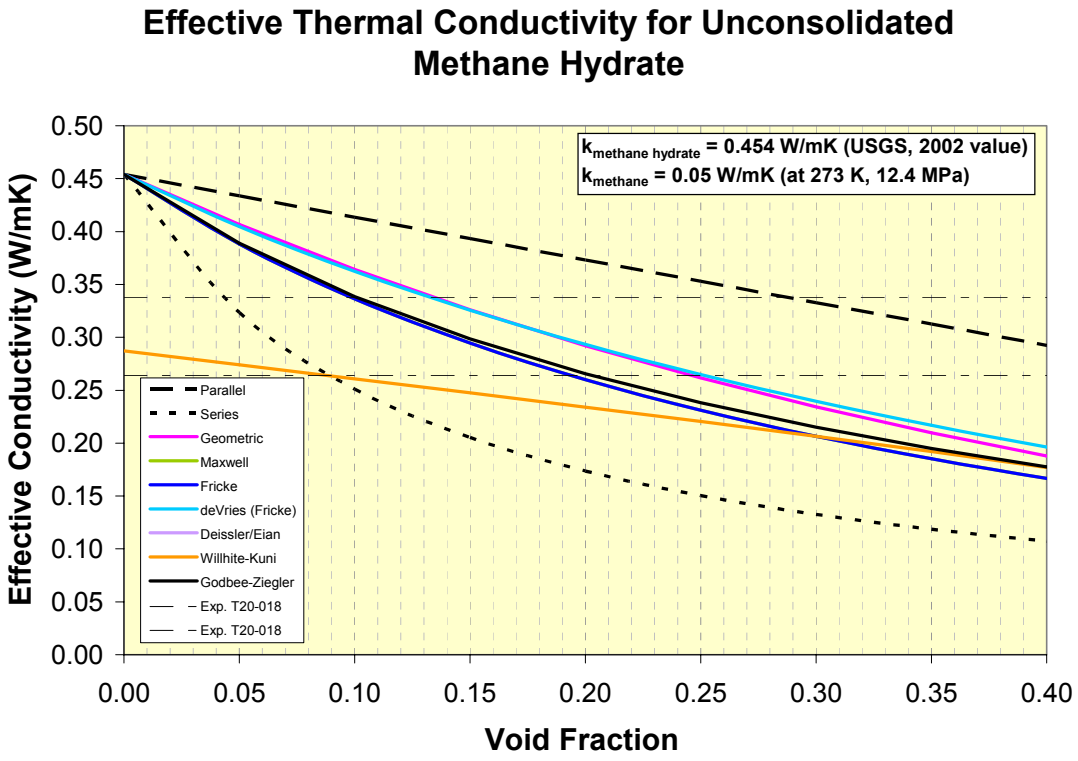

Figure 4-2: Models depicting the effective thermal conductivity for unconsolidated methane hydrate [26, 27].

fraction in the sample of experiment T20-018 is between 0.10 and 0.25. The range of thermal conductivity values obtained for experiment T20-018 are indicated in Figure 4-2 by two horizontal lines. The only other reported thermal conductivity values on a porous methane hydrate sample were by deMartin [15]. The values deMartin reports were for pure methane hydrate samples with porosities between 28% and 33%, determined by knowing the hydrate volume and the volume of the sample vessel.

The thermal conductivity values obtained from Experiment T20-018 decrease with increasing temperature. Ross and Anderson report an increase in the thermal conductivity with increasing temperature for THF hydrate [14]. USGS reports decreasing thermal conductivity values with temperature [10]. Since few measurements exist, it has not been concluded what the dependence of the thermal conductivity on temperature is for methane hydrates.

Figure 4-3 displays the thermal conductivity values obtained for experiments T20-017 and T20-018. The values shown are of the last cycles in both experiments where the thermal

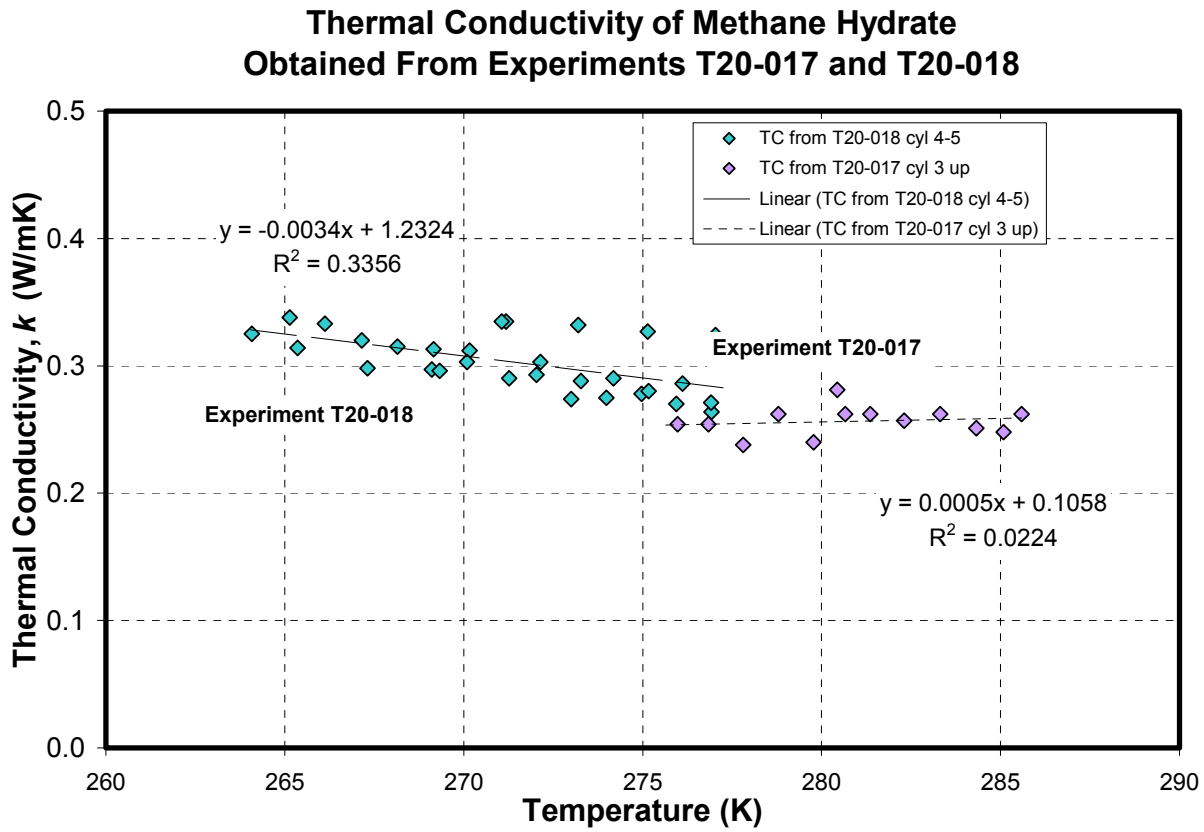

Figure 4-3: Thermal Conductivity of methane hydrate from experiments T20-017 and T20-018.

conductivity values remained constant for subsequent cycles and the pressure / temperature data did not indicate additional hydrate formation.

Only one other source reporting thermal diffusivity values was found. The thermal diffusivity values reported by deMartin are higher than the thermal diffusivity values reported here [15]. The values reported in deMartin's thesis were of compressed, pre-stressed samples. In his work he found that thermal diffusivity rose with increasing confining pressure. Since increasing the confining pressure would essentially decrease pores in the hydrate sample, it seems reasonable that since the sample in this work is unconsolidated that the difference in the thermal diffusivities can be attributed to the difference in porosity.

Figure 4-4 displays the thermal diffusivity values obtained from this work along with the values reported by deMartin. Because of experimental problems in deMartin's work, the other values he reports are at temperatures well below where measurements were taken in this work. One of his samples was also found to have ice in it and is also displayed in the figure as a straight line since his thermal diffusivity was described in terms of a straight line.

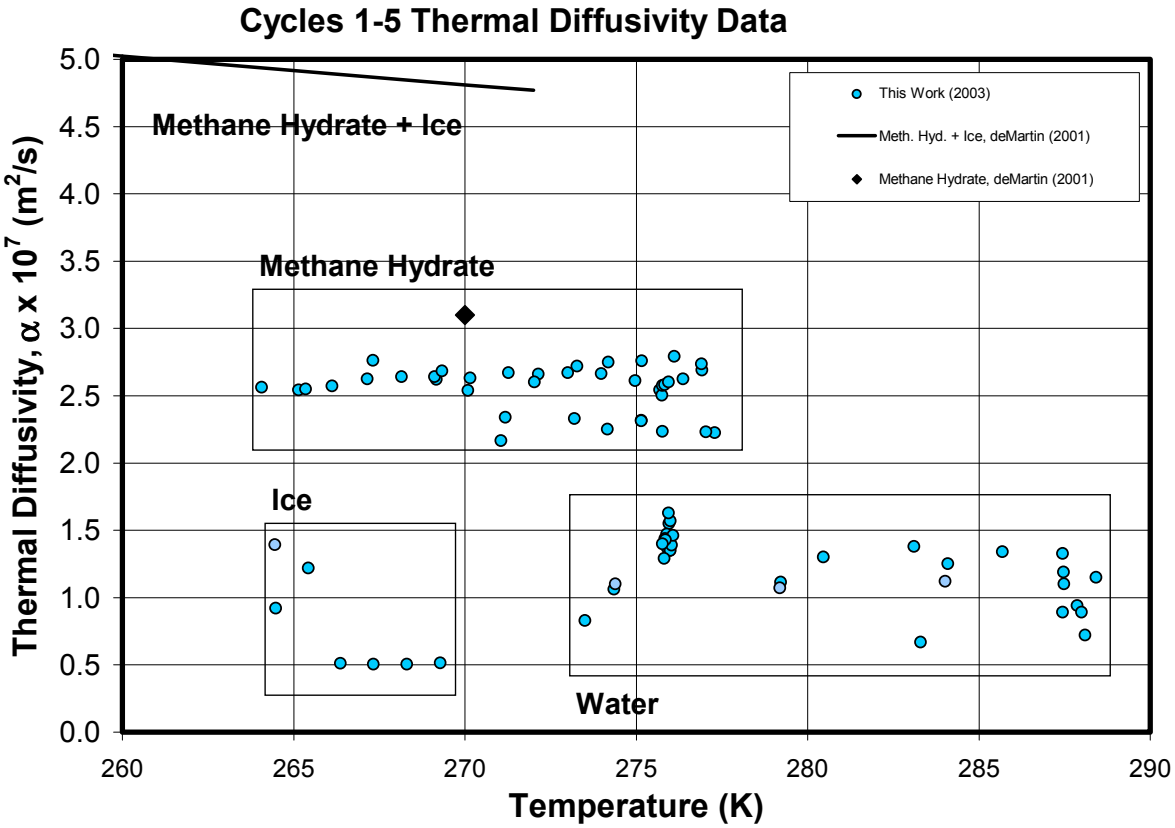

Figure 4-4: Experiment T20-018, Thermal diffusivity data with literature data.

5.0 CONCLUSIONS

The thermal conductivity and thermal diffusivity have been determined for an unconsolidated methane hydrate sample measured in the high-pressure vessel used to form the hydrate. Through experimental improvements, an automated, quick method has been developed to determine the thermal conductivity and thermal diffusivity of a sample of methane hydrate with a single measurement.

The cup designed to contain the sample around the TPS has proven to retain the sample during experiments. The interface between the sample and the TPS could be inspected by removing the cup bottom. The sample was also recovered during this experiment and additional Raman spectroscopy analysis was performed on the methane hydrate sample.

The experimental setup has been calibrated with substances of well investigated thermal properties. The thermal conductivity and thermal diffusivity of glycerol, water, and ice have been measured and compared with existing data of these substances.

In two experiments, the thermal properties have been determined for methane hydrates, though numerous insightful experiments were performed prior to these two successes. It must be noted that during the experiments performed, many thermal property measurements were possible throughout the process. The values for thermal conductivity and thermal diffusivity were validated through many measurements of the sample and the results are reproducible.

In all thermal property measurements, reported elsewhere and herein, the thermal conductivity of methane hydrate was found to be strikingly lower than ice by at least five times and lower than water by almost one and a half times, despite its structural similarities to ice. The thermal conductivity of methane hydrate in this work was determined to be 0.28 ± 0.01 W/mK for a temperature range of 276 K to 286 K in the pressure range 10.6 MPa to 11.4 MPa from experiment T20-017. In a similar experiment, experiment T20-018, where the sample was recovered and analyzed with Raman spectroscopy, the thermal conductivity decreased slightly with increasing temperature. The thermal conductivity for a temperature range of 264 K to 277

K and pressure range of 11.6 MPa to 13.0 MPa, respectively, can be described by $k = [-0.0034\ T + 1.2324]$ W/mK, where T is in Kelvin. The average of the thermal conductivity values within this range of temperatures and pressures is $k = 0.30 \pm 0.02$ W/mK. The thermal conductivity values obtained from this investigation are lower than other reported values but seem reasonable if the porosity of our sample was between 10 % and 25 %, which seem valid given the visual observations of the sample recovered from the cup.

The thermal diffusivity of methane hydrates determined in this work from experiment T20-018 was $\alpha = [2.59 \pm 0.16] \times 10^{-7}$ m^2/s. It can also be described by $\alpha = 0.0005\ T + 2.4424$ m^2/s where T is in Kelvin. The aforementioned thermal diffusivity values were within the temperature range of 264 K to 277 K and pressure range of 11.6 MPa to 13.0 MPa, respectively.

Few measurements of the thermal conductivity of methane hydrates and even fewer measurements of the thermal diffusivity have been reported. The method developed in this work has proven successful, and reproducible so that many future experiments can be performed. Measurements are made within the synthesis vessel, which has made other reported values questionable. Because this measurement technique is fast, without altering the sample, and has now been automated, many measurements on the same sample are possible.

6.0 FUTURE WORK

From the insight of the experiments described in this report, many experiments remain to expand the knowledge of methane hydrates. Some objectives for future experiments and investigations include: measurements on compacted samples, measurements of methane hydrate and sediment mixtures of varying hydrate composition, utilizing gas mixtures containing other components of natural gas, sample characterization, the possible use of surfactants, and modeling to compliment experimental results.

As was seen with comparison to other literature values, the porosity of our methane hydrate affected the thermal conductivity making it lower than other reported values. To obtain more useful thermal property data, the sample will be compressed. Thermal property measurements will be made on the sample both pre and post-compression. In modeling of multi-component systems where gas, hydrate, liquid or solid water can exist, it is necessary to have thermal property data of consolidated hydrate.

Thermal conductivity values have been reported elsewhere for methane hydrates in sediment mixtures made from water / sand mixtures and ice / sand mixtures. This work has yet to complete thermal property measurements of hydrate / sediment measurements. Given the success of the current experimental setup thus far, measurements of hydrate / sediment mixtures can and will be performed in the very near future. Not only will the individual constituents of the mixtures need characterization (e.g. the composition of the sand, the size of the sand particles, and the voids created by the sand), but the mixture both pre and post experiment will need characterization. Because sample characterization is so important in determining the thermal properties, the cup designed in this work was a large focus in experimental improvement to allow for sample recovery.

Because these experiments are performed without any mixing, hydrate formation is limited by diffusion. Since the TPS element, measuring the thermal properties, is located at the bottom of the cup and methane is introduced to the top of the sample, it takes successive temperature

ramps to ensure that methane hydrate is formed down to the TPS. The use of surfactants could promote uniform hydrate formation and may even promote the hydrate to form on or near the TPS first.

No modeling has been reported in this work, which will be a very near future focus to compliment the experimental work. Modeling will serve to enhance the measurements and may lend insight for experimental improvements or directions.

APPENDIX A

DATA ACQUISITION AND ANALYSIS

A.1 NATIONAL INSTRUMENTS HARDWARE

The diagrams shown in this appendix are of National Instrument components used to automate the thermal property measurements. These components replaced a Keithley multimeter and manual switch of the previous experimental setup.

An electromechanical relay switch, SCXI-1161, shown in Figure 0-1 is part of the Wheatstone bridge circuit and allows the current to flow through the Wheatstone bridge when prompted by the LabVIEW data acquisition program, allowing the experiments to be automated. The SCXI-1161 has eight independent, non-latching relays each with a normally closed (NC), normally open (NO), and common (COM) terminal. The relay can be controlled with National Instruments LabVIEW software.

The temperature sensor terminal block shown in Figure 0-3 allows data collection of the voltage difference across the Wheatstone bridge, the voltage across the sensor, and the voltage across the reference resistor during the transient measurement. Each parameter to be measured is connected to a different channel on the temperature sensor terminal block and data collection is controlled by LabVIEW. The temperature sensor is plugged into a SCXI-1120 signal conditioning module. The SCXI-1120 diagram is shown in Figure 0-2. The SCXI-1120 is an 8-channel isolated analog input module. The amplifiers can be configured using jumpers for input ranges from ± 2.5 mV to ± 5 mV.

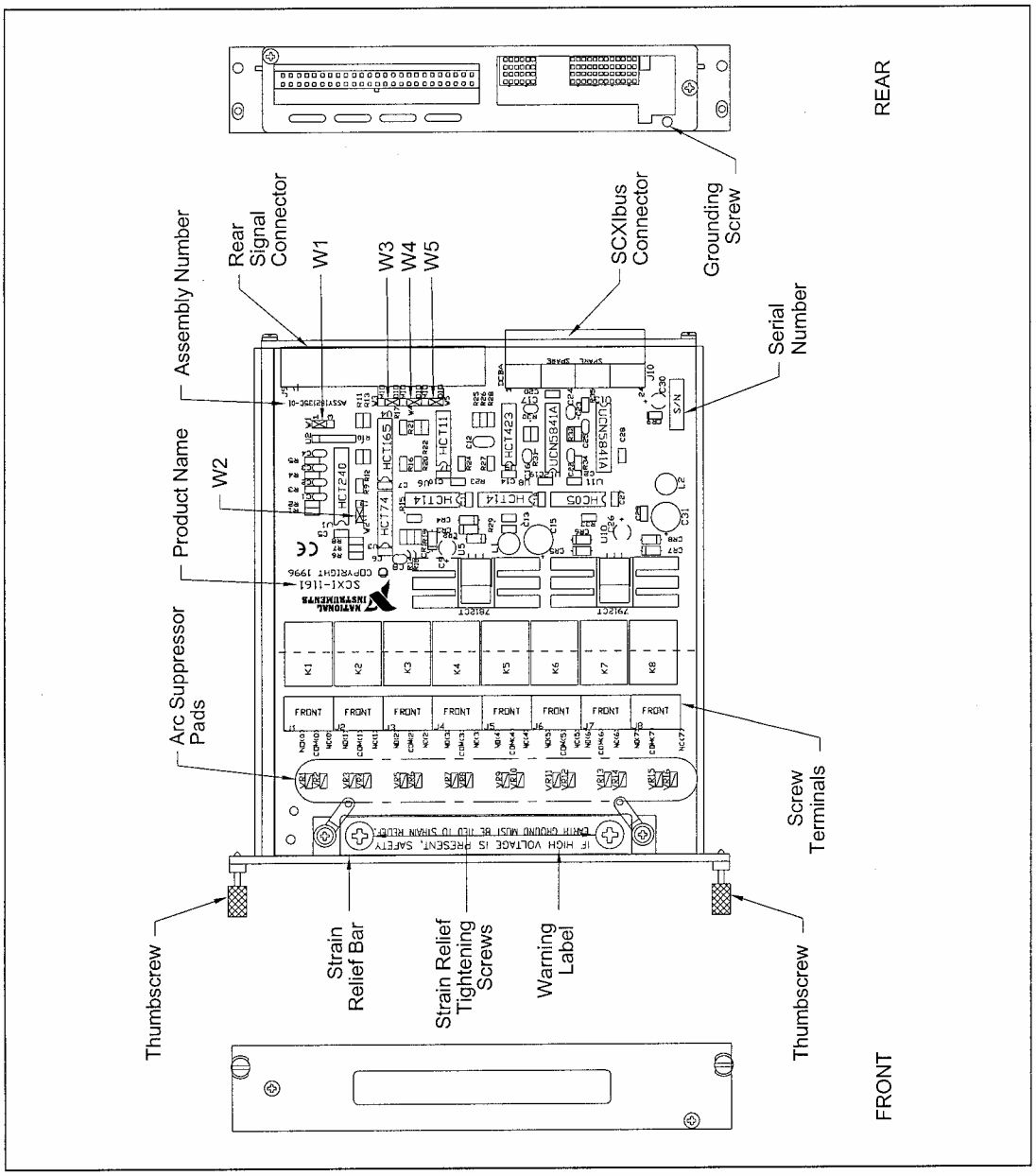

Figure 2-1. SCXI-1161 General Parts Locator Diagram

Figure A-1: Electromechanical relay switch used to initiate thermal property measurements.

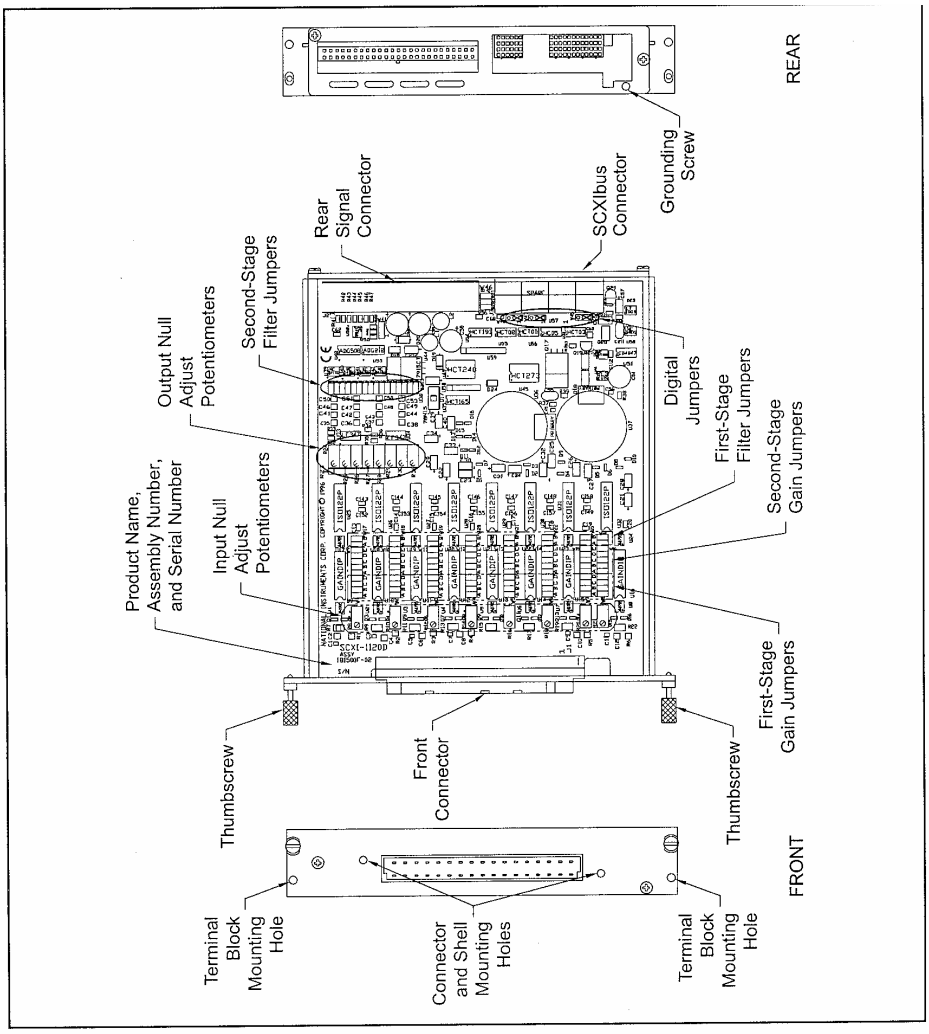

Figure 2-1. SCXI-1120/D Parts Locator Diagram

Figure A-2: 8-Channel isolation amplifier, 10 kHz bandwidth.

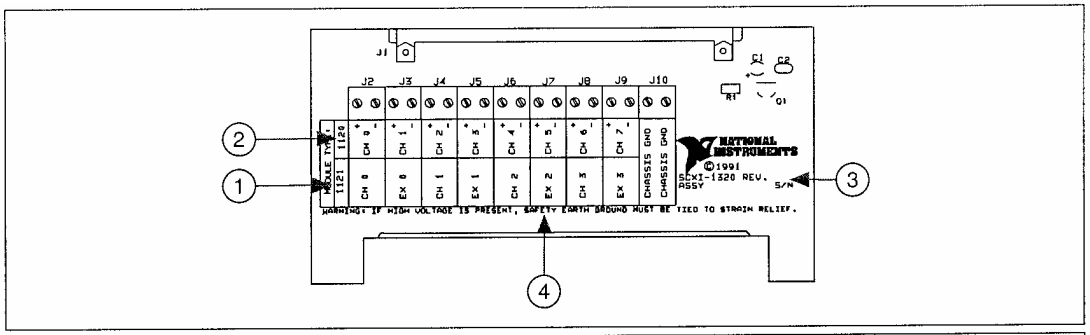

1 Channel Labeling for the SCXI-1121	3 Product Name, Assembly Number, Revision Letter, and Serial Number
2 Channel Labeling for the SCXI-1120, SCXI-1120D, SCXI-1125, and SCXI-1126	4 Warning Label

Figure 1. SCXI-1320 Signal Connections

Figure A-3: Temperature sensor terminal block.

A.2 DATA ANALYSIS PROGRAM (IN LabVIEW)

The data collected using the National Instruments components is analyzed using a program written in LabVIEW, a general-purpose programming system. LabVIEW is based on G programming, a graphical data flow programming language. The programs written in LabVIEW are referred to as virtual instruments (VIs) due to their appearance and operation which imitate actual instruments. LabVIEW offers a means for data acquisition, instrument control, data processing, and data storage. LabVIEW has an interactive user interface where inputs can be made and outputs displayed. This interface can simulate the panel of an actual instrument and is appropriately called the front panel. The actual code of the program is viewed and worked on in another window and the code is displayed in the form of a block diagram which is constructed in G.

The front panel of the data analysis program is shown in Figure 0-4. The block diagram of the data analysis program is shown in Figure 0-5 with the code displayed as sub-VIs and wires connecting the sub-VIs. The data analysis program is made up of many sub-routines referred to as sub-VIs. The calling hierarchy of these sub-VIs is shown in Figure 0-6. What follows is the documentation of the data analysis program including the connector pane, showing the sub-VI inputs and outputs, and the block diagram of each sub-VI that makes up the data analysis program. Any hidden cases (i.e. true or false cases) are shown as separate blocks following the block diagram. The sub-VI documentation is listed in the hierarchical order of the data analysis program, shown in Figure 0-6. The sub-VIs shown in the figure that have not been included in the documentation are the build-in sub-VIs included with the LabVIEW software package.

Data Analysis

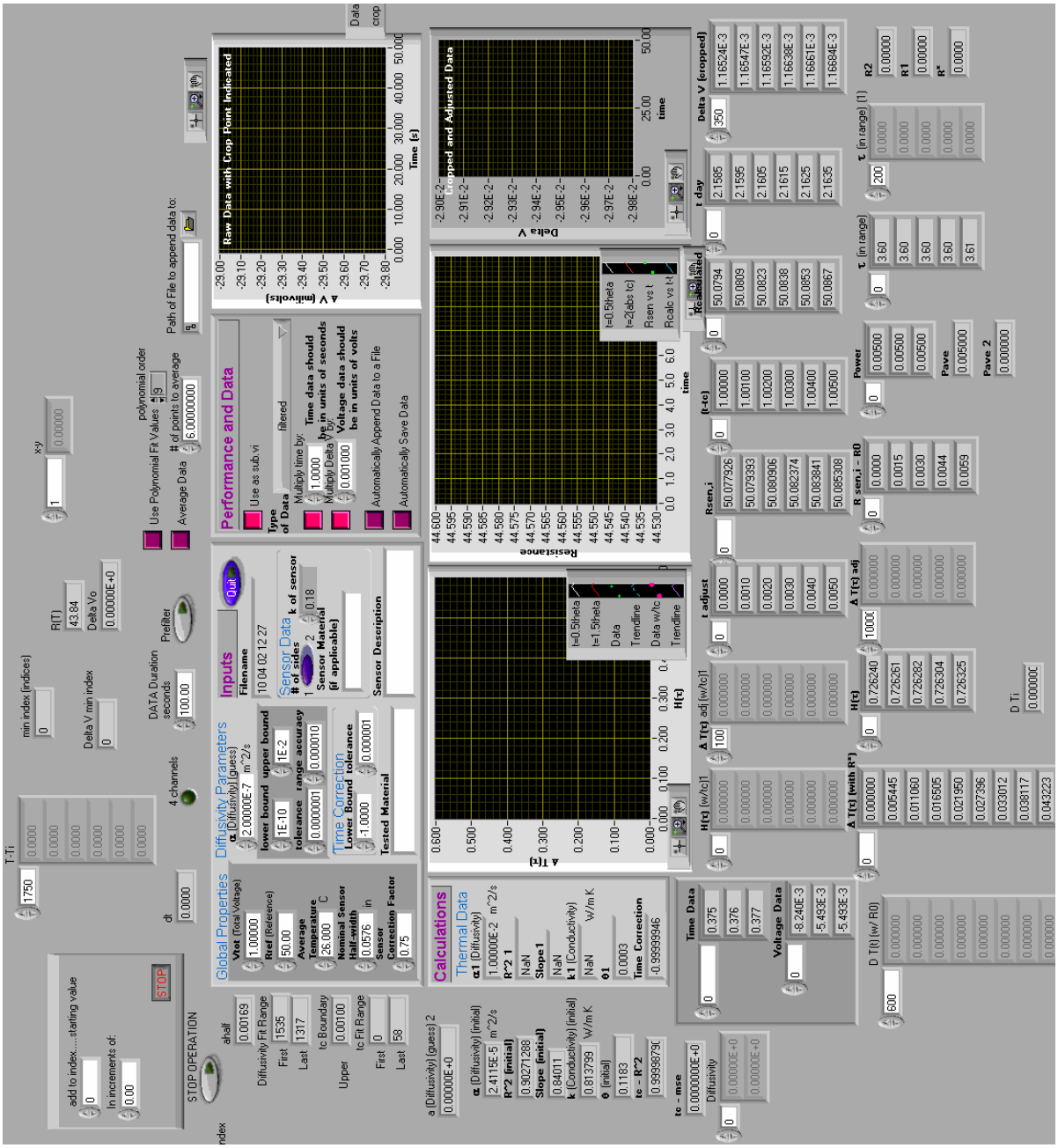

Figure A-4: Front Panel of the LabVIEW Data Analysis Program.

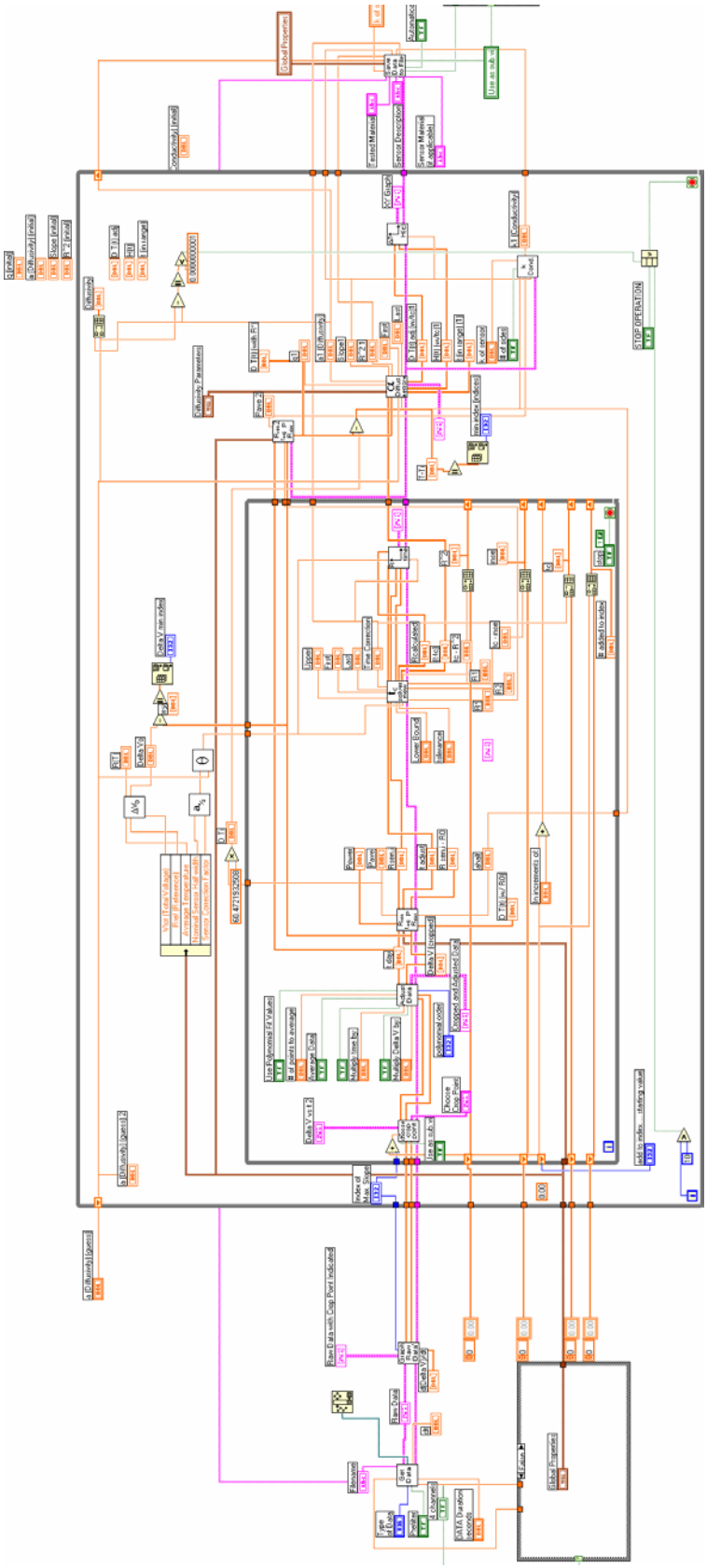

Figure A-5: LabVIEW block diagram of the data analysis program.

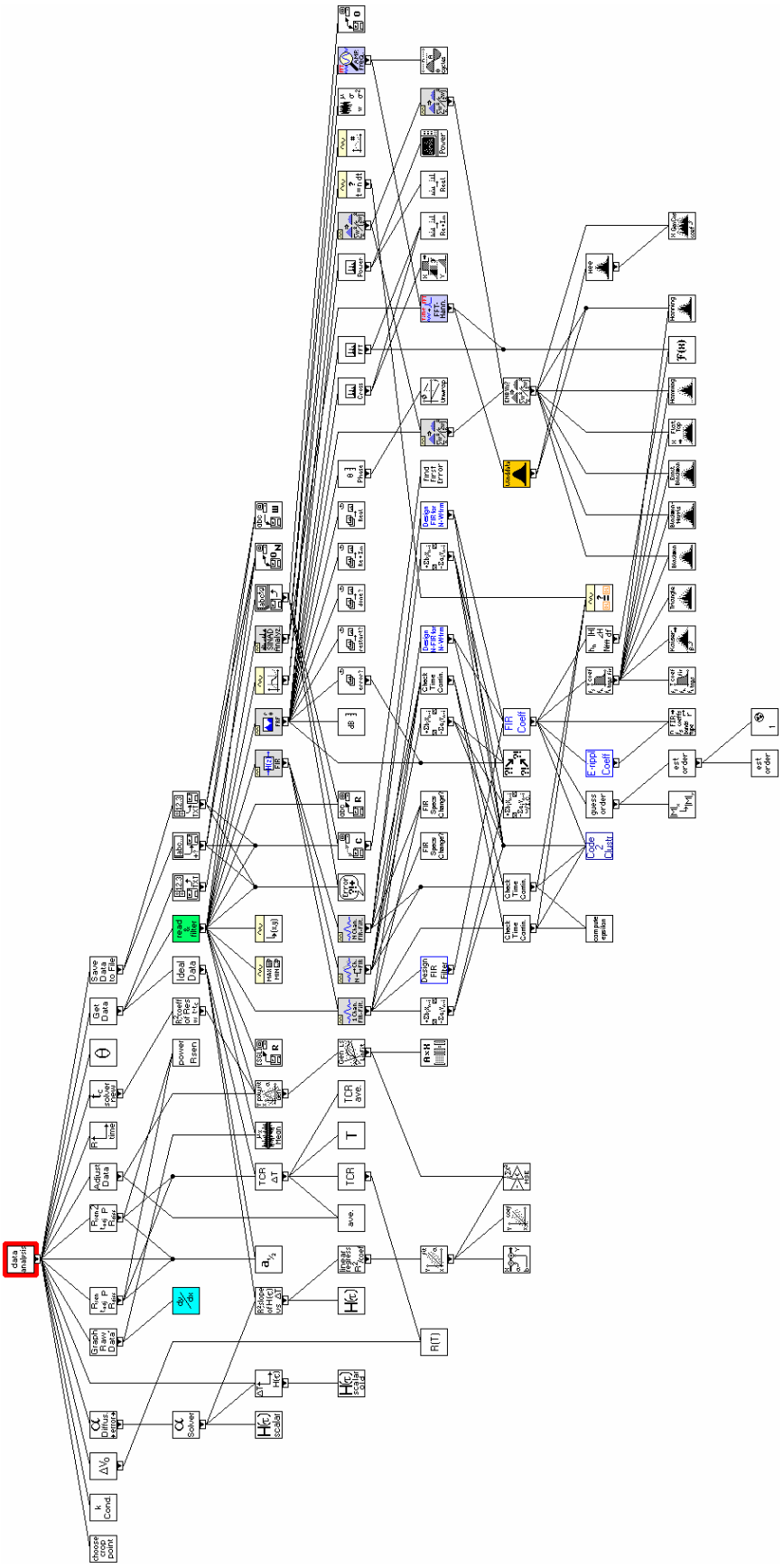

Figure A-6: Hierarchy of sub-VI's in data analysis program.

Choose Crop Point.vi

Connector Pane

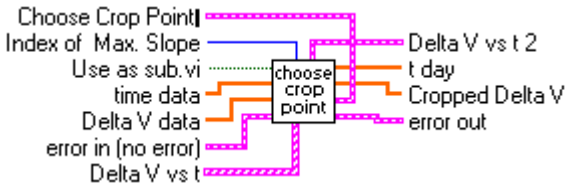

Block Diagram

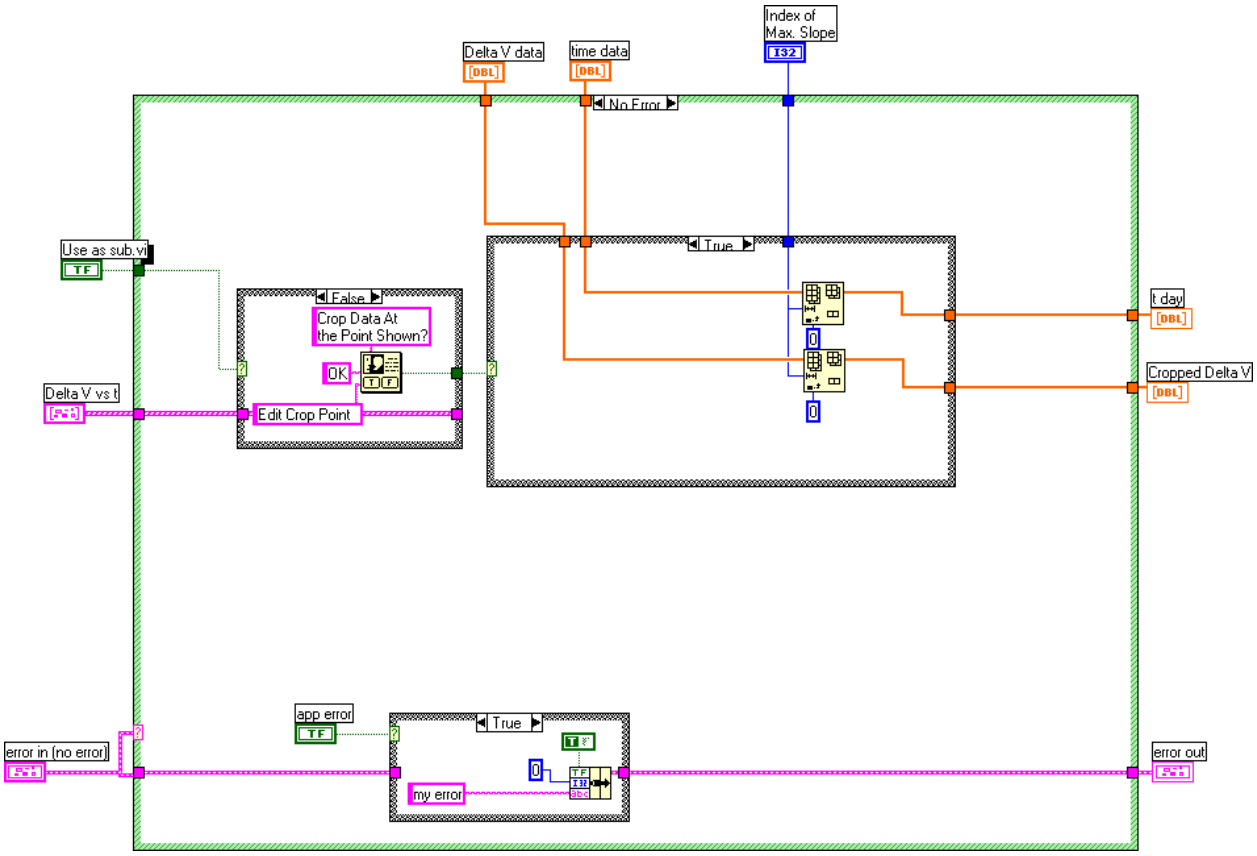

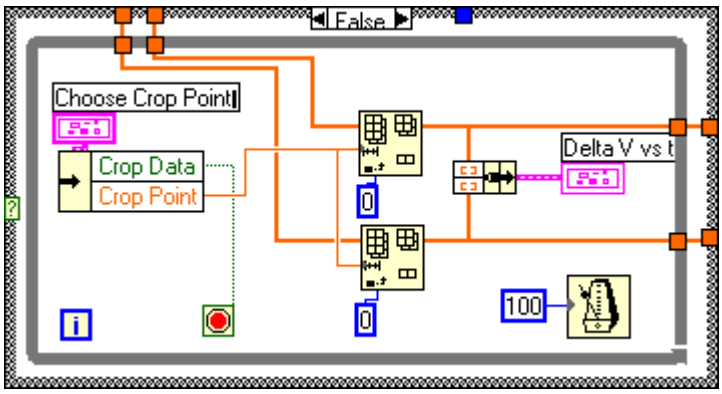
False
Choose Crop Point
Crop Data
Crop Point
Delta V vs t
0
0
100

Conductivity.vi

Connector Pane

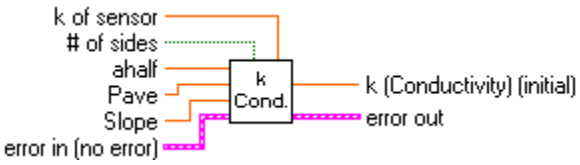

Front Panel

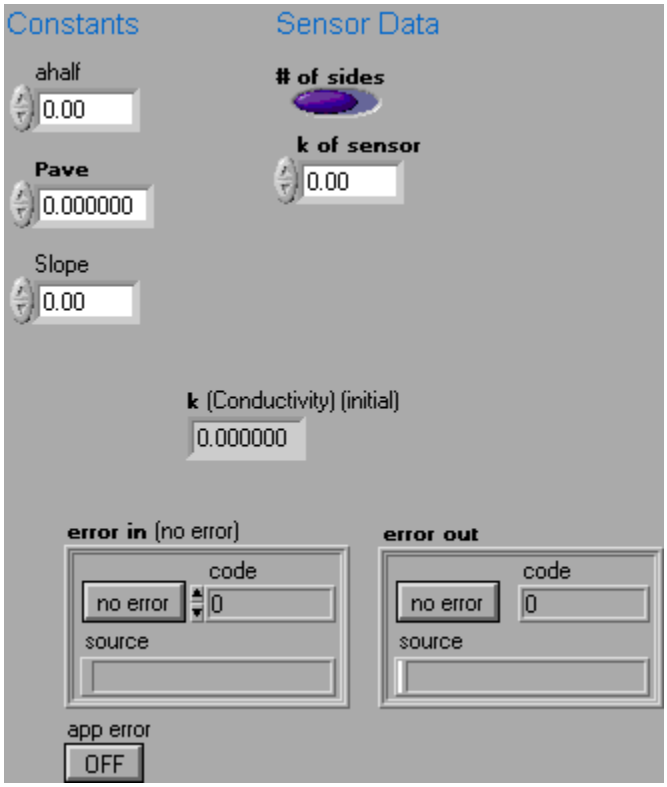

Block Diagram

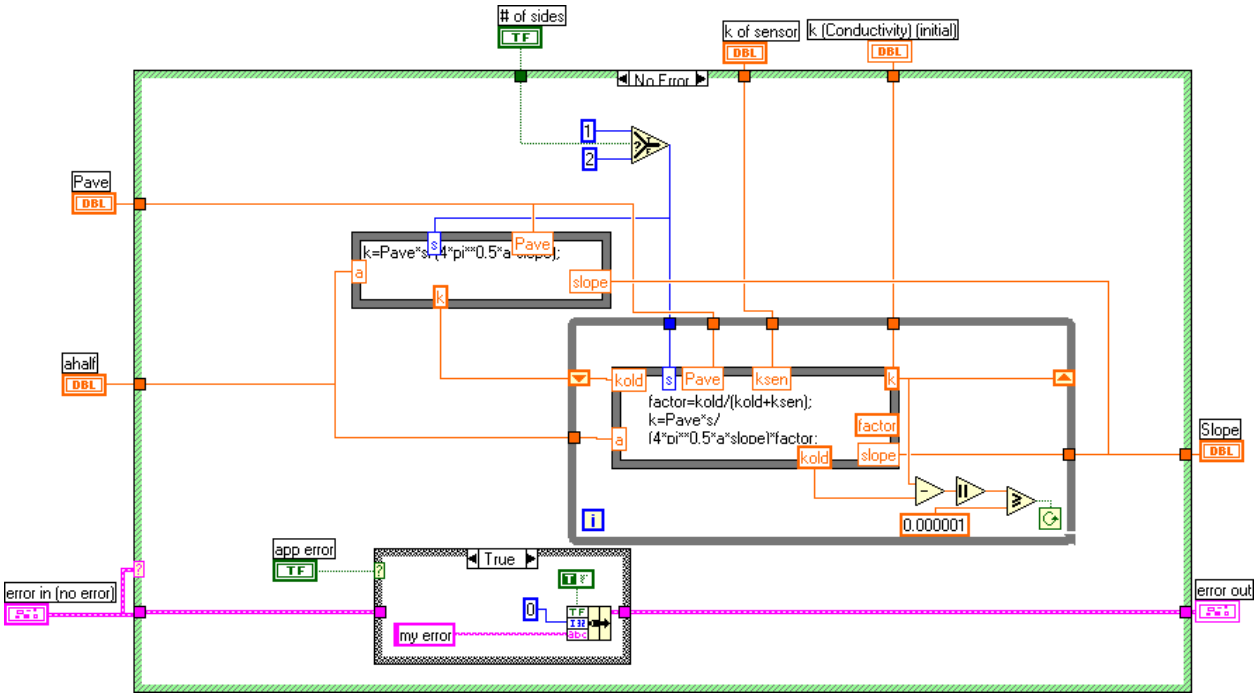

Delta Vo.vi

Connector Pane

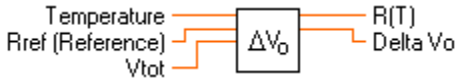

Block Diagram

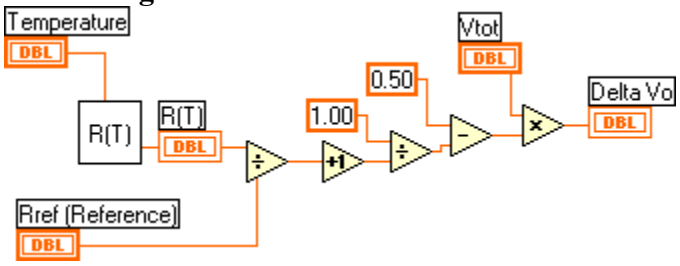

Diffusivity.vi

Connector Pane

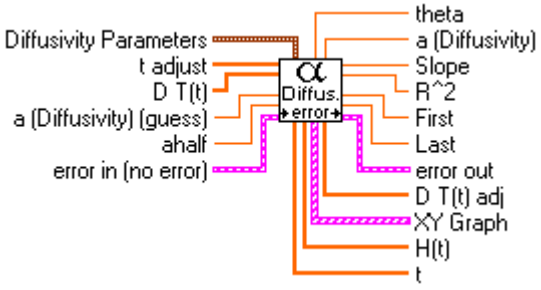

Block Diagram

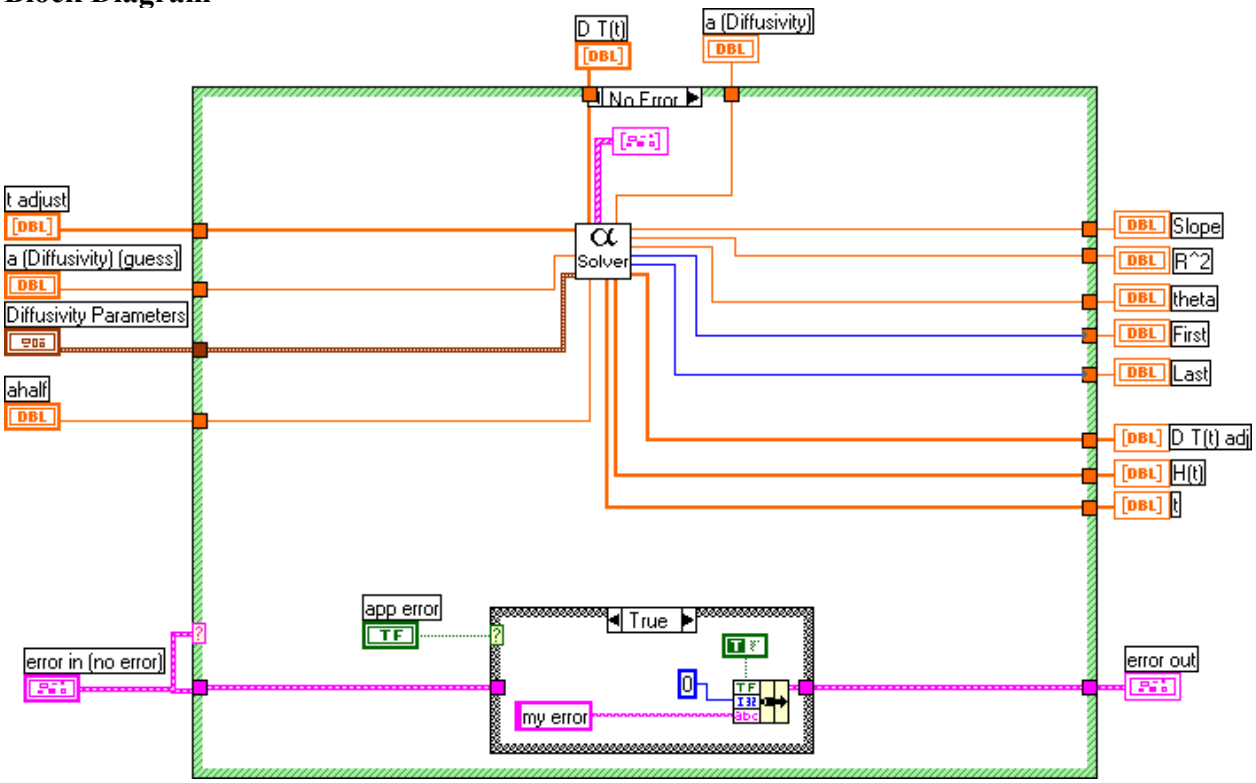

Diffusivity Solver.vi

Connector Pane

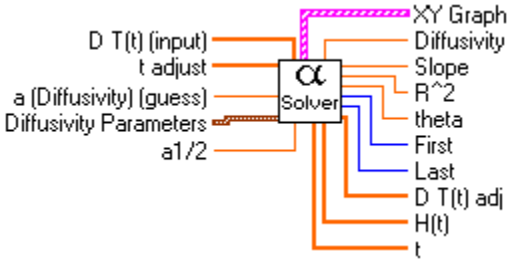

Front Panel

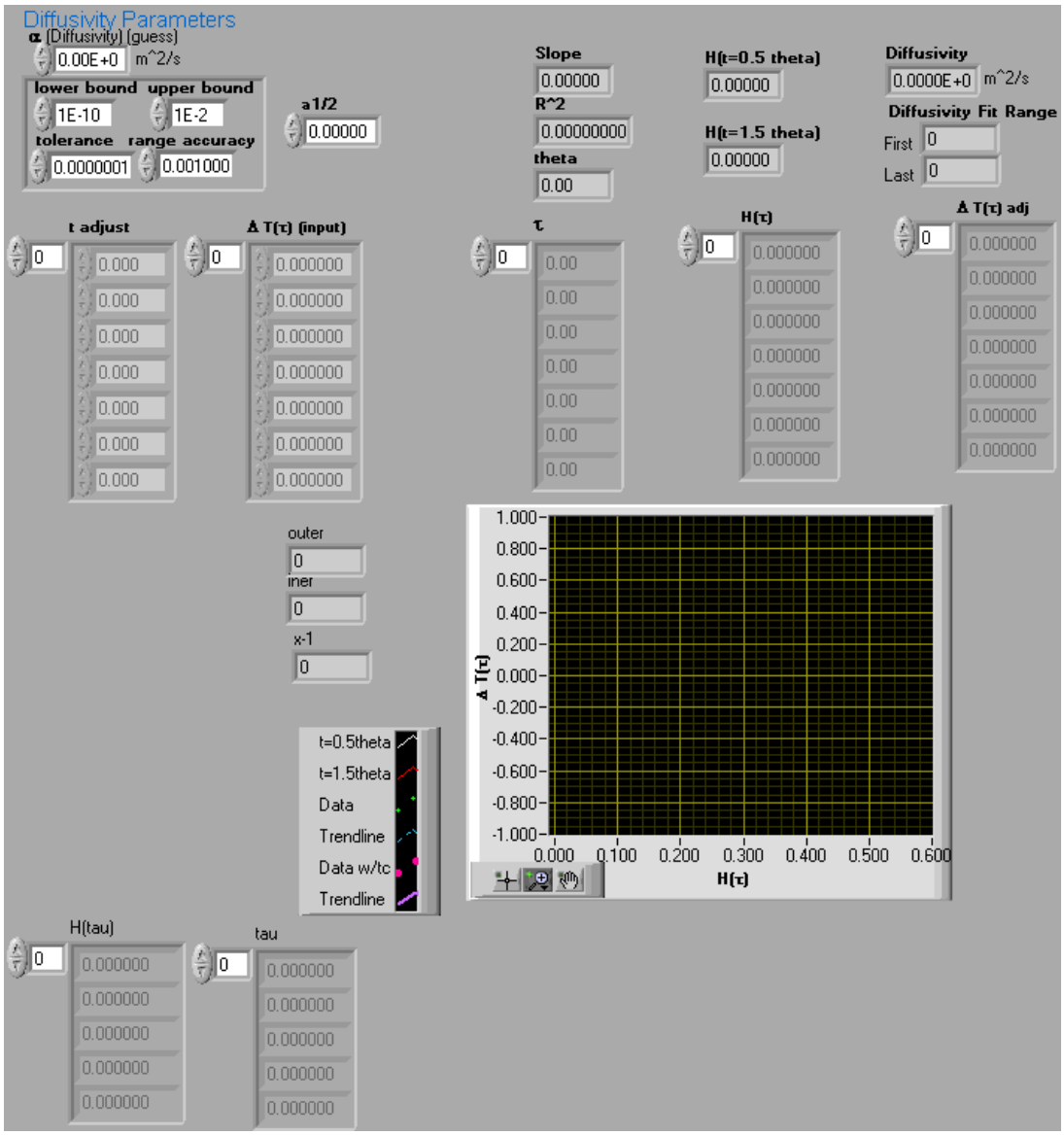

Block Diagram

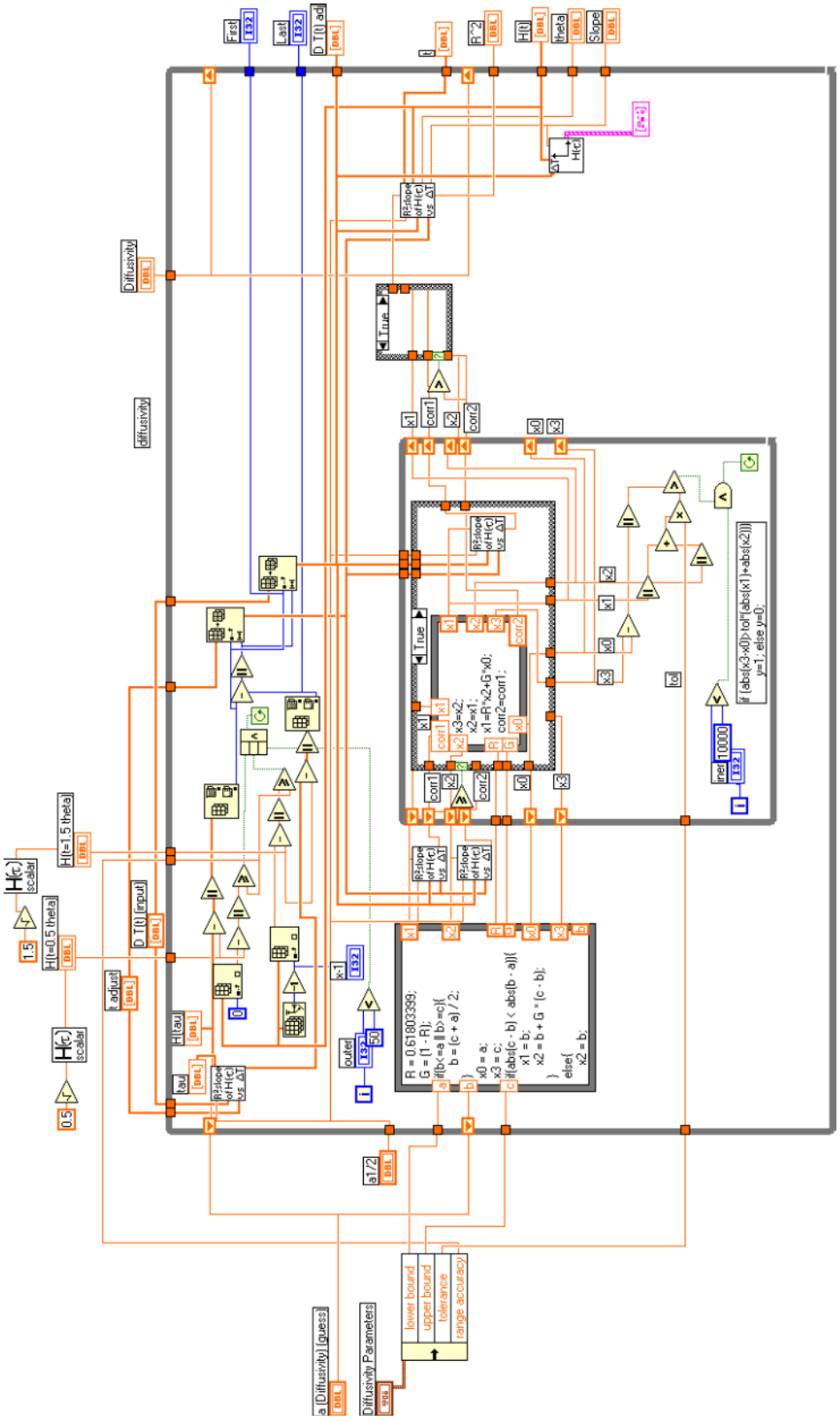

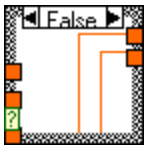
False
?

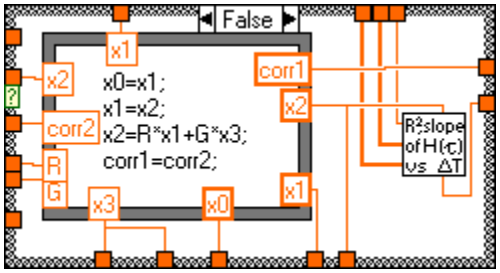
False
x1
x2
corr2
R
G
x3
x0
x0=x1;
x1=x2;
x2=R*x1+G*x3;
corr1=corr2;
corr1
x2
x1
R²slope
of H(τ)
vs ΔT

H(tau)_scalar.vi

Connector Pane

Block Diagram

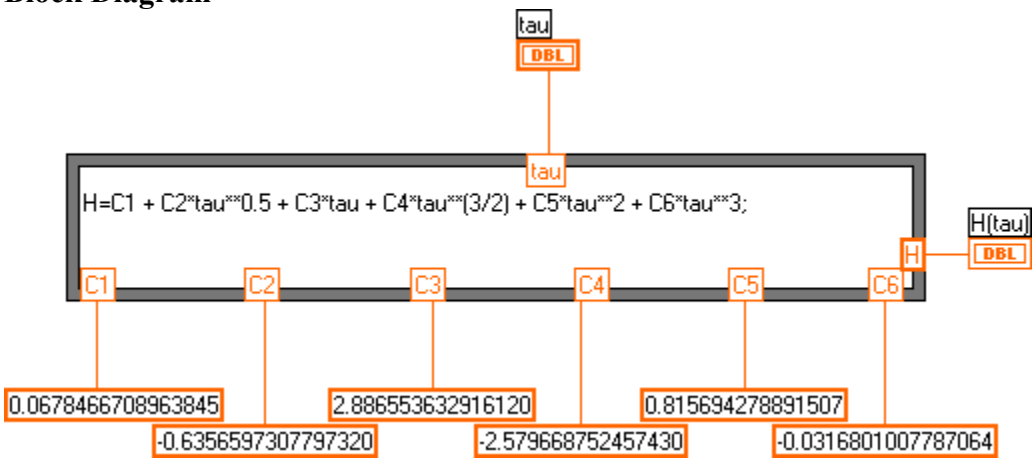

corr-slope_HvsT.vi

Connector Pane

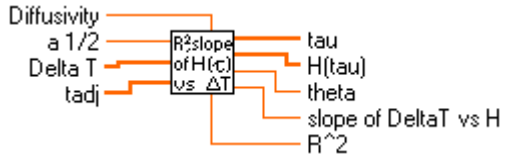

Block Diagram

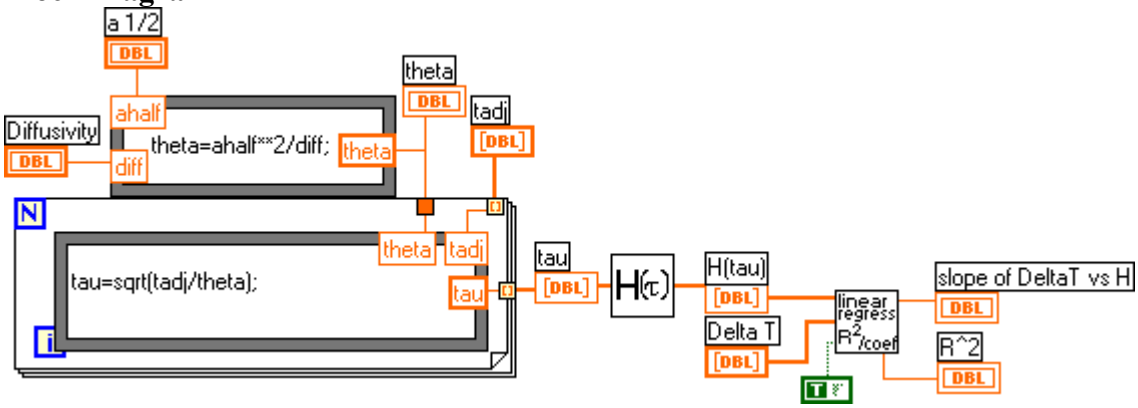

H(tau).vi

Connector Pane

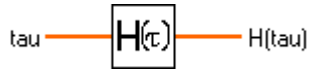

Block Diagram

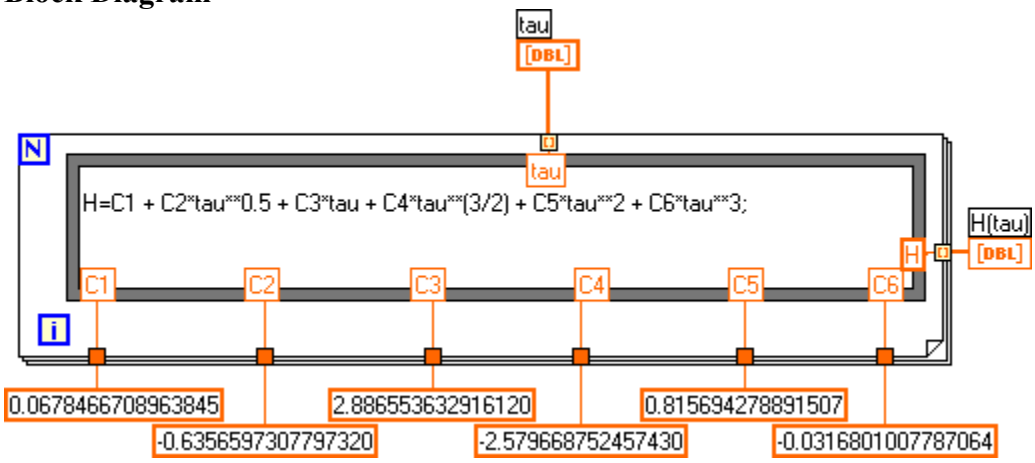

LinReg_origin.vi

Connector Pane

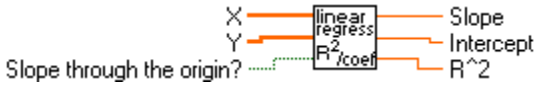

Block Diagram

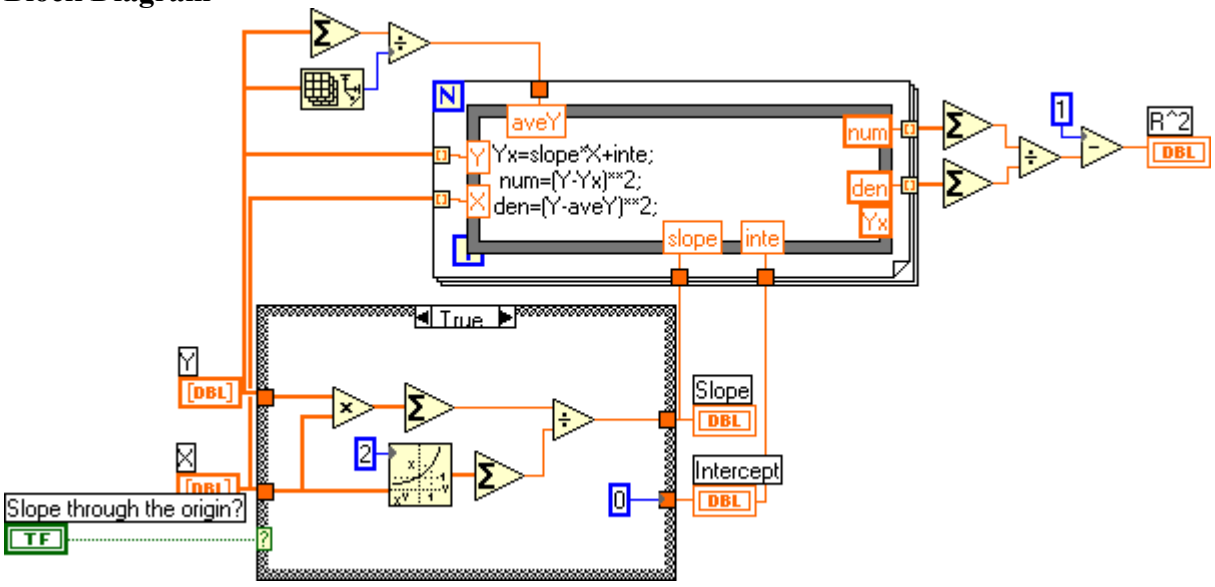

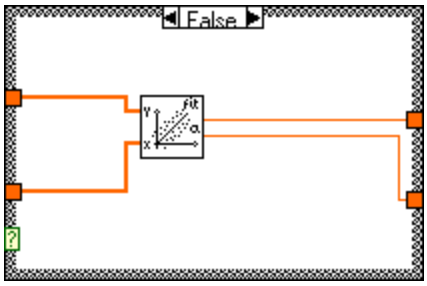

Delta T vs H(tau) graph.vi

Connector Pane

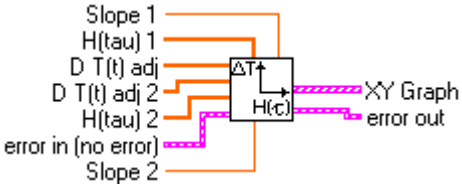

Block Diagram

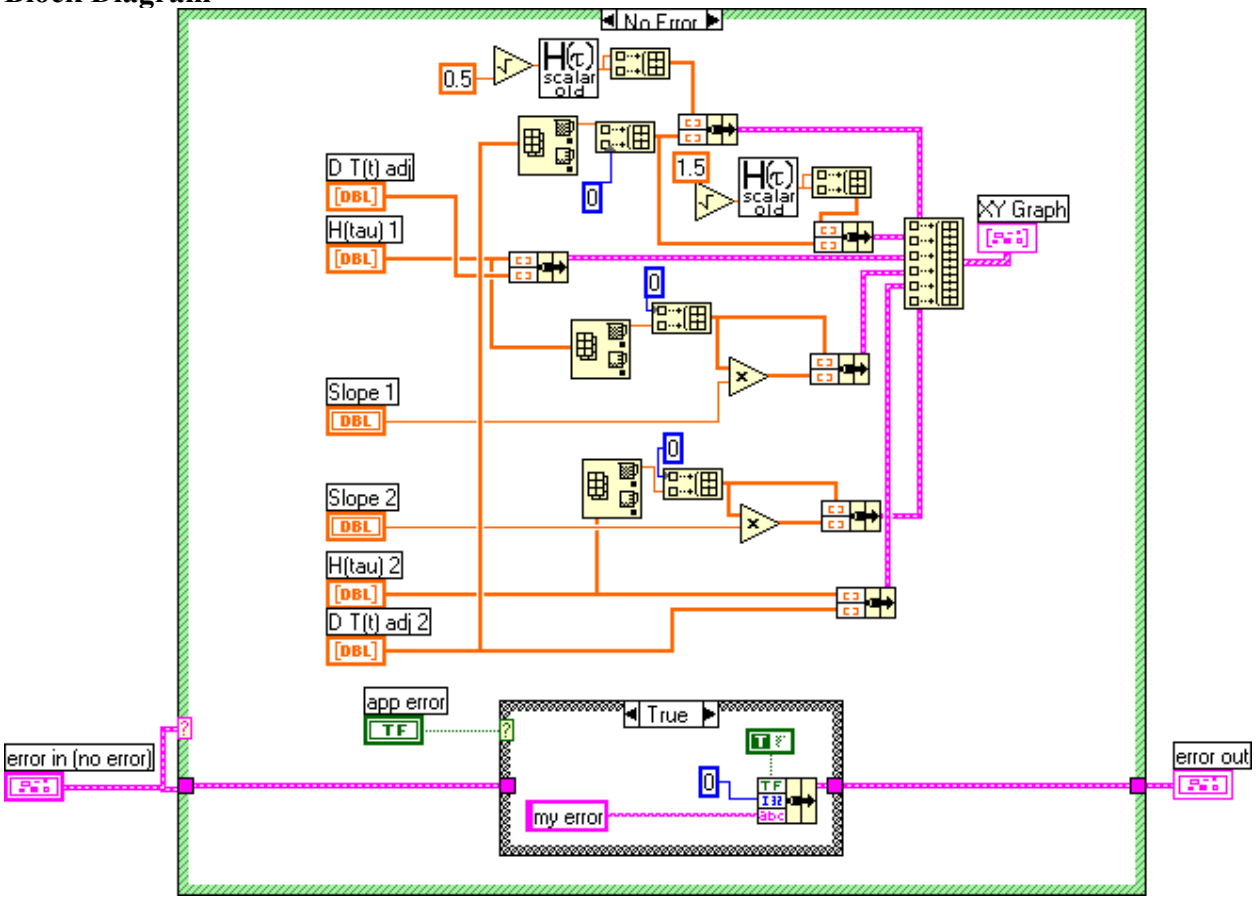

Graph Raw Data02.vi

Connector Pane

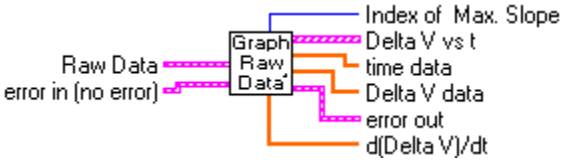

Block Diagram

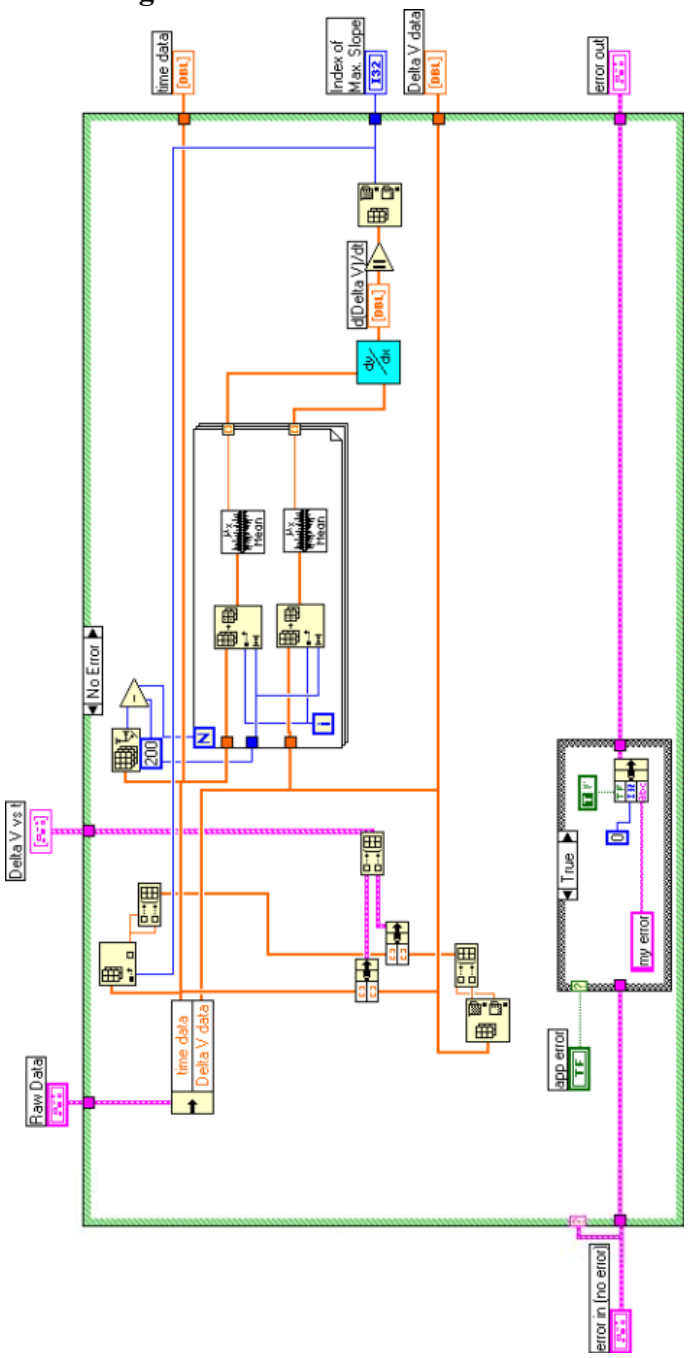

1st derivative.vi

Connector Pane

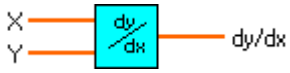

Block Diagram

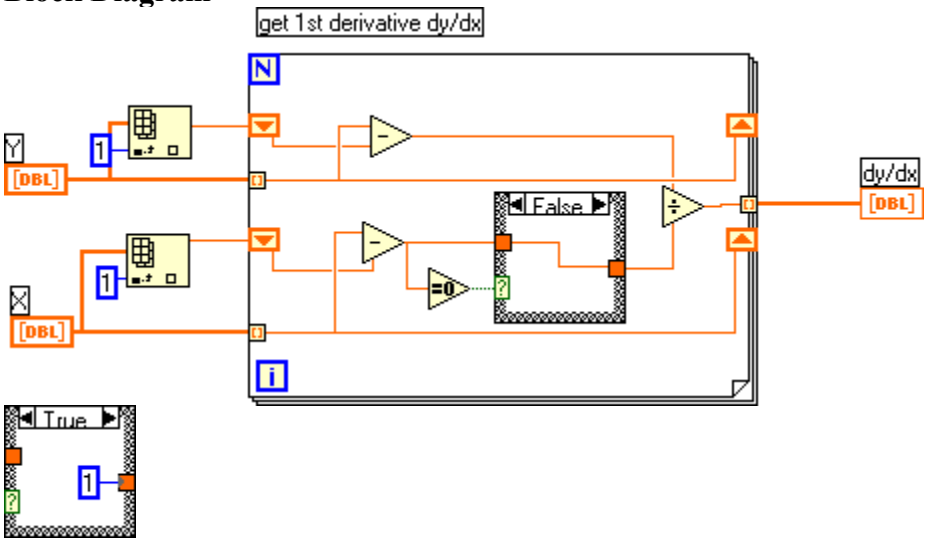

Intermediate Calculations.vi

Connector Pane

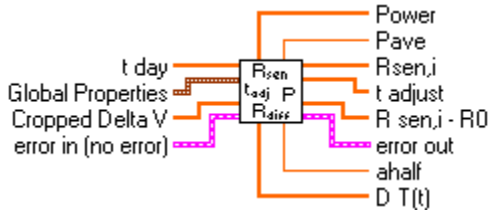

Block Diagram

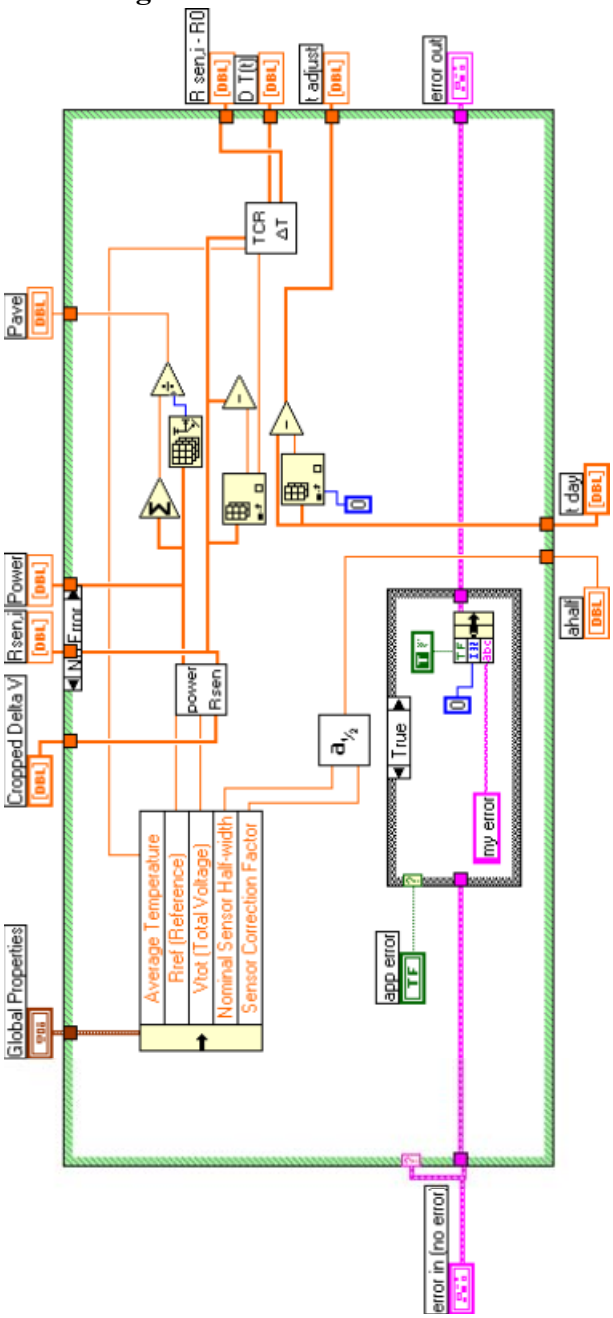

sensor half width.vi

Connector Pane

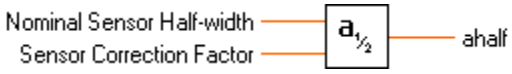

Block Diagram

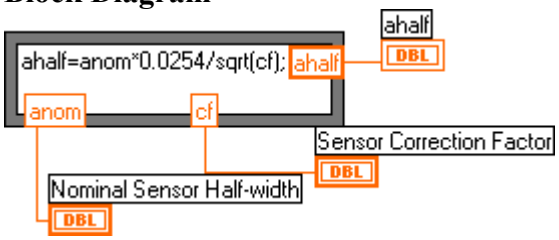

TCR & Delta T03.vi

Connector Pane

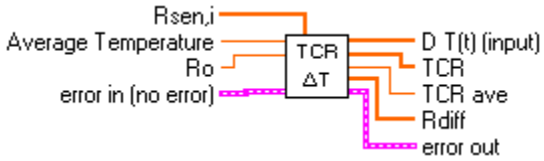

Block Diagram

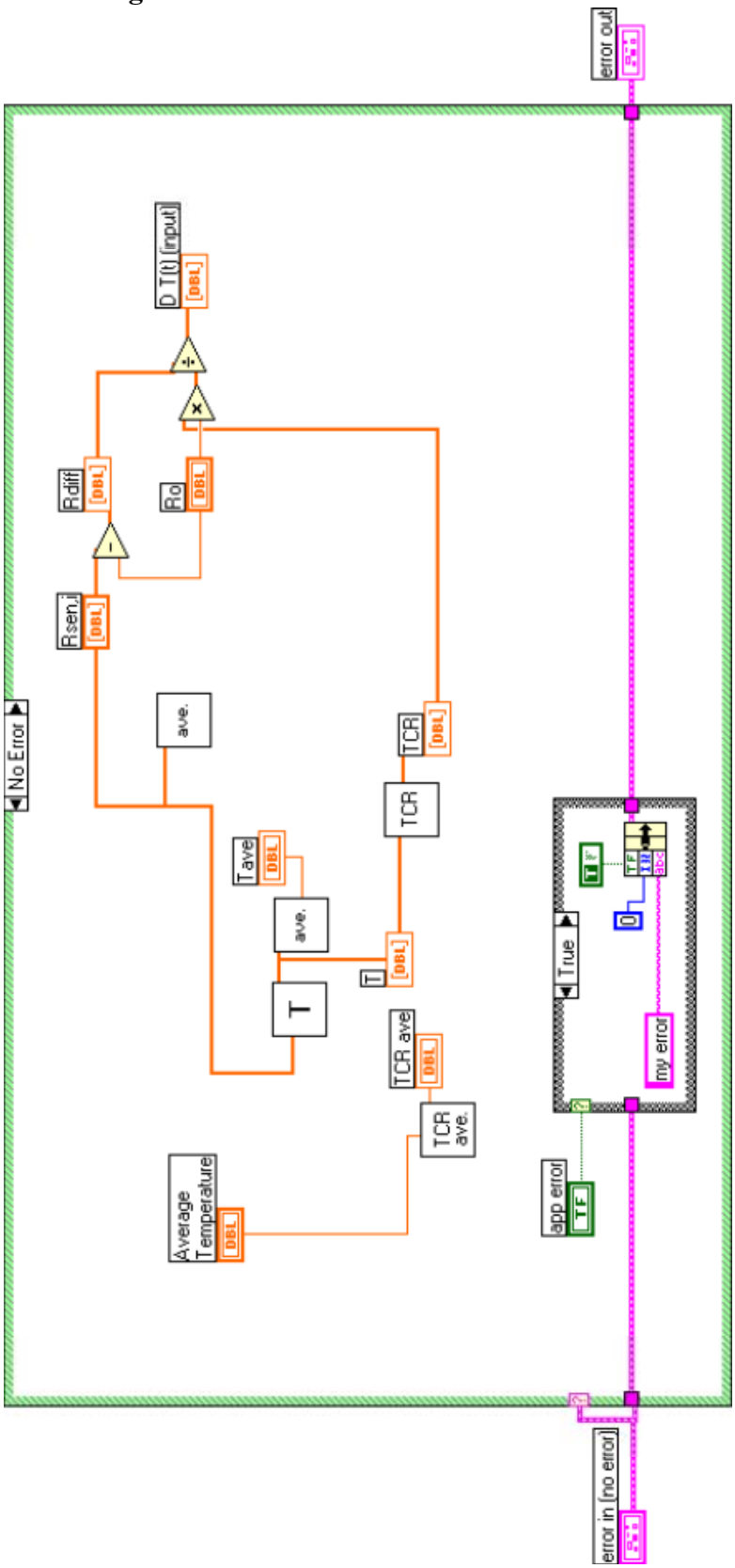

Average.vi

Connector Pane

Block Diagram

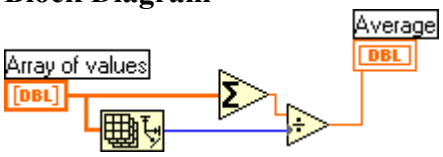

TCR.vi

Connector Pane

Block Diagram

Coefficients from Vishay's web page
http://www.vishay.com/brands/measurements_group/guide/tn/tn506/506m.htm

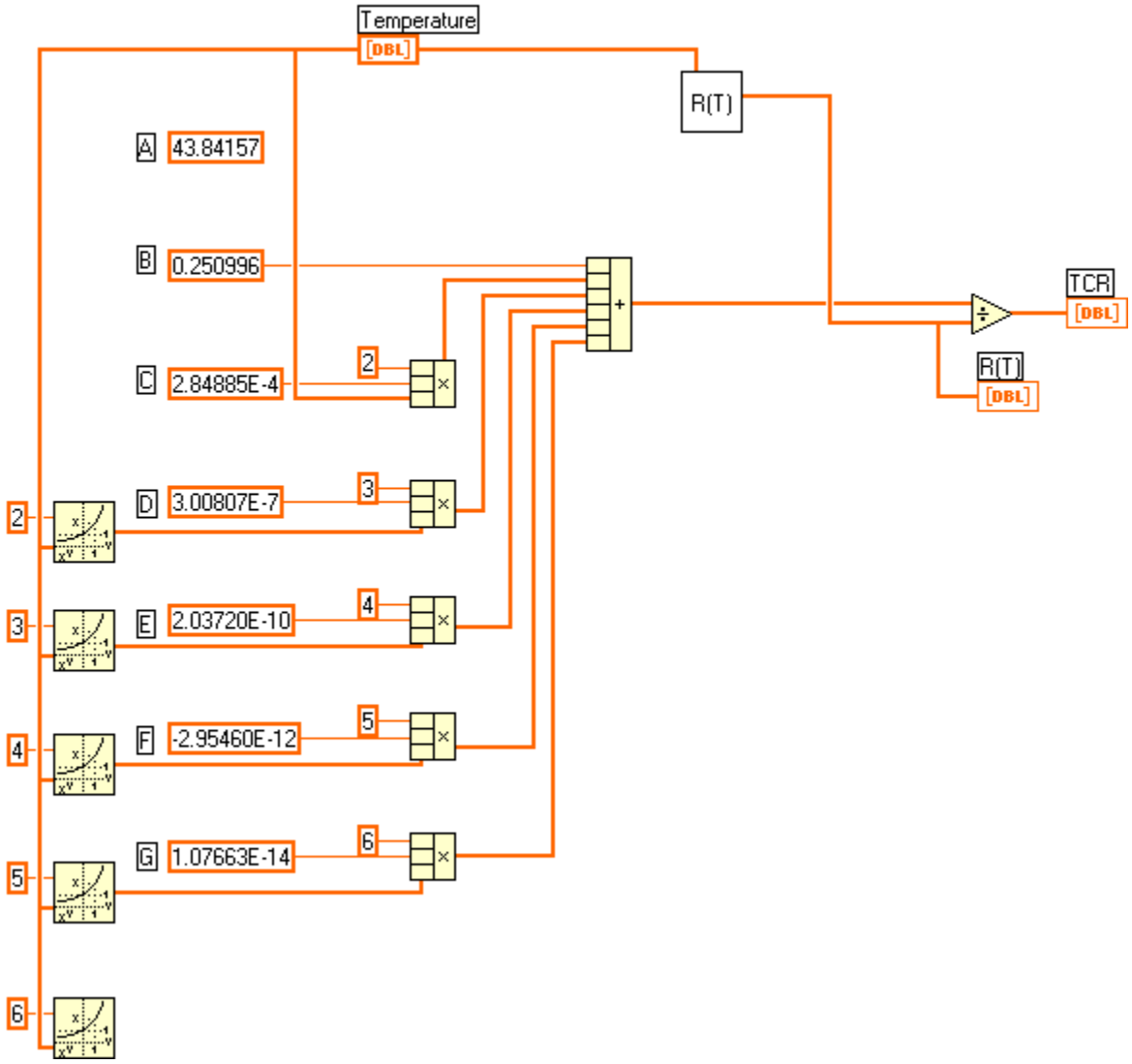

R(T).vi

Connector Pane

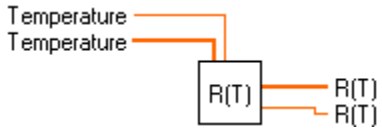

Block Diagram

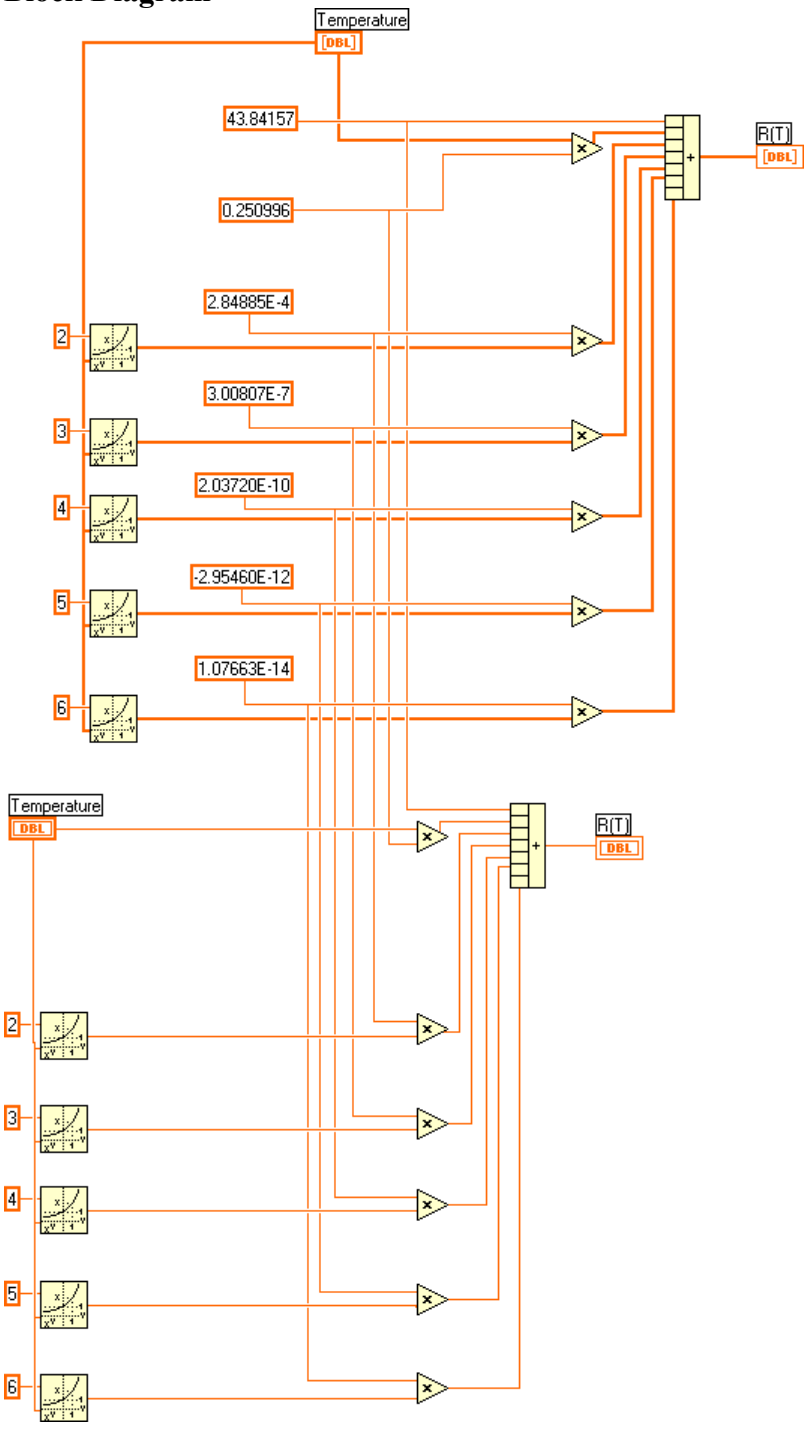

T.vi

Connector Pane

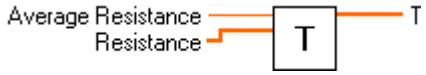

Block Diagram

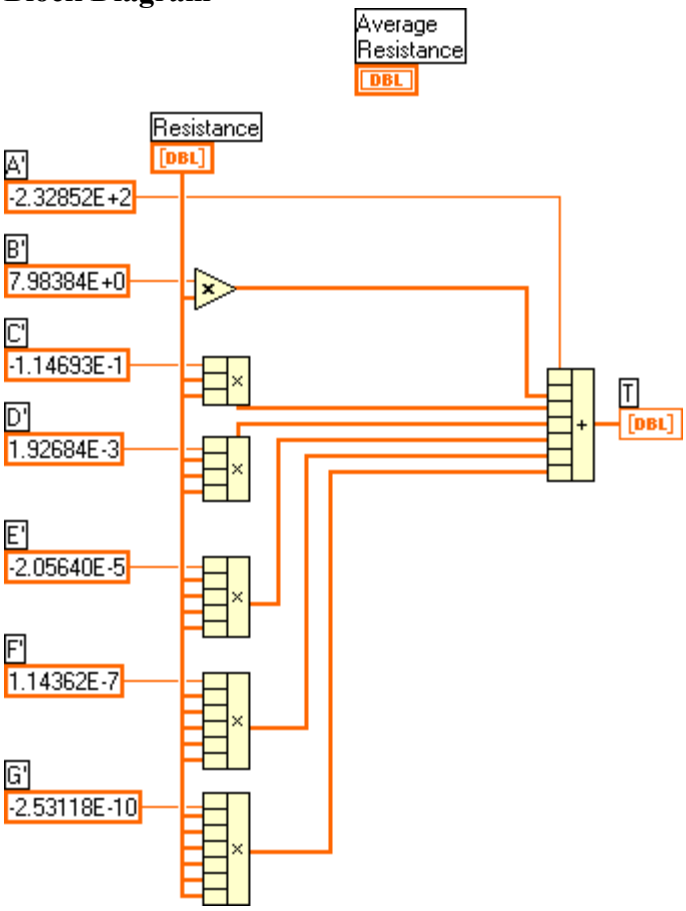

TCRave.vi

Connector Pane

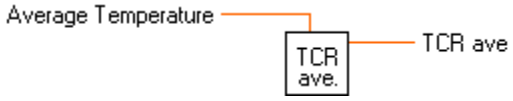

Block Diagram

Coefficients from Vishay's web page
http://www.vishay.com/brands/measurements_group/guide/tn/tn506/506m.htm

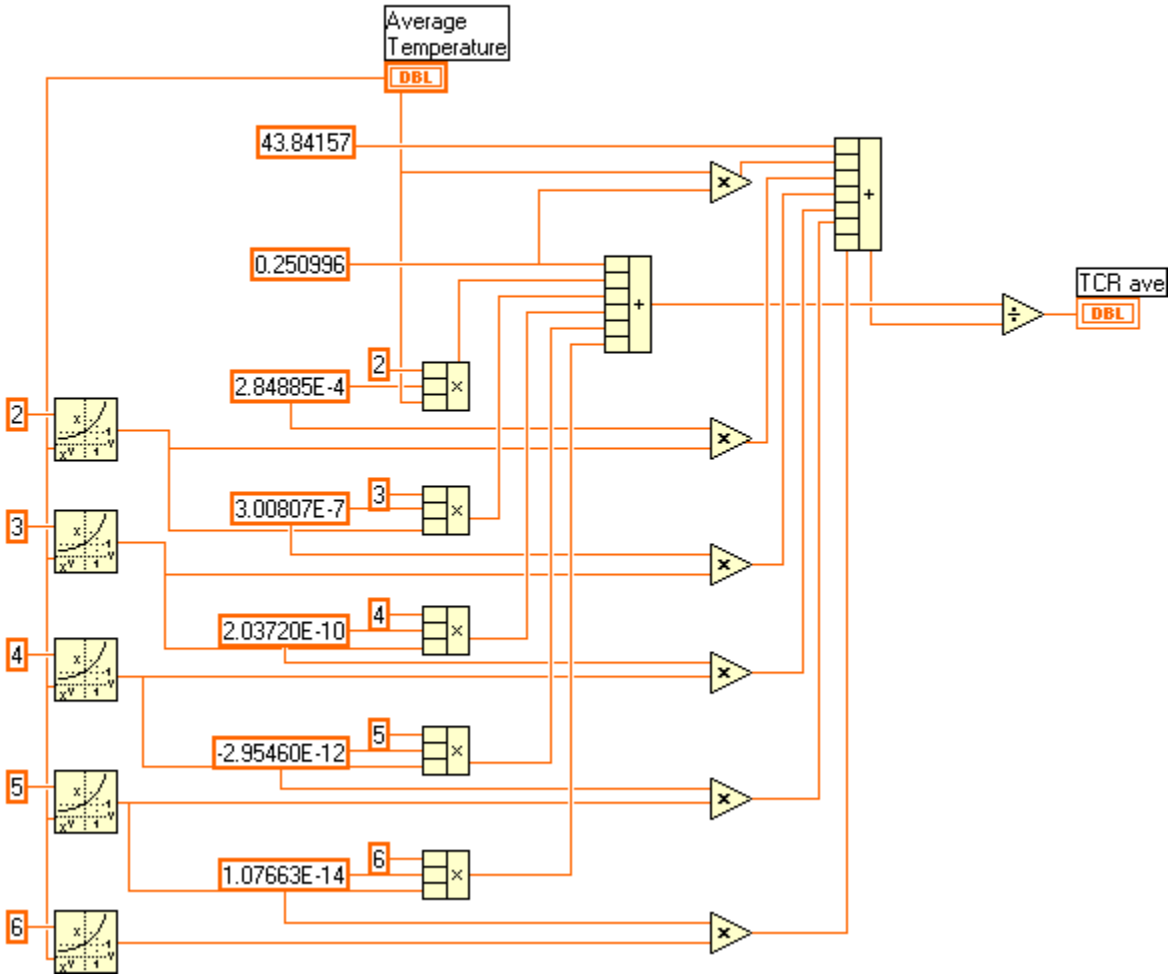

Power & Rsen.vi

Connector Pane

Block Diagram

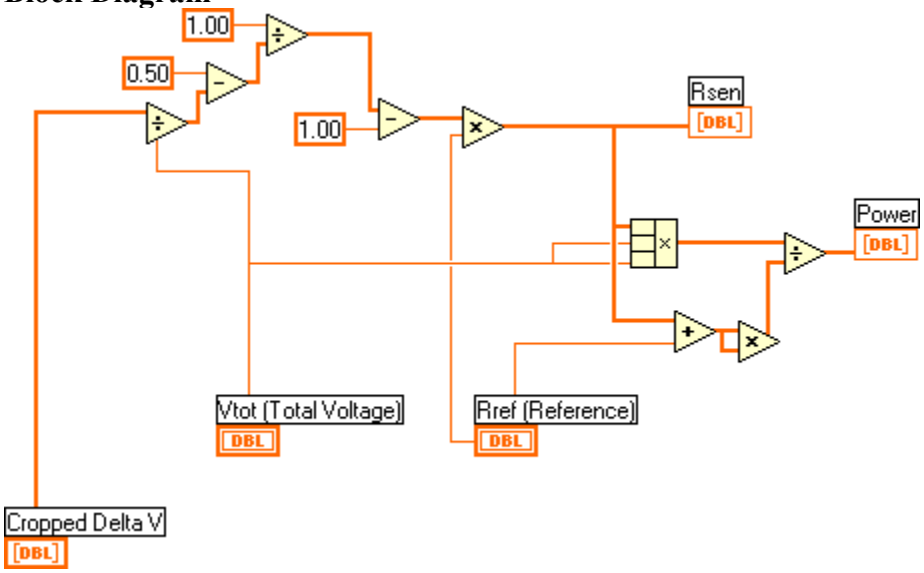

Intermediate Calculations02.vi

Connector Pane

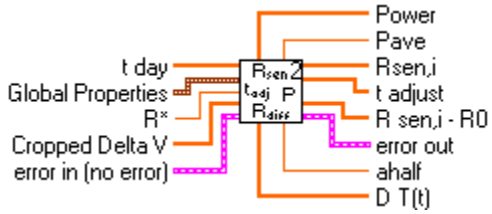

Block Diagram

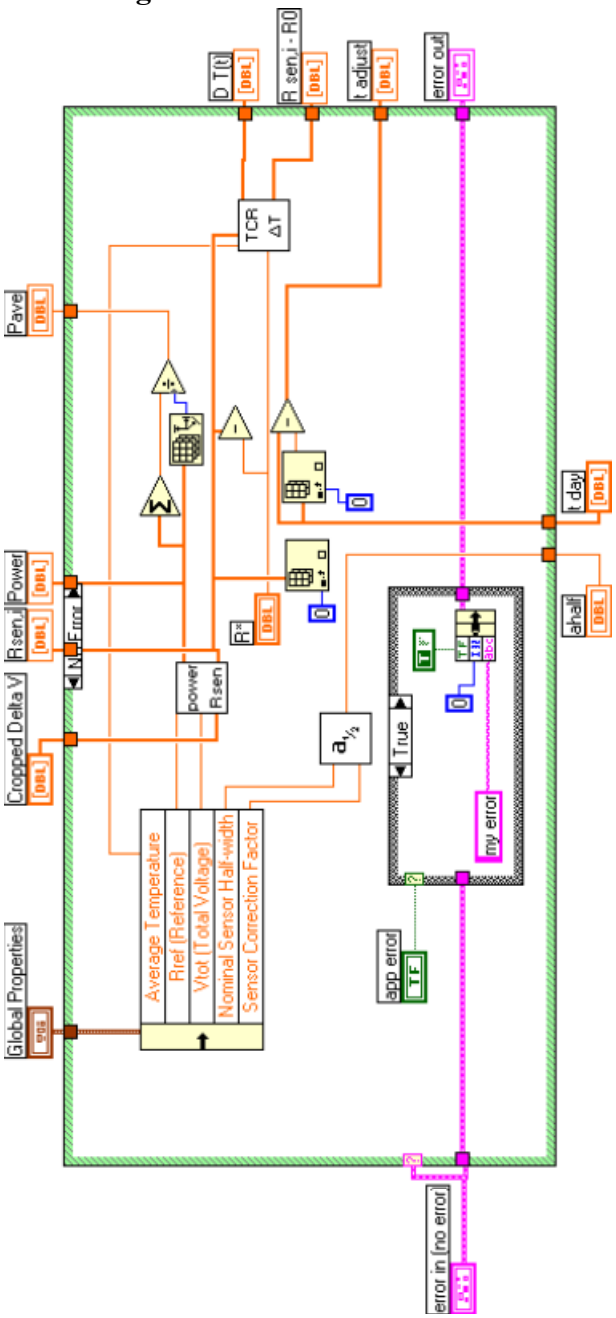

Data Modification.vi

Connector Pane

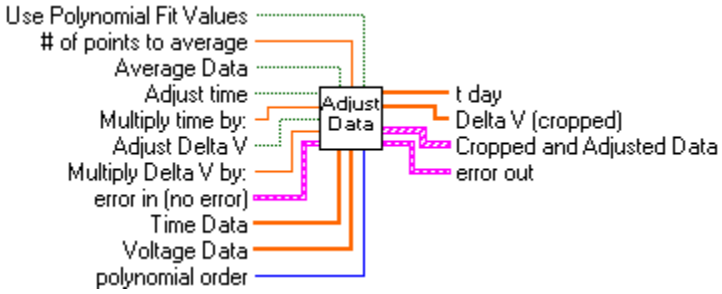

Block Diagram

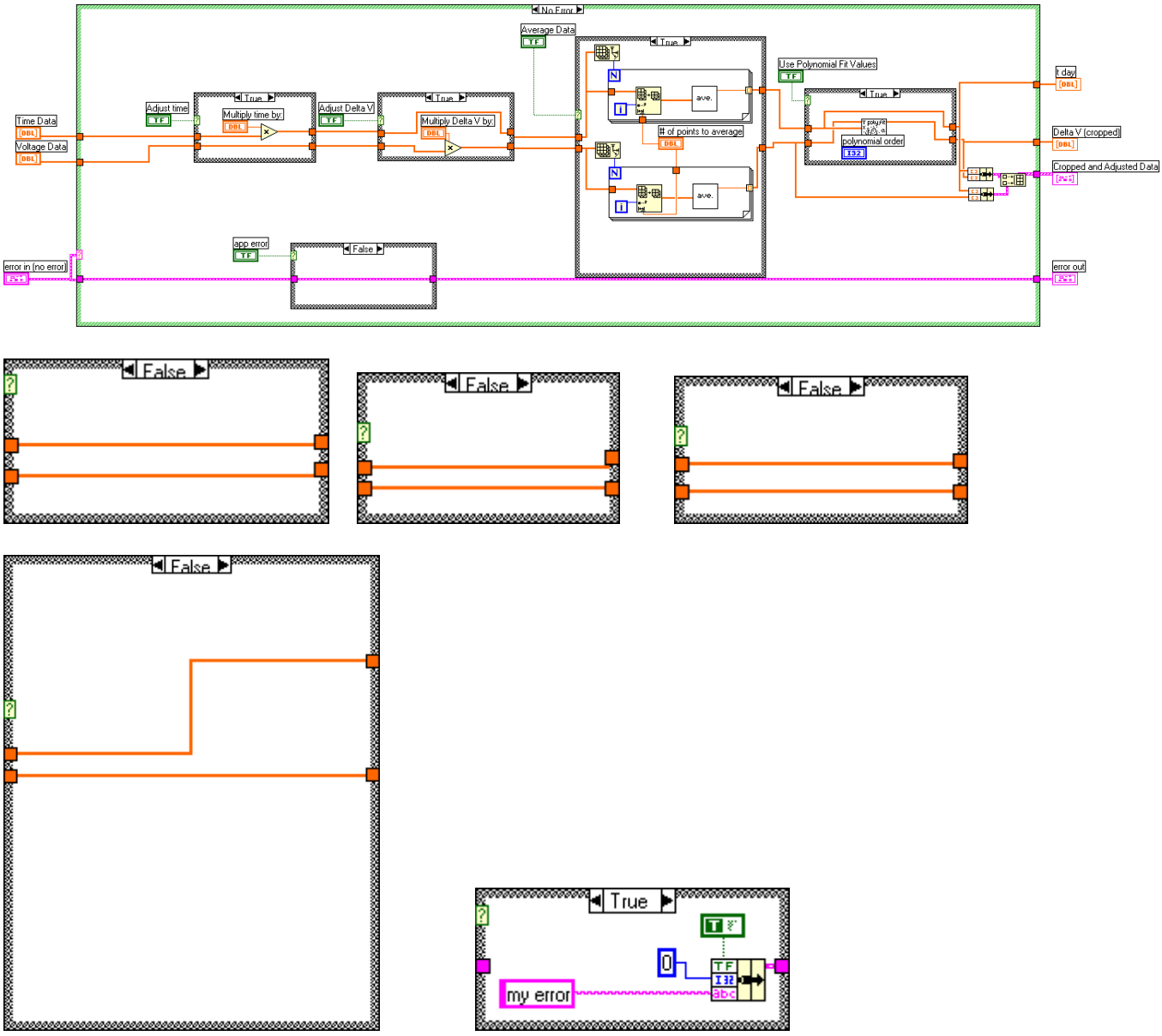

tc graph.vi

Connector Pane

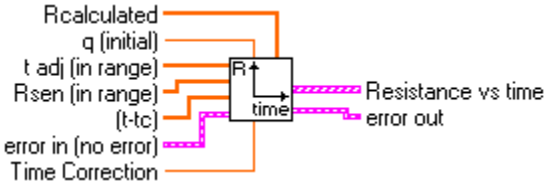

Block Diagram

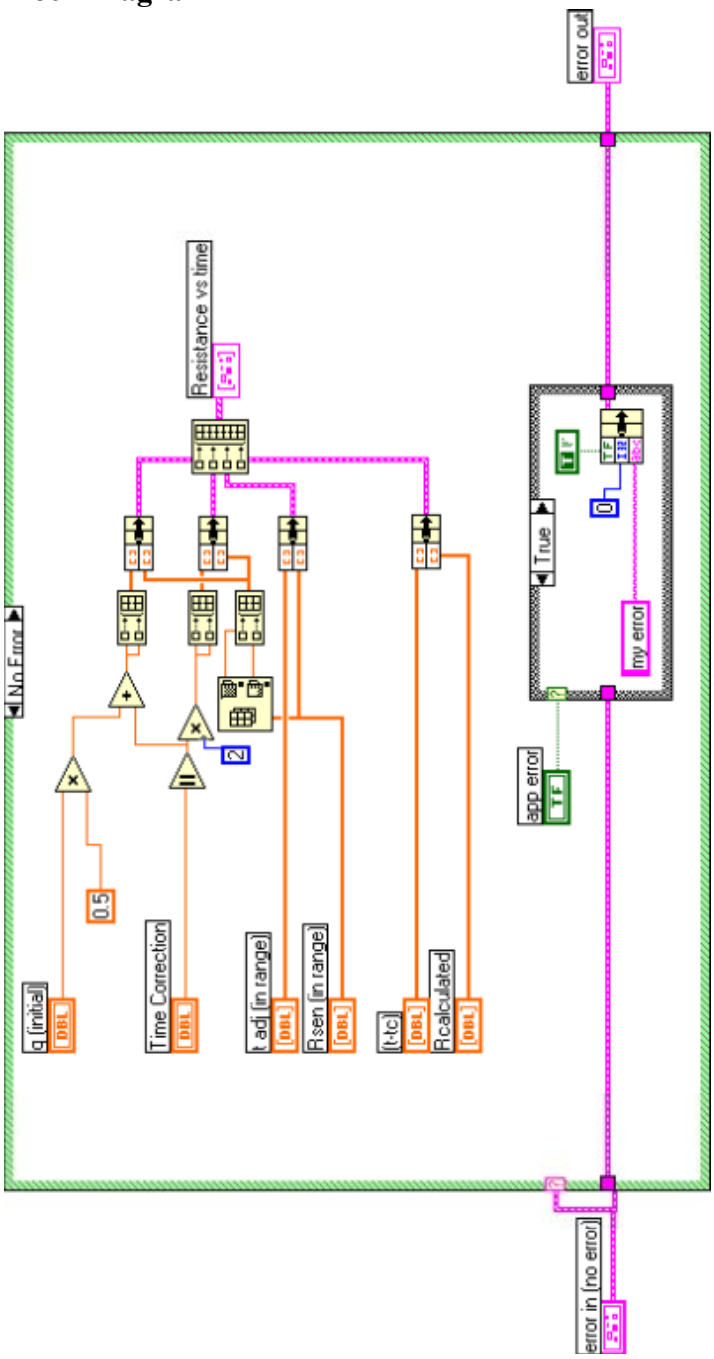

tc solver adjusted03.vi

Connector Pane

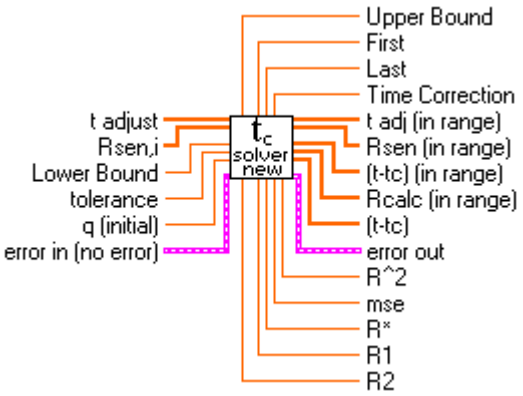

Front Panel

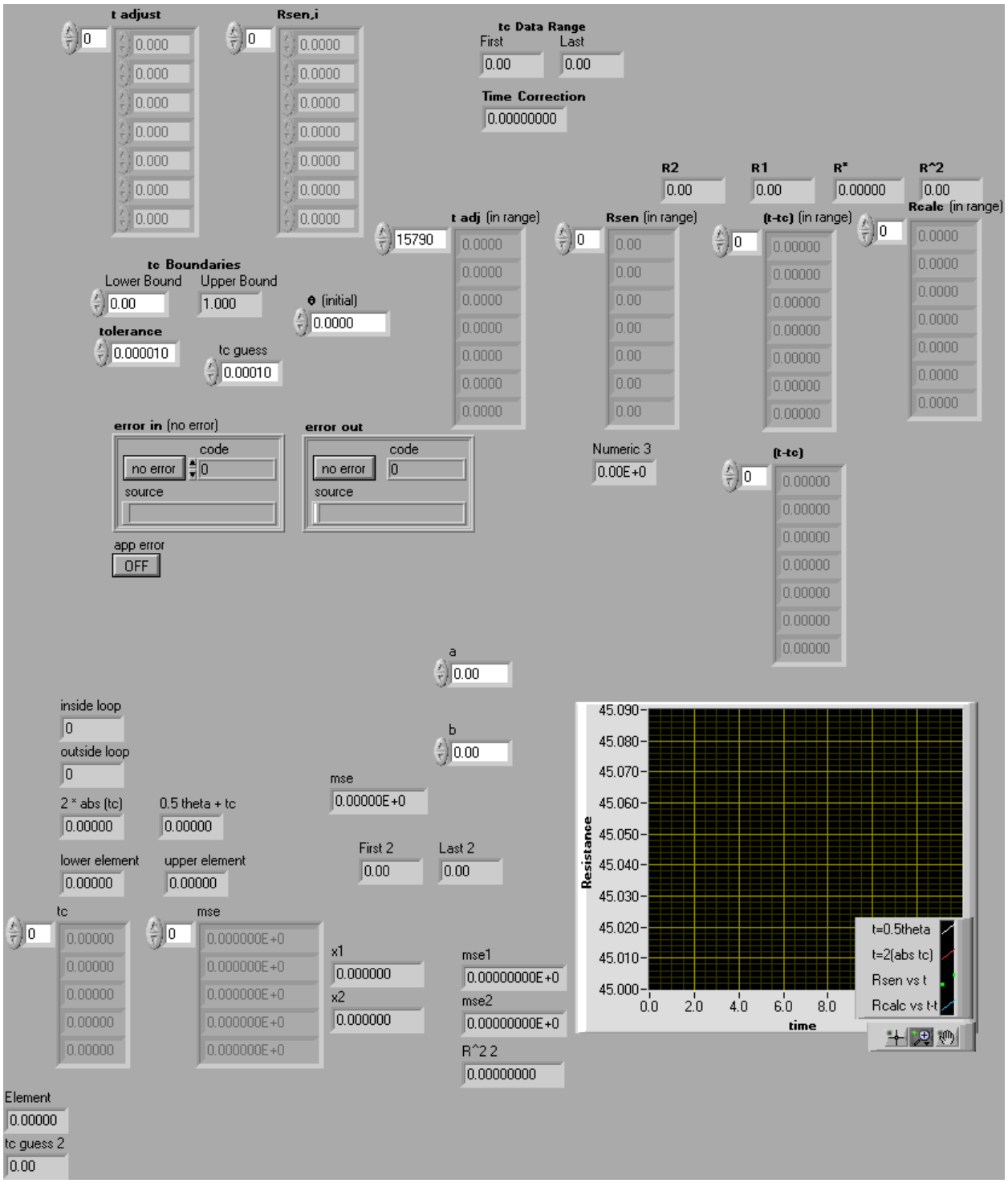
t adjust
Rsen,i
tc Data Range
First
Last
Time Correction
R2
R1
R*
R^2
t adj (in range)
Rsen (in range)
(t-tc) (in range)
Rcalc (in range)
tc Boundaries
Lower Bound
Upper Bound
θ (initial)
tolerance
tc guess
error in (no error)
error out
code
source
no error
app error
OFF
Numeric 3
(t-tc)
a
b
inside loop
outside loop
mse
2 * abs (tc)
0.5 theta + tc
First 2
Last 2
lower element
upper element
tc
x1
x2
mse1
mse2
R^2 2
Element
tc guess 2
Resistance
time
t=0.5theta
t=2(abs tc)
Rsen vs t
Rcalc vs t-t

Block Diagram

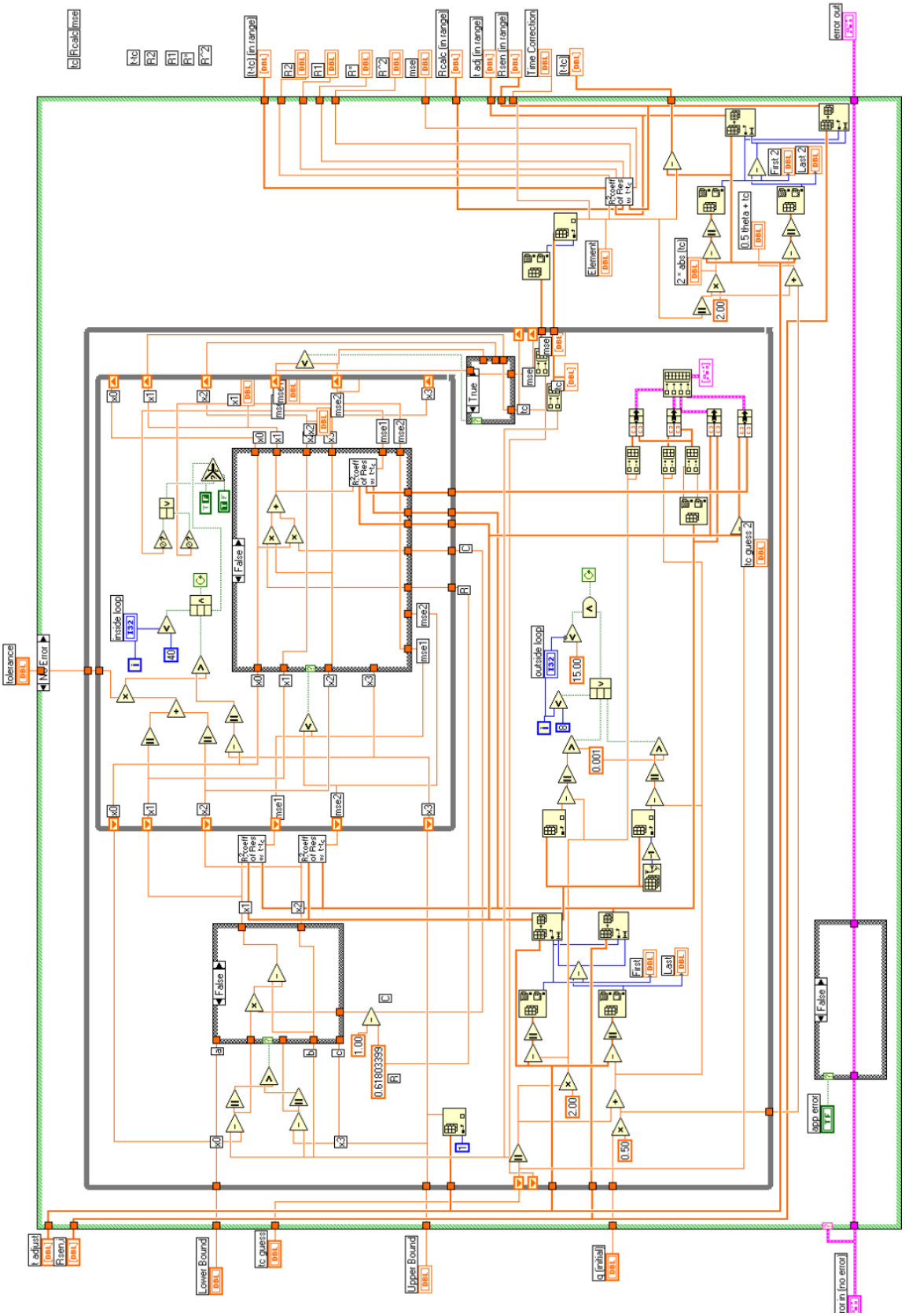

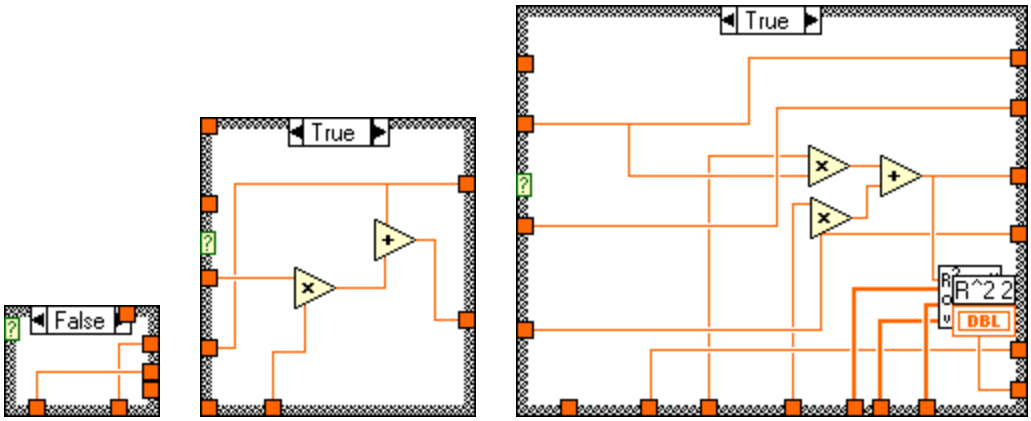
False
True
True
R^2 2
DBL

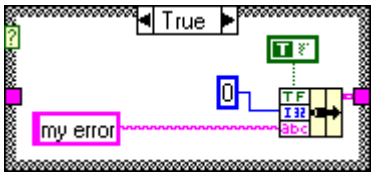
True
T
0
TF
I32
abc
my error

Res_vs_tc_coeff.vi

Connector Pane

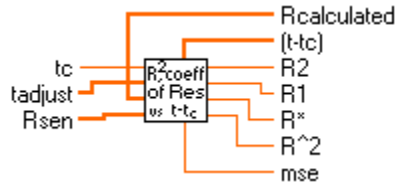

Block Diagram

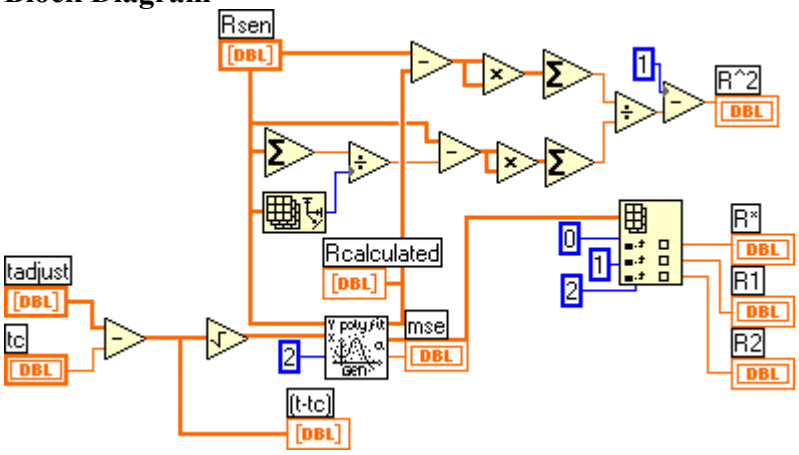

Theta.vi

Connector Pane

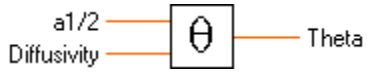

Block Diagram

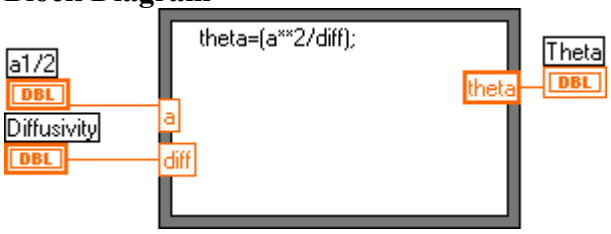

Retrieve Data.vi

Connector Pane

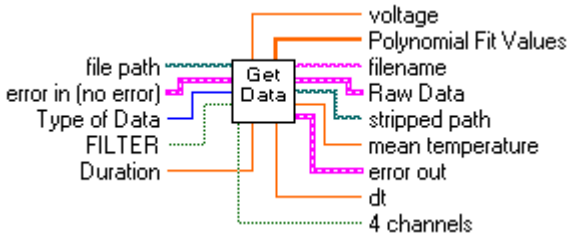

Block Diagram

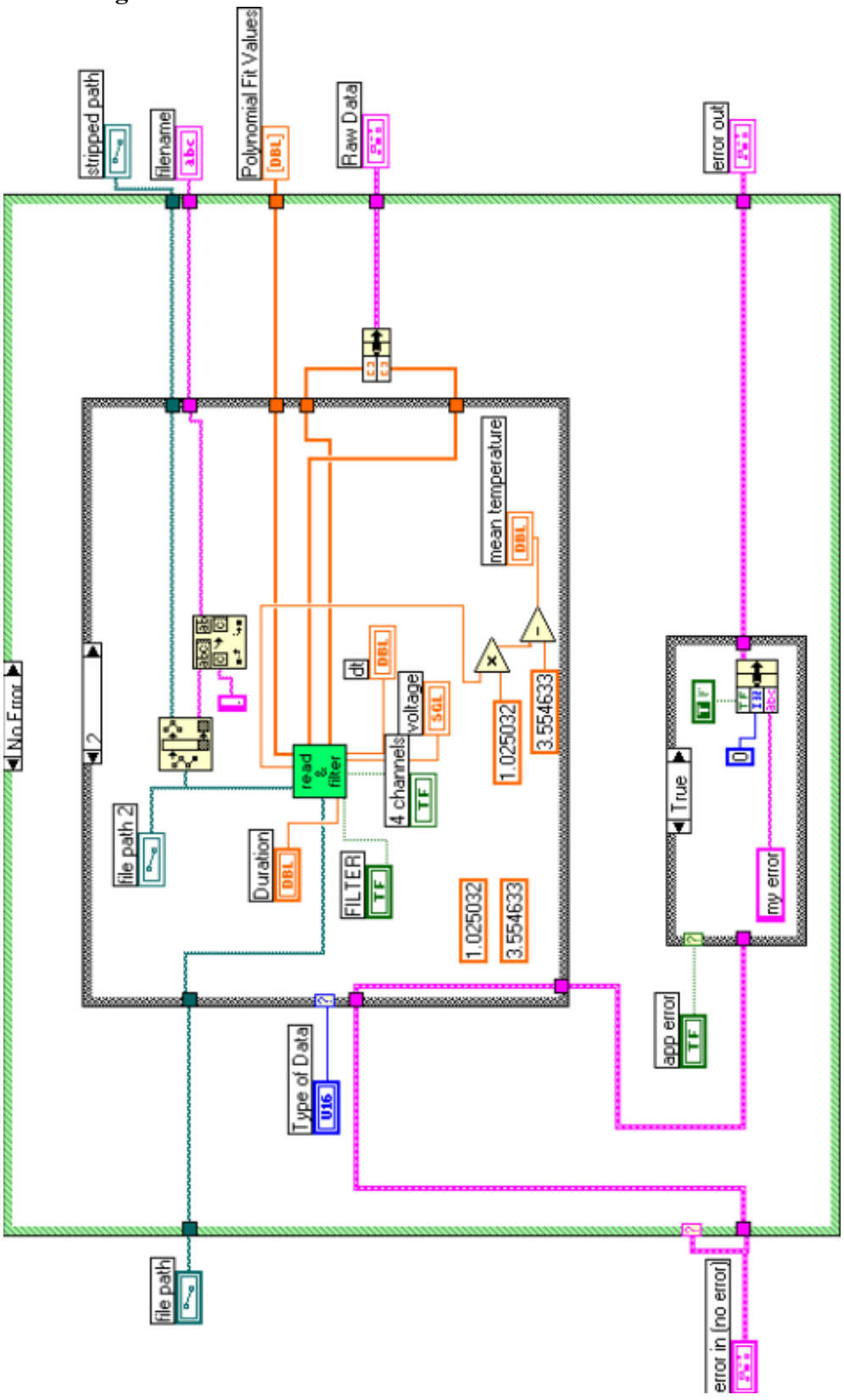

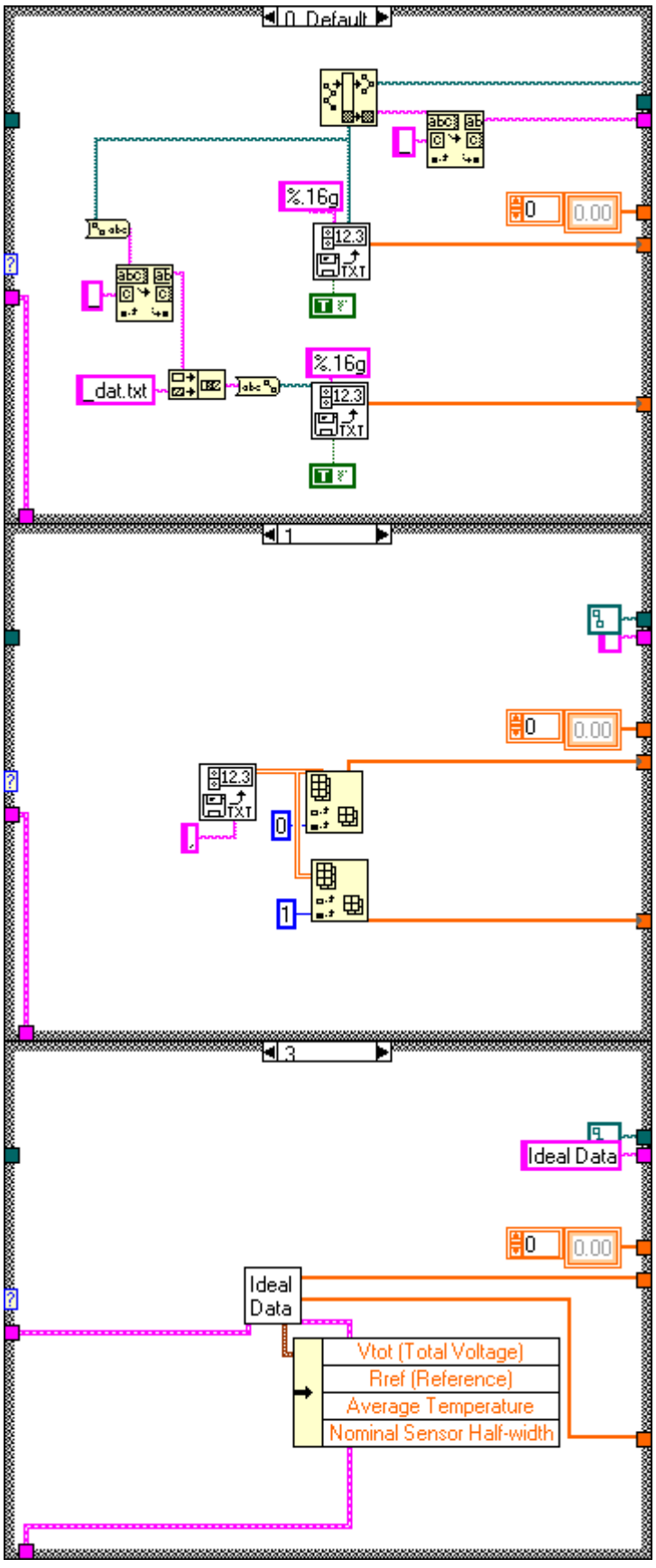
0 Default
%.16g
0
0.00
12.3
TXT
_dat.txt
%.16g
1
0
0.00
0
1
3
Ideal Data
0
0.00
Ideal Data
Vtot (Total Voltage)
Rref (Reference)
Average Temperature
Nominal Sensor Half-width

read and filter data2.vi

Connector Pane

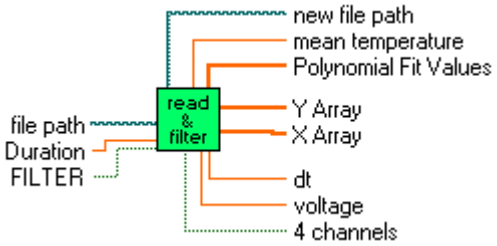

Front Panel

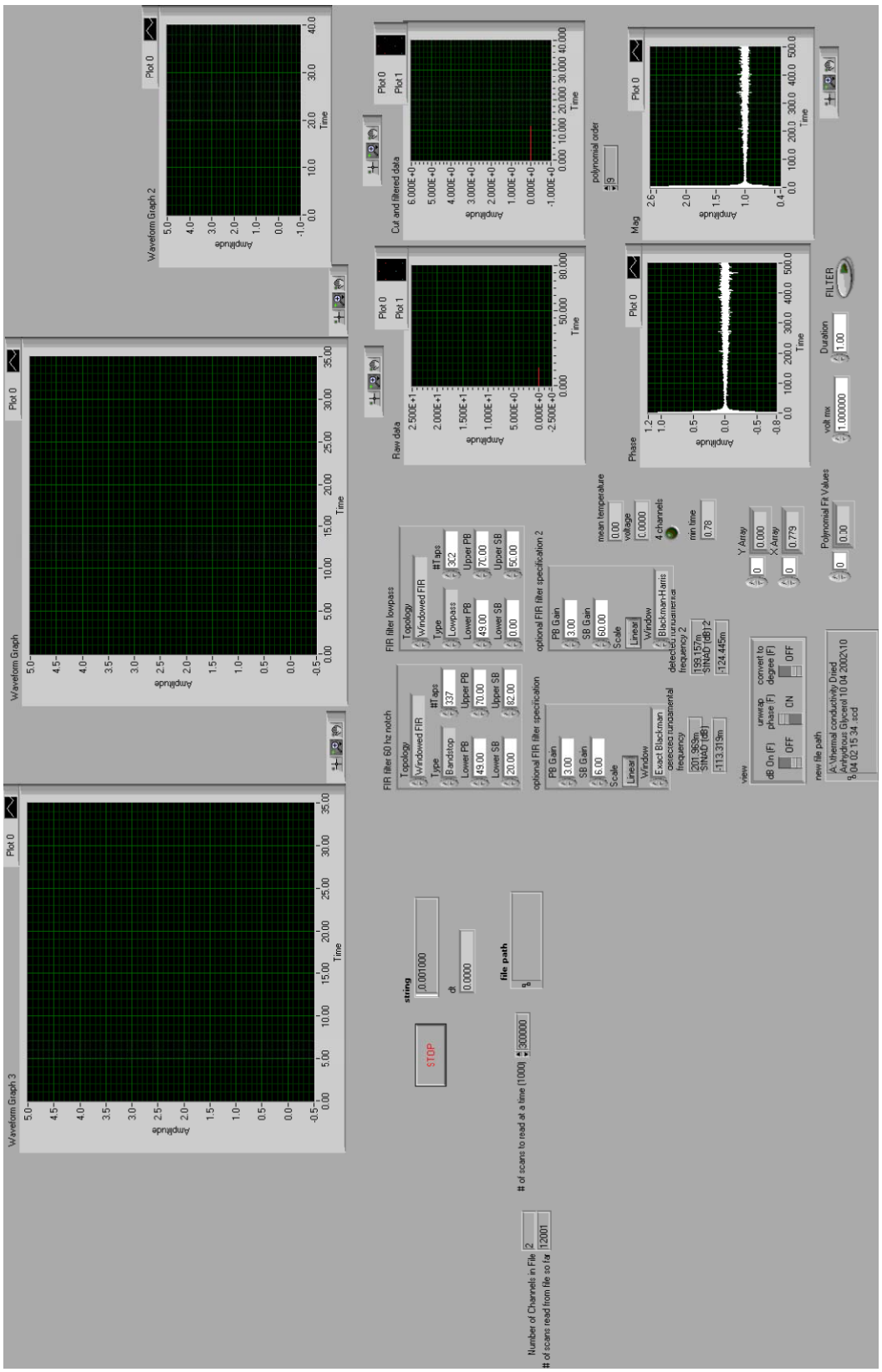
Waveform Graph 2
Plot 0
Waveform Graph
Plot 0
Cut and filtered data
Plot 0
Plot 1
polynomial order
9
Raw data
Plot 0
Plot 1
Mag
Plot 0
Phase
Plot 0
FILTER
Duration
1.00
volt mx
1.000000
FIR filter 60 hz notch
Topology
Windowed FIR
Type
Bandstop
#Taps
337
Lower PB
49.00
Upper PB
70.00
Lower SB
20.00
Upper SB
82.00
Window
Exact Blackman
optional FIR filter specification
PB Gain
3.00
SB Gain
6.00
Scale
Linear
detected fundamental frequency
201.363m
SINAD (dB)
-113.319m
FIR filter lowpass
Topology
Windowed FIR
Type
Lowpass
#Taps
362
Lower PB
49.00
Upper PB
70.00
Lower SB
0.00
Upper SB
50.00
Window
Blackman-Harris
optional FIR filter specification 2
PB Gain
3.00
SB Gain
60.00
Scale
Linear
detected fundamental frequency 2
199.157m
SINAD (dB) 2
-124.445m
mean temperature
0.00
voltage
0.0000
4 channels
min time
0.78
Y Array
0
0.000
X Array
0
0.779
Polynomial Fit Values
0
0.00
view
dB On (F)
OFF
unwrap phase (F)
ON
convert to degree (F)
OFF
new file path
A:\thermal conductivity Died Arrhyotous Glycerol 10 04 2002\10 9_04 02 15 34 .scd
Waveform Graph 3
Plot 0
STOP
string
0.0001000
dt
0.0000
file path
# of scans to read at a time (1000)
300000
Number of Channels in File
2
# of scans read from file so far
12001

Block Diagram

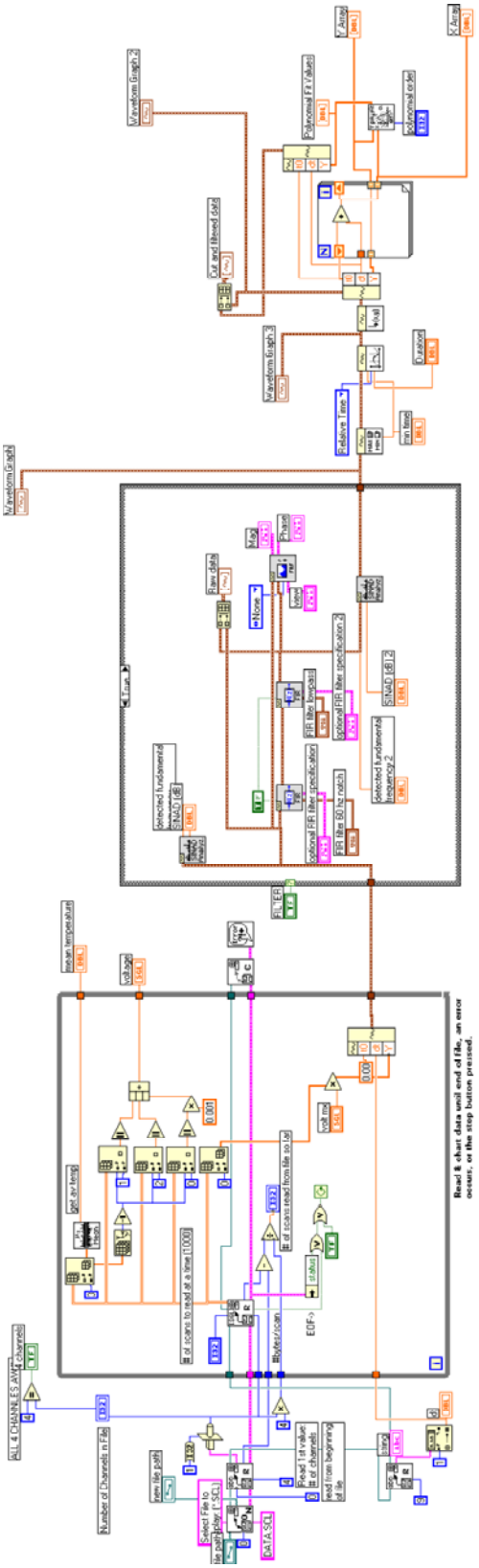

APPENDIX B

EQUATIONS AND CALCULATIONS

B.1 DERIVATION OF EQUATIONS USED IN THE DATA ANALYSIS

B.1.1 R_{sen} Derivation

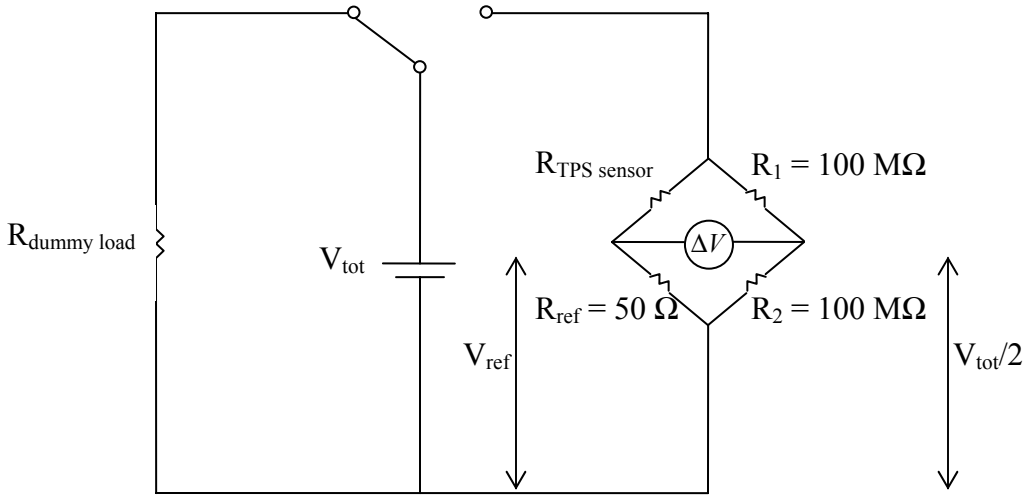

Figure B-1: Wheatstone bridge circuit, containing the TPS sensor.

$$V_{tot} = IR_{sen} + IR_{ref}$$

$$I = \frac{V_{tot}}{R_{sen} + R_{ref}} = \frac{V_{ref}}{R_{ref}}$$

$$V_{ref} = \frac{V_{tot}}{2} - \Delta V$$

$$R_{sen} = \frac{V_{tot} - IR_{ref}}{I} = \frac{V_{tot} - \frac{V_{ref}}{R_{ref}} R_{ref}}{\frac{V_{ref}}{R_{ref}}} = R_{ref}\left[\frac{V_{tot} - V_{ref}}{V_{ref}}\right] = R_{ref}\left[\frac{V_{tot} - \frac{V_{tot}}{2} + \Delta V}{\frac{V_{tot}}{2} - \Delta V}\right]$$

$$R_{sen} = R_{ref}\left[\frac{1}{\frac{1}{2} - \frac{\Delta V}{V_{tot}}} - 1\right] \qquad \textbf{(0-1)}$$

B.1.2 H(τ) Values From Numerical Integration at Different τ-Values

τ	H	τ	H	τ	H
0.00	0.000000	1.10	0.572665	3.20	0.740317
0.05	0.048603	1.20	0.591781	3.30	0.743238
0.10	0.094464	1.30	0.608504	3.40	0.745993
0.15	0.137664	1.40	0.623225	3.50	0.748595
0.20	0.178281	1.50	0.636264	3.60	0.751056
0.25	0.216396	1.60	0.647881	3.70	0.753387
0.30	0.252088	1.70	0.658285	3.80	0.755598
0.35	0.285436	1.80	0.667651	3.90	0.757699
0.40	0.316521	1.90	0.676120	4.00	0.759696
0.45	0.345427	2.00	0.683813	4.10	0.761598
0.50	0.372243	2.10	0.690828	4.20	0.763412
0.55	0.397071	2.20	0.697250	4.30	0.765142
0.60	0.420023	2.30	0.703148	4.40	0.766795
0.65	0.441217	2.40	0.708583	4.50	0.768376
0.70	0.460781	2.50	0.713607	4.60	0.769890
0.75	0.478839	2.60	0.718263	4.70	0.771339
0.80	0.495516	2.70	0.722590	4.80	0.772730
0.85	0.510931	2.80	0.726622	4.90	0.774064
0.90	0.525193	2.90	0.730386	5.00	0.775346
0.95	0.538408	3.00	0.733909		
1.00	0.550668	3.10	0.737213		

B.2 RAMAN SPECTROSCOPY ANALYSIS

The following analysis was performed by Christopher Matranga of US DOE National Energy Technology Laboratory.

The close up of the Methane Region was deconvoluted by a least squares fit of the experimental spectra to 2 lorenztian oscillators:

$$I(\nu) = \sum_{q=1}^{2} \frac{A_q \Gamma_q}{(\nu - \nu_q)^2 + \Gamma_q}$$

A_q = Peak Height, Γ_q is the Half-Width Half Max,
ν_q is the resonance freq of the peak.

From the parameters on the fits the crystallographic hydration number and the occupancy of the large and small cages can be determined using:

1) $\frac{I_L}{3I_s} = \frac{\theta_L}{\theta_s}$,

2) $\Delta\mu_w^o = -\frac{RT}{23}\left[3\ln(1-\vartheta_L) - (1-\vartheta_s)\right]$,

3) $n_c = \frac{23}{(3\vartheta_L + \vartheta_S)}$

$\Delta\mu_w^o$ = 1297 J mol^{-1}, I_L & I_s are the integrated intensities from the deconvolution, θ is the cage occupancy, n_c is the crystallographic hydration number.

(for references on these equations see Sum, Burruss & Sloan, J. Phys Chem-B, 1997, 101, pg 7371-7377).

From curve fits using Excel the frequency & full width half maximums (FWHM) for the peaks associated with the large & small cages are:

Large Cage:
Resonance Energy = 2902.4 cm^{-1}
FWHM = 7.28 cm^{-1}

Small Cage
Resonance Energy = 2914.2 cm^{-1}
FWHM = 4.68 cm^{-1}

REFERENCES

[1] Sloan, E. Dendy, Jr., *Clathrate Hydrates of Natural Gases*, *2d. Edition*, Marcel Decker, New York, 1998.

[2] Makogon, Yuri F., *Hydrates of Hydrocarbons*, PennWell Books, Tulsa, OK, 1997, p. 397.

[3] Millheim, Keith; Kwan, Jonathan; Maurer, Williams; "A Field Oriented Natural Gas Hydrate Research Project for The Alaska North Slope – Resource Evaluation and Possible Testing", *Fuel Chemistry Division Preprints*, 2002 47 (1), 344.

[4] Rosenberg, Nina, Durham, William, Kirby, Stephen, Brewer, Peter, "Final Report for the September 2001 Workshop on Physical and Chemical Property Measurements for the Gas Hydrate R & D Community", October 2001.

[5] Gustafsson, Silas E, "Transient plane source techniques for thermal conductivity and thermal diffusivity measurements of solid materials", *Rev. Sci. Instrum.*, 62 (3), March 1991.

[6] U.S. Patent 5,044,767 9/1991 Gustafsson, Silas.

[7] Tse, J.S., Shpakov, V., Belosludov, V., Murashov, V.I., "Electronic and Vibrational Properties of Gas Hydrates," Proc. 213th ACS National Meeting, Vol. 42 (2), p. 534, San Francisco, CA, April 13-17, 1997.

[8] Trout, Bernhardt, "Solvation Effects in Clathrate-Hydrates and Biological Systems", Chemical and Petroleum Engineering Seminar at the University of Pittsburgh, April 11, 2003.

[9] Link, Dirk D., Ladner, Edward P., Elsen, Heather A., Taylor, Charles E.; "Physical Properties and Conversion of Methane Hydrates", *Fuel Chemistry Division Preprints*, 2002, 47 (1), 341.

[10] Waite, William F., Pinkston, John, Kirby, Stephen H., "Preliminary Laboratory Thermal Conductivity Measurements in Pure Methane Hydrate and Methane Hydrate-Sediment Mixtures: A Progress Report", *Proceedings of the Fourth International Conference on Gas Hydrates*, Yokohama, May 19-23, 2002.

[11] Stoll, R.D., G.M., Bryan "Physical properties of sediments containing gas hydrates", *J. Geophys. Res*., 84, 1629-1634.

[12] Asher, G.B., *Development of a Computerized Thermal conductivity Measurement System Utilizing the Transient Needle Probe Technique: An Application to Hydrates in Porous Media*, Dissertation T-3335, Colorado School of Mines, (1987).

[13] Cook, J.G., Leaist, D.C., "An Exploratory Study of the Thermal Conductivity of Methane Hyddrate", *Geophysical Research Letters*, Vol. 10, No. 5, pgs. 397-399, May 1983.

[14] Ross, R.G. Anderson, P. Bastrom, G., *Nature*, 290, 322, 1981.

[15] deMartin, Brian J., *Laboratory Measurements of the Thermal Conductivity and Thermal Diffusivity of Methane Hydrate at Simulated In Situ Conditions, Master of Science Thesis*, May 2001.

[16] Gustafsson, Silas E., "Thermal Conductivity of Solids Measured with the Transient Hot Strip and the Transient Plane Source Techniques", *Thermal Conductivity*, 22, 1994.

[17] Gustafsson, Silas E., Suleiman, Bashir, "The Transient Plane Source Technique: Experimental Design Criteria", High Temperatures-High Pressures, 1991, vol. 23, pgs. 289-293.

[18] Carslaw, H.S., Jaeger, J.C., *Conduction of Heat in Solids*, Oxford University Press, 1959.

[19] Agrawal, R., Saxena, N.S., Sharma, K. B., Sreekala, M. S., Thomas, S, "Thermal conductivity and thermal diffusivity of reinforced binary phenolformaldehyde composites", Indian Journal of Pure & Applied Physics, vol. 37, Dec. 1999, pp. 865-869.

[20] Log, T., S. E. Gustafsson, "Transient Plane Source (TPS) Technique for Measuring Thermal Transport Properties of Building Materials", *Fire and Materials*, vol. 19, 43-49, 1995.

[21] Gustavsson, J.S.; Gustavsson, M.; Gustafsson, S.E.; "On the Use of the Hot Disk Thermal Constants Analyser for Measuring the Thermal Conductivity of Thin Samples of Electrically Insulating Materials", *Thermal Conductivity 24*, Vol. 24, p. 116, 1999.

[22] Gustafsson, Silas E, Karawacki, E., Chohan, M. A., "Thermal transport studies of electrically conducting materials using the transient hot-strip technique", J.*Phys. D: Appl. Phys.*, Vol. 19, p. 727, 1986.

[23] Gustafsson, Silas E, "Transient hot-strip method for measuring thermal conductivity and specific heat of non-conducting solids and liquids", *Proceedings of the Eighth Symposium on Thermophysical Properties*, Vol. II, Edited by J.V. Sengers, American Society of Mechanical Engineers, New York, 1982.

[24] Warzinski, R.P., Lee, C.-H., Holder, G.D., "Supercritical-fluid solubilization of catalyst precursors: the solubility and phase behavior of molybdenum hexacarbonyl in supercritical

carbon dioxide and application to the direct liquefaction of coal", *Journal of Supercritical Fluids*, 5, 60-71.

[25] Rosenbaum, Eilis, Shaw, David, Lynn, Ronald, Holder, Gerald; Warzinski, Robert; "Thermal Properties and Characterization of Gas Hydrates", AIChE Third Topical Conference on Natural Gas Utilization Conference Proceedings, National Meeting, April 2003.

[26] Models collected and developed by Dr. David Shaw, Geneva College, 3200 College Ave. 15010, and obtained through personal communication.

[27] Godbee, Herschel W., Ziegler, Waldemar T., "Thermal Conductivities of MgO, Al_2O_3, and ZrO_2 Powders to 850 ^{o}C. II.Theoretical", Journal of Applied Physics, vol. 37, 1, Jan. 1966.